# PHOTODISSOCIATION OF OZONE IN THE HARTLEY BAND:

# EVIDENCE FOR A Λ-DOUBLET PREFERENCE

A Dissertation

by

CAROLYN ELISE GUNTHARDT

Submitted to the Office of Graduate and Professional Studies of
Texas A&M University
in partial fulfillment of the requirements for the degree of

DOCTOR OF PHILOSOPHY

| | |
|---|---|
| Chair of Committee, | Simon W. North |
| Committee Members, | Michael B. Hall |
| | Timothy R. Hughbanks |
| | George R. Welch |
| Head of Department, | Simon W. North |

December 2020

Major Subject: Chemistry

## ABSTRACT

Experiments have been performed that provide evidence for a Λ-doublet preference in the $O_2(a^1\Delta_g)$ fragments resulting from the photodissociation of ozone in the Hartley band. In a recent study, the odd/even population alternation in the $O_2(a^1\Delta_g)$ rotational distribution first observed at 300 K was reproduced in a jet-cooled molecular beam. The population alternation, which favors the even rotational states, was found to be temperature dependent. The measured temperature dependence of the alternation, decreasing alternation with increasing temperature, is inconsistent with a parity-selective curve crossing origin as previously proposed. In this work, additional measurements were made to determine the origin of the population alternation. Using improved experimental techniques, the 2+1 resonance enhanced multiphoton ionization (REMPI) spectrum of the nascent $O_2(a^1\Delta_g)$ fragments following the 266 nm photolysis of 60 K ozone was remeasured. A quantitative $O_2(a^1\Delta_g)$ rotational distribution was extracted from the new spectrum using improved analysis techniques. Previous REMPI spectra have been refit using the new analysis. Additionally, ion imaging was used to measure the temperature dependent vector correlations of $O_2(a^1\Delta_g)$ fragments in odd and even rotational states. Consistent with previous results, the **v-j** and **μ-j** correlations were more depolarized for the odd rotational states than for the even rotational states, while the **μ-v** correlation was found to be independent of rotational state parity. A classical model based on a Λ-doublet

preference was developed which qualitatively reproduces the experimental trends in the odd/even population alternation and vector correlations. According to this model the odd/even population alternation is a result of preferential formation of the A′ Λ-doublet of $O_2(a^1\Delta_g)$. Initial excitation in the Hartley band is to the B state which has A′ symmetry. Singlet products result from diabatic dissociation on the B state, so conservation of symmetry dictates preferential formation of the A′ Λ-doublet of $O_2(a^1\Delta_g)$. Due to nuclear exchange symmetry restrictions, the A′ Λ-doublet can only occupy even rotational states while the A″ Λ-doublet can only occupy odd rotational states. Parent out-of-plane rotation facilitates the formation of the A″ Λ-doublet, explaining the relative increase in odd state population with increasing temperature as well as the depolarization of the odd state **v-j** and **μ-j** vector correlations.

DEDICATION

*To my parents*

# ACKNOWLEDGEMENTS

Many thanks are in order, as I could not have completed this work on my own. First, I would like to thank all of the members of the North group. Over the years the North group has become like a second family to me. There are a few members I would like to thank in particular. Wei, you are one of the sweetest, most genuine people I have ever met. Thank you for welcoming me to the group with open arms and teaching me all about vector correlations. Colin, thank you for being an amazing mentor and friend. Thank you for always being patient with me as a stripped screws and broke bubblers. I have learned so much from both of you and will always look back fondly at our time spend in lab together. Zach, it has been a joy sharing an office with you. Thank you for being a great friend and making me laugh. It is hard to be in a bad mood when you are around. Thank you Megan for hanging out with me while I collected data and helping me determine the daily beam temperature. I pass the ozone torch to you; I know you will do great things. Lastly, I would like to thank Michelle. Thank you for laying the groundwork for the work in this dissertation. Your data and insights have been extremely helpful to me.

I would also like to thank my friends who have supported me. Emma, thank you for always being there for me. Your friendship means more to me than I can express. Ben Sr., it has been inspiring to watch you learn and grow. Hanging out with you often provided me with a much-needed reminder that there is more that

is important in the world than chemistry. Agustin, thank you for being an amazing friend. I do not think I would have made it through graduate school without our weekly lunches. Alina, thank you for introducing me to the beautiful world of scientific research and for continuing to be an amazing friend. Your success as a professor continues to inspire and motivate me.

I would like to thank my family for their love and support. Thank you to my parents for letting me find my own path and for always being supportive, no matter where it led me. Thank you for traveling to Texas on the drop of a hat when I needed you. Knowing I have your unconditional love and support means the world to me. Madeline and Graydon, thank you for being amazing siblings.

I would like to thank all of the collaborators I have worked with throughout graduate school. Thank you Shanyu, Professor Guo, and Professor Dawes for realizing my dream of seeing the odd/even alternation reproduced by theory. Thank you Professor McBane for your insightful questions and careful reading of manuscripts. I have learned a lot working with you. Thank you Dr. Hall for taking an interest in the CO Q-branch story and making sure it saw the light of day. Thank you for all of your help with the classical model. Thank you for always providing thoughtful, in depth answers to my questions. I have learned a lot from working with you.

Last but not least, I would like to thank Dr. North. Thank you for accepting me into your group when I decided I wanted to be a physical chemist. Thank you for your mentorship and support throughout the years. Thank you for being patient

with me, and convincing me not to give up when times were rough. Thank you for believing in me enough for the both of us. Thank you for always being there to answer my questions while giving me enough freedom to grow as a scientist. I could not have asked for a better advisor and will be forever grateful.

# CONTRIBUTORS AND FUNDING SOURCES

## Contributors

This work was supervised by a dissertation committee consisting of Professor Simon North, Michael Hall, and Timothy Hughbanks of the Department of Chemistry and Professor George Welch of the Department of Physics.

Some of the spectra analyzed in Chapter 3 were provided by Michelle Warter. The data in Chapter 4 were collected and analyzed in collaboration with Megan Aardema. The analyses depicted in Chapter 5 were conducted in part by Gregory Hall. The quantum scattering calculations presented in Chapter 6 were performed by Shanyu Han, Richard Dawes, Daquin Xie, and Hua Guo. The 226 nm classical trajectory calculations in Chapter 6 were performed by George McBane.

All other work conducted for the dissertation was completed by the student under the advisement of Dr. Simon North of the Department of Chemistry.

## Funding Sources

This work was made possible in part by the Robert A. Welch Foundation under Grant Number A-1405.

TABLE OF CONTENTS

Page

LIST OF FIGURES

Page

LIST OF TABLES

Page

# 1. INTRODUCTION

Ozone is one of the most important trace constituents in the atmosphere and thus is of great interest to atmospheric chemists. Additionally, the multiconfigurational nature of the excited states of ozone provides a stringent test for computational methods to describe excited state dynamics. Consequently, there have been numerous detailed experimental and theoretical studies on the UV photolysis of ozone. Ozone has four main absorption bands in the UV-Visible-IR region: the Wulf, Chappuis, Huggins, and Hartley bands (see Figure 1.1).

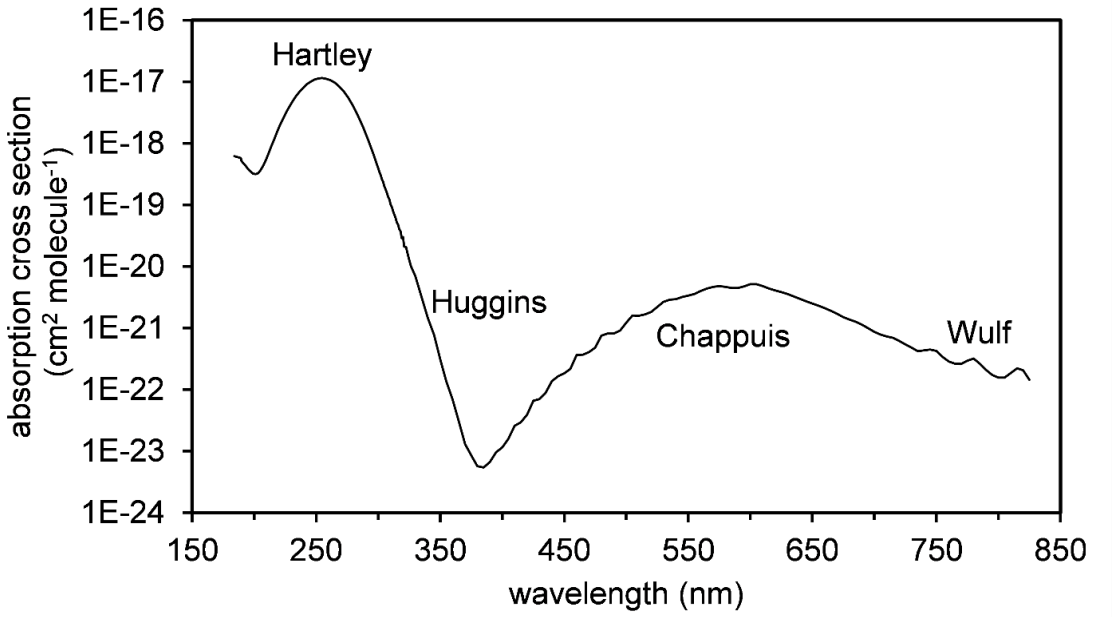


Figure 1.1. Absorption spectrum of ozone. Data from NASA JPL.[1]

The Wulf band (700–1050 nm) is the lowest energy band and results primarily from spin forbidden transitions to the lowest two $^3A''$ states. In the visible region is the Chappuis band (400-700 nm), which results from excitation to the two lowest $^1A''$ states. In the UV region are the Huggins (310-370 nm) and Hartley bands (200-300 nm) which both result from excitation to the third $^1A'$ state, often referred to as the B state (see Figure 1.2).

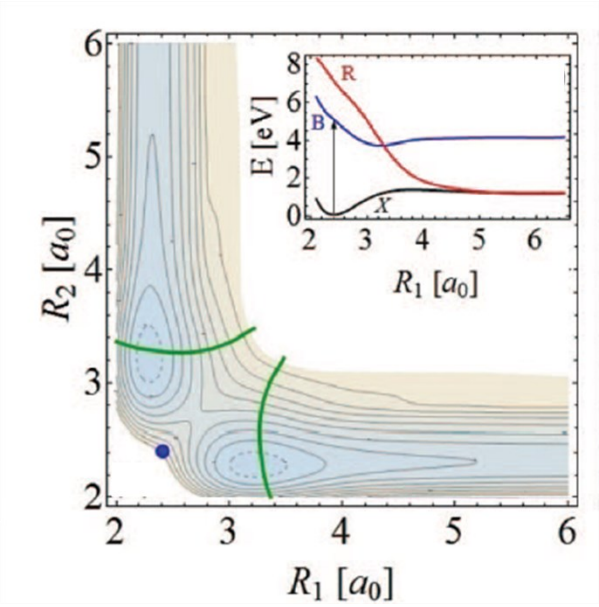


Figure 1.2. 2-D cut through the B state PES with the bond angle fixed at 117°. The dashed contour is 3.6 eV and contour spacings are 0.2 eV. The blue circle represents that Frank Condon point and the green lines represent the crossing seam between the B and R states. The inset shows a 1-D cut through the B, R, and X states with a bond angle of 117° and $R_2$ fixed at 2.42 $a_0$. Figure reprinted from Picconi and Grebenshchikov, *J Chem Phys*, **141**, 074311 (2014)[2] with the permission of AIP Publishing.

The Huggins band results from excitation to the bound levels of the B state, while the Hartley band results from excitation to the continuum of the B state.[3] The Hartley band is the most intense band and is the most important in stratospheric chemistry. The ozone layer absorbs almost all solar radiation below 300 nm, as demonstrated by the solar actinic flux profiles above and below the ozone layer, as shown in Figure 1.3. The quantum yield for ozone photodissociation is almost unity in the Hartley band, and as a result, the photolytic lifetime of atmospheric ozone is only about 16 minutes. The photoproducts often recombine to form ozone, however, so the overall lifetime of ozone in the atmosphere ranges from weeks to months, depending on altitude.[4] Photodissociation of ozone in the Hartley band (200-300 nm) primarily proceeds through two spin allowed channels:

$$O_3 + h\nu \rightarrow O(^3P) + O_2(X\,^3\Sigma_g^-) \quad (1.1)$$

$$\rightarrow O(^1D) + O_2(a^1\Delta_g) \quad (1.2)$$

Both channels start with a parallel transition to the continuum of the B state. The transition dipole moment lies in the molecular plane and is perpendicular to the $C_{2v}$ axis. The B state has a conical seam with a repulsive state of A′ symmetry, referred to as the R state (see inset of Figure 1.2). Molecules that remain on the B state promptly dissociate into singlet products (eq 1.2) and molecules that cross to the R state dissociate into triplet products (eq 1.1).

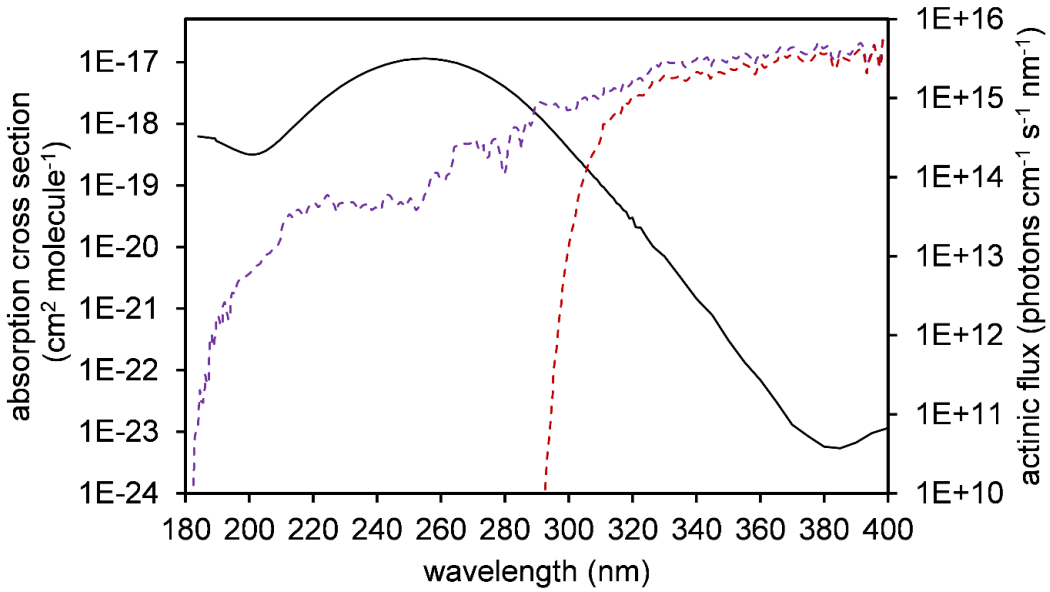


Figure 1.3. Ozone absorption spectrum (solid line) overlaid with the actinic flux (dashed lines) above and below the ozone layer. The actinic flux above the ozone layer is shown in purple and the flux below the ozone layer is shown in red. Data from NASA JPL.[1, 5]

The branching ratio between these two channels is of great importance to atmospheric chemistry as the singlet products are much more reactive than the triplet products. Accordingly, there have been many studies investigating this branching ratio. Figure 1.4 shows the theoretical and experimental branching ratios between the singlet and triplet channels in the Hartley band. It can be seen that throughout most of the Hartley band the singlet/triplet branching ratio is approximately 0.9/0.1. At wavelengths greater than 300 nm the dissociation wavelength approaches the threshold for the singlet channel (310 nm) and the singlet yield decreases. The singlet yield remains nonzero for dissociation energies slightly below the threshold, due to excitation of excited parent molecules

and minor spin forbidden channels. The temperature dependence of the branching ratio has also been investigated. Figure 1.5 shows the temperature dependence of the singlet/triplet branching ratio at a wavelength of 248 nm and includes measurements by Talukdar *et al.*[6] in a bulb as well as a measurement by Sparks *et al.*[7] in a jet-cooled molecular beam. The singlet/triplet branching ratio remains 0.9/0.1 independent of temperature.

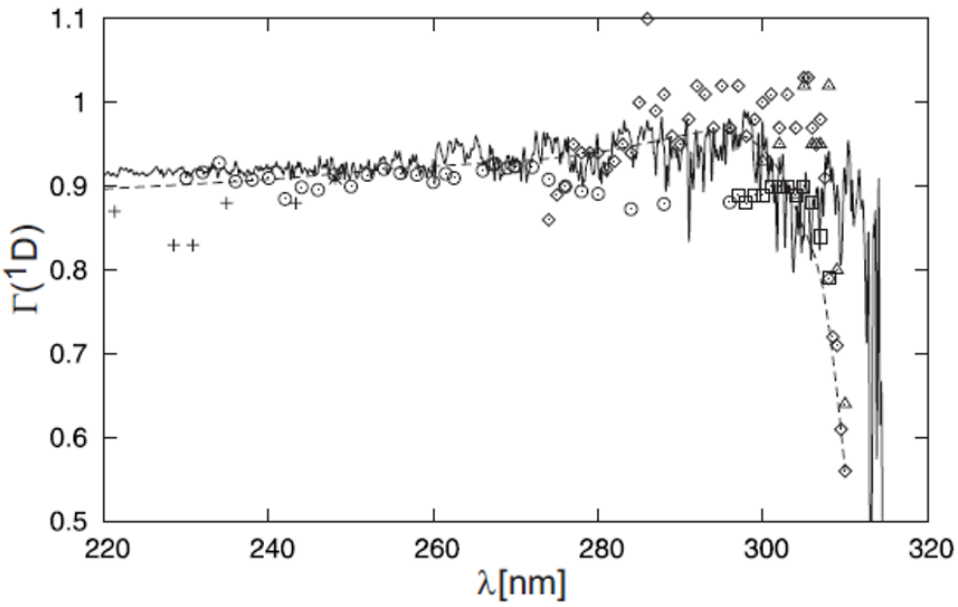


Figure 1.4. Wavelength dependence of calculated (lines) and experimental (symbols) singlet channel branching ratio. The solid line represents quantum mechanical results and the dashed line represents corrected trajectory surface hopping results. Open circles are results from Takahashi *et al.*,[8] open squares are results from Taniguchi *et al.*,[9] + symbols are from Cooper *et al.*,[10] open diamonds are from Trolier and Wiesenfeld,[11] and open triangles are from Ball *et al.*[12] Figure reprinted from Shinke and McBane, *J. Chem. Phys*. **132**, 044305 (2010)[13] with the permission of AIP Publishing.

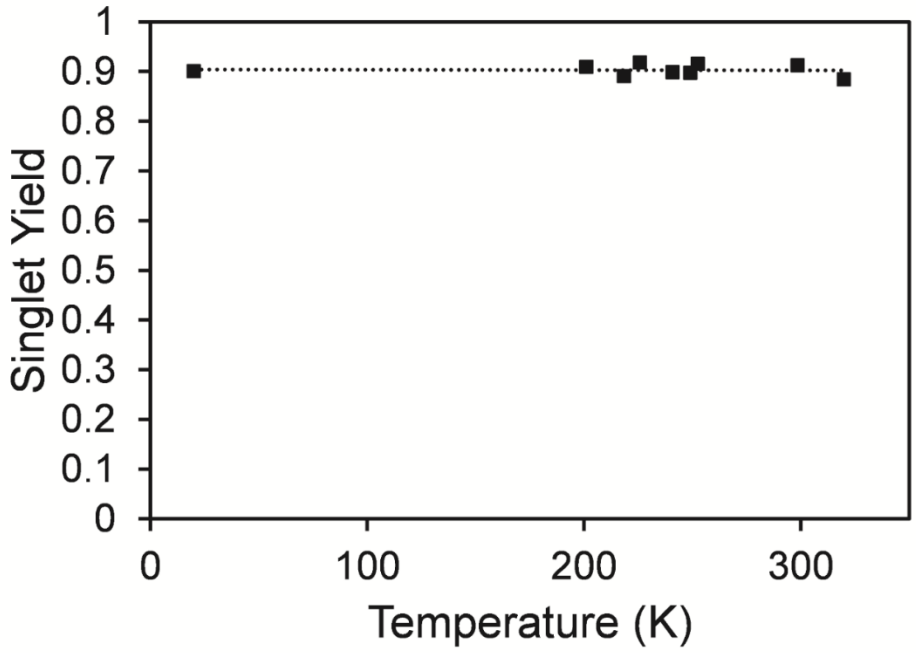


Figure 1.5. Temperature dependence of the singlet yield following photodissociation of ozone at 248 nm. High temperature data points are from Talkudar *et al.*[6] and the low temperature data point is from Sparks *et al.*[7]

In both channels, all energetically allowed vibrational states of the diatomic fragment are populated. In the triplet channel, the $O_2(X\,^3\Sigma_g^-)$ vibrational distribution is highly inverted, with minimum population in v=0.[14] The high degree of vibrational excitation arises because the length of the conserved O-O bond acts as a tuning mode; the longer the length of the conserved bond at the crossing seam the more likely the molecule is to cross from the B to the R state.[2] In the singlet channel, the $O_2(a^1\Delta_g)$ vibrational distribution has a maximum at v=0 with population decreasing monotonically with increasing v.[15] According to calculations by Picconi and Grebenshchikov,[2] in both channels, on average

around 20 percent of the available energy is partitioned into $O_2$ rotation.

Computational studies have been able to reproduce many of the experimental scalar distributions and branching ratios. There is one experimental observable, however, that many computational studies have failed to reproduce: an odd/even population alternation in the $O_2(a^1\Delta_g)$ rotational state distribution. This population alternation was first observed in 300 K Coherent anti-Stokes Raman Scattering (CARS) experiments conducted by Valentini *et al.*[16, 17] (see Figure 1.6). The population alternation favors the even rotational states, and decreases in magnitude with both increasing $O_2(a^1\Delta_g)$ vibrational state and photolysis wavelength.

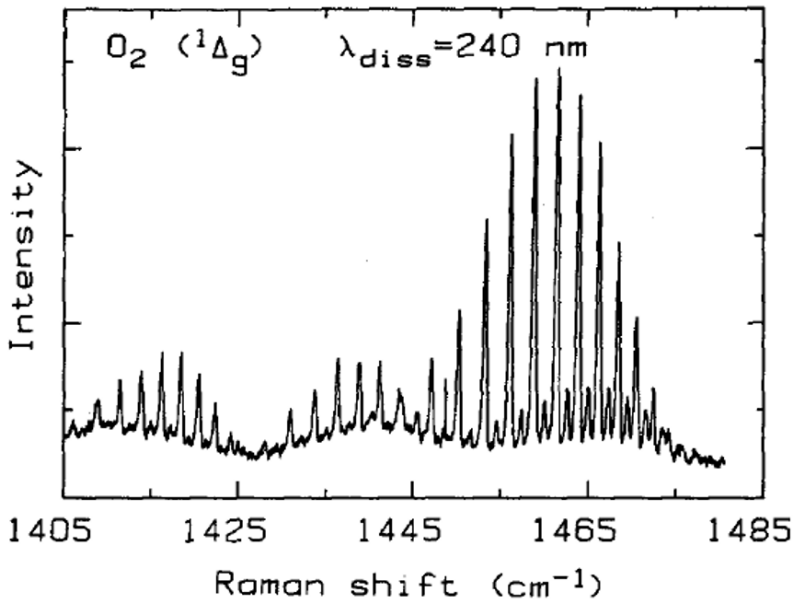


Figure 1.6. CARS spectrum of $O_2(a^1\Delta_g)$ fragments resulting from the photodissociation of 300 K ozone at 240 nm. Figure reprinted from Valentini *et al. J. Chem. Phys.* **86**, 6745 (1987)[17] with the permission of AIP Publishing.

There are two competing theories on the origin of the odd/even population alternation. Valentini *et al.*[17] proposed that the alternation is a result of the curve crossing between the potentials involved in the singlet and triplet channels (eq 1.2 and 1.1) in the Hartley band. Due to nuclear exchange restrictions, $O_2(X\,^3\Sigma_g^-)$ can only occupy odd rotational states. Because of this, Valentini *et al.* proposed that only molecules occupying odd rotational states could cross from the B state to the R state. This essentially depletes the singlet channel of odd rotational states as they cross from the singlet channel to form triplet products. This hypothesis was supported by the fact that the sum of the missing odd states in the triplet channel added up to 6-15 percent, in close agreement with the observed triplet yield of 10 percent.[18, 19]

To confirm this model, Valentini *et al.* conducted mixed isotope experiments.[17] A mixture of ozone isotopologues was synthesized by introducing a 1:1 mixture of $^{16}O^{16}O$ and $^{18}O^{18}O$ into an ozone generator. The mix of isotopologues was photodissociated and the CARS spectra of the $^{16}O^{16}O(a^1\Delta_g)$ and $^{16}O^{18}O(a^1\Delta_g)$ fragments were measured. As observed previously, the $^{16}O^{16}O(a^1\Delta_g)$ rotational distribution exhibited a population alternation. Unlike $^{16}O^{16}O$ the two nuclei in the $^{16}O^{18}O$ isotopologue are not indistinguishable, so $^{16}O^{18}O(X\,^3\Sigma_g^-)$ can occupy both odd and even rotational states. Consequently, according to the model, in the case of mixed isotope fragments both even and odd molecules can cross from the singlet channel to the triplet channel. Consistent with the curve crossing model, no population alternation was observed in the

$^{16}O^{18}O(a^1\Delta_g)$ rotational distribution. To determine if the population alternation was caused by an overproduction of even states or a depletion of odd states, Valentini *et al.* compared the statistically adjusted $^{16}O^{16}O(a^1\Delta_g)$ and $^{16}O^{18}O(a^1\Delta_g)$ population distributions (Figure 1.7). The population of both the odd and even $^{16}O^{18}O(a^1\Delta_g)$ fragments was in agreement with the population of the odd $^{16}O^{16}O(a^1\Delta_g)$ fragments, suggesting that for $^{16}O^{18}O(a^1\Delta_g)$ fragments both the odd and even states were being depleted from the singlet channel at the same rate as the odd $^{16}O^{16}O(a^1\Delta_g)$ fragments. If this is true, it would mean that the triplet yield for mixed isotope $O_2$ is twice the triplet yield for homonuclear $O_2$. The same arguments hold for $^{16}O^{17}O(a^1\Delta_g)$ or any other heteronuclear isotopologue.

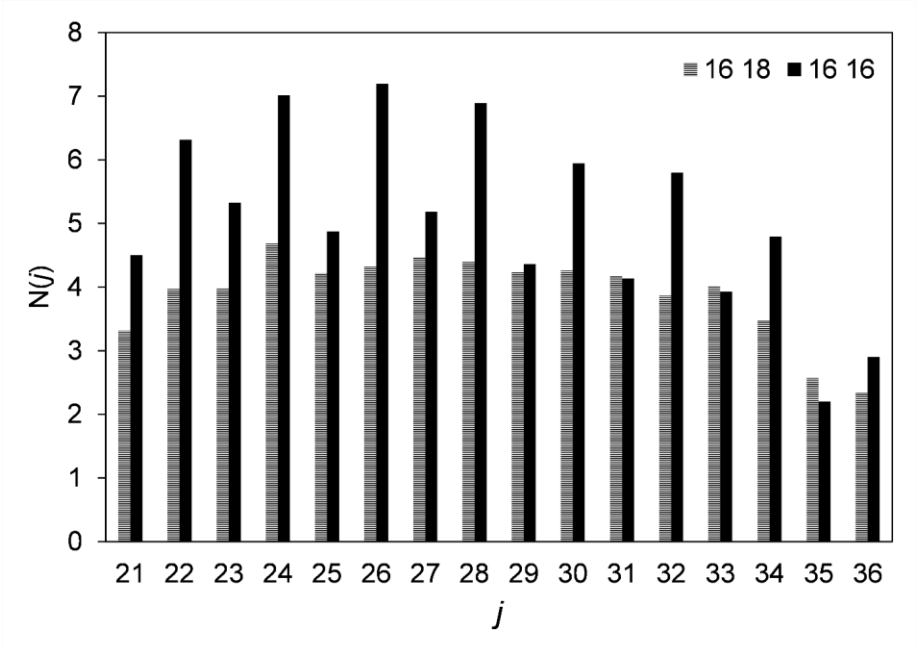


Figure 1.7. Comparison of $^{16}O^{16}O(a^1\Delta_g)$ and $^{16}O^{18}O(a^1\Delta_g)$ populations following photodissociation of a mix of ozone isotopologues. Data from Valentini *et al.*[17]

The second model for the odd/even alternation is based on a preference for the formation of the $O_2(a^1\Delta_g)$ A′ Λ-doublet. In molecules with cylindrical symmetry, states with nonzero angular momentum split into two Λ-doublets. In a nonrotating In linear molecules with cylindrical symmetry, electronic states with nonzero orbital angular momentum (Π, Δ, Φ…) are split into two states referred to as Λ-doublets.[20] These Λ-doublets are degenerate for a non-rotating molecule, but in a rotating molecule the Λ-doublets split in energy. This energy splitting increases with the total angular momentum quantum number *j*. In most cases the energy splitting between the two Λ-doublets is extremely small (less than a wavenumber), with splitting in Δ-states being even smaller than splitting in Π-states. In the high-*j* limit the two Λ-doublets are described by the symmetry of their electronic wavefunctions with respect to the rotational plane of the molecule. One Λ-doublet has a wavefunction which is symmetric with respect to the rotational plane, the A′ Λ-doublet, and the other has a wavefunction which is antisymmetric with respect to the rotational plane, the A″ Λ-doublet. In the case of $^{16}O^{16}O(a^1\Delta_g)$, due to nuclear exchange restrictions, the A′ doublet can only occupy even rotational states and the A″ doublet can only occupy odd rotational states. In heteronuclear $^{16}O^{18}O(a^1\Delta_g)$, the nuclear symmetry is broken and both Λ-doublets can occupy even and odd rotational states.

A Λ-doublet preference can be understood based on the conservation of symmetry. Baloïtcha and Balint-Kurti alluded to a Λ-doublet propensity mechanism by stating that careful consideration must be given to the initial and

dissociative wavefunctions, and that in the absence of additional angular momentum only even fragments would be formed.[21] The excited B state of ozone has A′ symmetry and thus is symmetric with respect to molecular plane. In the absence of initial $O_3$ rotation, the final $O_2$ rotational plane is identical to the $O_3$ molecular plane at the time of dissociation leading to the exclusive formation of the A′ Λ-doublet (even rotational states). Out-of-plane parent rotation will tilt the fragment rotational plane so it no longer lies in the original parent molecular plane. When the rotational plane is tilted with respect to the molecular plane at the time of dissociation conservation of symmetry is achieved by a linear combination of the two Λ-doublets, allowing for the formation of the A″ Λ-doublet (odd rotational states). While there will still be a preference for the A′ Λ-doublet in the case of $^{16}O^{18}O(a^1\Delta_g)$, this preference will not lead to an odd/even population alternation because in this case the A′ Λ-doublet can occupy both even and odd rotational states.

Valentini *et al.* acknowledged that preferential formation of the A′ Λ-doublet would lead to an odd/even population alternation in the rotational distribution.[17] The authors ruled out this possibility however, because the mixed isotope study suggested that the alternation was produced due to a depletion of odd states, not an increased production of even states. This evidence, however, is based on the comparison of absolute populations of two separate rotational distributions, which is a very difficult measurement to make. The direct comparison of $^{16}O^{16}O$ and $^{16}O^{18}O$ populations relies on many assumptions. Some of these assumptions

include that the distribution of isotopologues in the initial mixture was statistical, all of the isotopologues have identical absorption cross sections, and both bonds are equally likely to break for the asymmetric isotopologues ($^{16}O^{16}O^{18}O$ and $^{18}O^{18}O^{16}O$). At low pressures, it has been found that the mixture of ozone isotopologues formed is not statistical, with asymmetric isotopologues favored over symmetric isotopologues ($^{16}O^{16}O^{18}O$ vs $^{16}O^{18}O^{16}O$).[22] Additionally, a theoretical study found that the photodissociation of the $^{16}O^{16}O^{18}O$ isotopologue led to a slight preference for forming the $^{16}O^{18}O$ fragment over the $^{16}O^{16}O$ fragment.[23]

There are, however, many inconsistencies with the curve crossing model of Valentini *et al.* Calculations have shown that rotational state of the $O_2$ fragment is not determined before the curve crossing[2] and that, at the crossing point, exchanging the two nuclei is an unfeasible symmetry operation.[2, 24] This is because the crossing seam is near the minima of the B state, as shown in Figure 1.2. Near the conical intersection the even and odd states are nearly degenerate and are highly localized around Jacobi coordinate angles 60° and 120°. The two minima are separated by a 1.2 eV barrier, which is much greater in energy than the bending energy of approximately 0.2 eV. Additionally, the trends Valentini *et al.* observed in the degree of odd/even alternation with wavelength and fragment vibrational state are inconsistent with the curve crossing model.[2] The probability of a diabatic curve crossing can be approximated using the 1-D Landau-Zener equation

$$P_{cross} = 1 - e^{\left(\frac{-2\pi V_{12}^2}{\hbar v|\Delta F|}\right)} \quad (1.3)$$

where $V_{12}$ is the coupling between the B and R states, v is the radial velocity, and ΔF is the difference in slopes of the two potentials at the crossing point. In the experiments of Valentini *et al.* it was observed that the odd/even alternation decreased with both increasing photolysis wavelength and $O_2$ vibrational state. According to the 1-D Landau-Zener equation, however, fragments with lower translational energy have a greater chance of diabatically curve crossing. Since fragment translational energy decreases with both increasing photolysis wavelength and $O_2$ vibrational state, according to the curve crossing model it is predicted that the degree of odd/even alternation should increase in both of these cases. Figure 1.8 shows the 1-D Landau-Zener curve crossing probability assuming 0.1 crossing probability for 1236 m/s which is the velocity of the most probable rotational state (v=0, *j*=36) resulting from the 248 nm photodissociation of 300 K ozone.[25] According to the model, following 248 nm dissociation a v=1, *j*=32 fragment (v=1172 m/s) has a 0.11 crossing probability, and following 293 nm dissociation a v=0, *j*=10 fragment (v=400 m/s) has a 0.28 crossing probability. If the alternation was caused by curve crossing, the degree of alternation in the 248 nm v=0 and v=1 distributions should be approximately the same, and the degree of alternation in the 293 v=0 distribution should be approximately three times that observed for the 248 nm, v=0 distribution. Experimentally, the degree of alternation decreases going from 248 nm v=0 to 248 nm v=1, and 248 nm v=0 to 293 v=0.

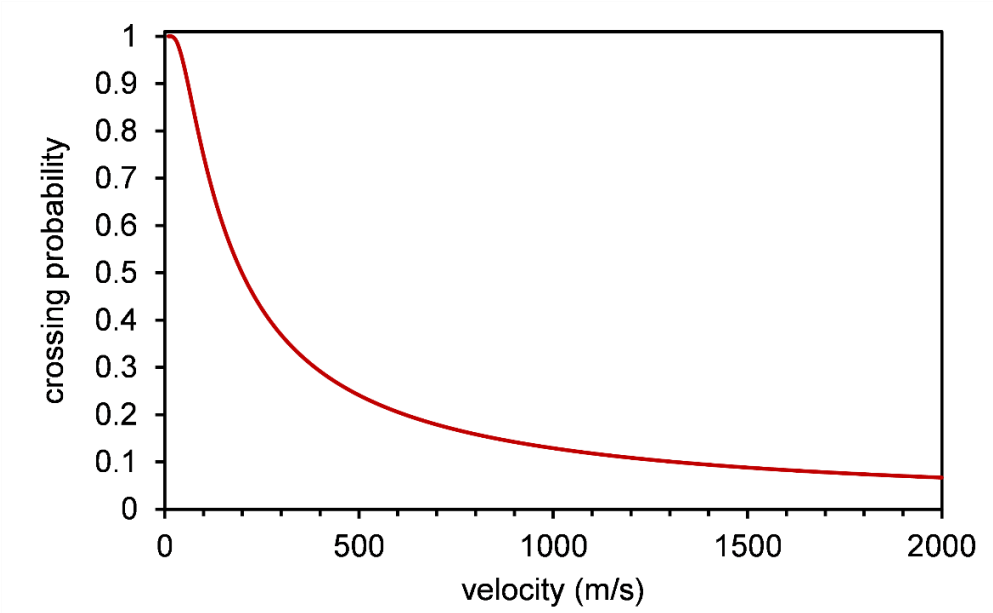


Figure 1.8. B/R crossing probability calculated using the 1-D Landau-Zener equation (eq 1.3). The probability of a *j*=28 fragment following 248 nm photodissociation of ozone was set to 0.1.

Recent studies have provided evidence in favor of the Λ-doublet preference model. A study by Warter *et al.* has reproduced the odd/even population alternation in a molecular beam.[26] Jet-cooled ozone was photodissociated at multiple wavelengths in the Hartley band and the $O_2(a^1\Delta_g)$ photofragments were probed using 2+1 resonance enhanced multiphoton ionization (REMPI). The alternation observed in these molecular beam experiments was much stronger than that observed in the 300 K experiments of Valentini *et al.*[17] By changing the molecular beam temperature, it was found that the magnitude of odd/even alternation is strongly temperature dependent, with decreasing alternation with increasing temperature. The observed temperature

dependence of the odd/even alternation is consistent with a Λ-doublet preference model. As the parent ozone temperature increases, so does the amount of parent rotation, which leads to an increase in the production of the A″ Λ-doublet (odd rotational states) and a decrease in the observed alternation. Additionally, Ritchie and coworkers have observed an odd/even alternation in the **v-j** and **μ-j** vector correlations in a manner that is consistent with the Λ-doublet propensity theory.[27-30] Ritchie and coworkers found that for multiple photolysis wavelengths in the Hartley band, the odd $O_2(a^1\Delta_g)$ fragments had **v-j** and **μ-j** correlations that were more depolarized than those of the even $O_2(a^1\Delta_g)$ fragments. The authors have suggested that one possible explanation for the alternation is that odd rotational states are being formed from a more rotationally excited parent population than the even rotational states. As parent rotation is needed to form the A″ Λ-doublet (odd states), this is exactly what is predicted by the Λ-doublet preference model.

The correct identification of the model responsible for this phenomenon has implications for isotopic fractionation in the stratosphere. In 1981, Mauersberger measured the $^{50}O_3$ concentration in the stratosphere using a mass spectrometer and found that stratospheric ozone was significantly enriched in $^{18}O$.[31] In a subsequent study, Mauersberger also analyzed $^{49}O_3$ and found that stratospheric ozone was approximately equally enriched in both $^{17}O$ and $^{18}O$.[32] While these initial studies reported enrichments between 13 and 40 percent depending on altitude, more recent studies have reported lower enrichment percentages. For example, Fernando *et al.*[33] report enrichments ranging from 5 to 30 percent.

Because the observed isotopic enrichment is mass independent (shows no difference between $^{17}O$ and $^{18}O$), it cannot be caused by typical kinetic isotope effects. If kinetic isotope effects were the cause of the enrichment, the enrichment would be proportional to $\Delta m/m$ so the ratio of $^{17}O/^{18}O$ would be expected to be 0.5.[34] In fact, a kinetic isotope analysis predicts that ozone would be slightly depleted of heavy oxygen isotopes, and not enriched.[35] In addition to the observed atmospheric enrichment, mass independent isotope fractionation has been observed in ozone in a laboratory setting. For example, Thiemens and Heidenreich III observed mass independent isotopic enrichment in ozone formed from electrical discharge in $O_2$.[36] Additionally Morton *et al.* observed enrichment of ozone formed through the recombination of $O(^3P)$ and $O_2(X\,^3\Sigma_g^-)$.[37]

The parity selective curve crossing model provides a possible mechanism for isotopic fractionation resulting from ozone photodissociation while the Λ-doublet preference model does not. Once consequence of the parity selective curve crossing model is that the triplet yield for heteronuclear $O_2$ is twice that of homonuclear $O_2$. Additionally, Valentini argued that because nonadiabatic collisional relaxation of $O_2(a^1\Delta_g)$ to $O_2(X\,^3\Sigma_g^-)$ involves the same curve crossing as the photodissociation, nonadiabatic collisional relaxation of heteronuclear $O_2(a^1\Delta_g)$ is twice as likely as nonadiabatic collisional relaxation of homonuclear $O_2(a^1\Delta_g)$.[38] Both of these effects would serve to enrich $O_2(X\,^3\Sigma_g^-)$ in $^{17}O$ and $^{18}O$ and deplete $O_2(a^1\Delta_g)$ of these heavy isotopes. This enrichment is a consequence of the two ozone nuclei being distinguishable and not the mass of the specific

isotope, so any resulting isotopic fractionation would be mass independent. As $O_2(X\,^3\Sigma_g^-)$ can combine with an O atom to form ozone while $O_2(a^1\Delta_g)$ cannot as $O_2(a^1\Delta_g)$ + O($^3$P) or O($^1$D) correlate to repulsive states in ozone, if recombination rates are faster than isotope exchange, isotopic enrichment in $O_2(X\,^3\Sigma_g^-)$ would lead to isotopic enrichment in ozone. Under atmospheric conditions, however, quenching of $O_2(a^1\Delta_g)$ is extremely fast compared to both the production of $O_2(a^1\Delta_g)$ through photodissociation and recombination of $O_2(X\,^3\Sigma_g^-)$ and O, so the isotopic fractionation in the $O_2(X\,^3\Sigma_g^-)$ reservoir is expected to be on the order of $10^{-4}$ percent, much smaller than the observed isotopic enrichment of ozone in the stratosphere. To account for this, Valentini suggests the presence of a reaction that selectively converts $O_2(a^1\Delta_g)$ to a stable molecule that very slowly releases the heavy isotope depleted oxygen back into the atmosphere, such as $CO_2$. Another possible mechanism involves direct ozone formation from enriched $O_2(X\,^3\Sigma_g^-, v\geq 26)$ molecules formed during the photodissociation:

$$O_2(X\,^3\Sigma_g^-) + O_2(X\,^3\Sigma_g^-, v\geq 26) \rightarrow O_3 + O \qquad (1.3)$$

This reaction was first proposed as a solution to the ozone deficit problem, which was a disagreement between model and measured atmospheric ozone concentrations. If the parity-selective curve crossing model is correct, reaction 1.3 could account for 3% of the isotopic enrichment in the stratosphere.[39]

Theoretically atmospheric chemists should be able to accurately model ozone concentrations in the upper stratosphere and mesosphere where ozone is

in a photochemical steady state and is involved in relatively few chemical reactions.[40] In the 1980s, however, many of the stratospheric and mesospheric models underestimated the concentration of odd oxygen (O and $O_3$) leading to what is referred to as the "ozone deficit problem." One of the proposed solutions to the ozone deficit problem is directly related to ozone photodissociation dynamics. As the recombination reaction

$$O_2(X\,^3\Sigma_g^-) + O(^3P) \rightarrow O_3 \qquad (1.4)$$

is the major ozone formation reaction in the atmosphere, it was proposed that the models may be missing a mechanism of odd oxygen production. A potential source of O atoms is highly vibrationally excited $O_2(X\,^3\Sigma_g^-)$ molecules formed in the photodissociation of ozone. Fairchild *et al.* measured $O_2(X\,^3\Sigma_g^-)$ in vibrational states as high as v=10 following the 274 nm photodissociation of ozone.[41] Slanger *et al.*[42] observed autocatalytic ozone formation when irradiating a cell of $O_2$ with 248 nm light. As the dissociation limit of ground state $O_2$ is 242.4 nm irradiation of 248 nm light should not cause the production of O atoms. The authors proposed that a small amount of ozone was formed in the cell following an unidentified initiation step. That ozone is then photodissociated resulting in some highly vibrationally excited $O_2(X\,^3\Sigma_g^-)$ molecules which have enough internal energy to be dissociated by 248 nm light. In this case, one ozone molecule can form three O atoms, each of which can go on to react with $O_2$ resulting in a net gain of two ozone molecules. If highly vibrationally excited $O_2(X\,^3\Sigma_g^-)$ molecules can be dissociated with light >242 nm under atmospheric conditions, it would

result in a source of O atoms not accounted for by the contemporary models. A study by Toumi *et al.*[43] found that the inclusion of the photodissociation of highly vibrationally excited $O_2$ in atmospheric models can account for the ozone deficit, but the effect is strongly dependent on collisional relaxation rate constants of the highly vibrationally excited $O_2$.

Wodtke and coworkers employed stimulated emission pumping to measure the relaxation rates of highly vibrationally excited $O_2$.[44-46] In this work, stimulated emission pumping was used to produce highly vibrationally excited $O_2(X\,^3\Sigma_g^-$, 19≤v≤27) molecules and laser induced fluorescence (LIF) was used to monitor the change in the prepared state over time in order to determine collisional relaxation rate constants. The experimental collisional relaxation rate measured were an order of magnitude larger than those used in the model of Toumi *et al.*,[43] suggesting that photodissociation of highly vibrationally excited $O_2$ is too slow to compete with collisional deexcitation under atmospheric conditions, and thus does not contribute to ozone formation in the atmosphere. The authors instead proposed a separate ozone formation mechanism involving highly vibrationally excited $O_2$. The collision of $O_2(X\,^3\Sigma_g^-$, v=26) with $O_2(X\,^3\Sigma_g^-$, v=0) has enough energy to overcome the threshold of the bimolecular abstraction reaction in equation 1.4. The authors found that the relaxation rate sharply increased for $O_2(X\,^3\Sigma_g^-$, v≥26) and posited that the increased disappearance rate was a consequence of reaction 1.4. As the O atoms produced in reactions 1.1 and 1.4 can each recombine with $O_2$ to form ozone, photodissociation of ozone followed

by bimolecular abstraction reaction 1.4 would result in a net gain of two ozone molecules. The authors performed "trickle down" spectroscopy, where they prepared molecules in $O_2(X\,^3\Sigma_g^-$, v=27 or 28) and probed $O_2(X\,^3\Sigma_g^-$, v=26) and found that at 295 K only one percent of molecules prepared in v=27 were seen to trickle down into v=26, and no population was observed in v=26 following excitation to v=28, indicating the presence of a dark channel. The dark channel was attributed to the bimolecular abstraction reaction. Miller *et al.*[47] studied the product distribution of $O_2(X\,^3\Sigma_g^-)$ fragments following the photodissociation of ozone at 226 nm using ion imaging and LIF. The imaging and LIF studies confirmed the formation of $O_2(X\,^3\Sigma_g^-)$ in vibrational states up to v=27, showing that the highly vibrationally excited $O_2(X\,^3\Sigma_g^-)$ molecules needed to surpass the threshold of the bimolecular abstraction reaction can indeed be formed from the photodissociation of ozone. Subsequent studies have shown that the highly vibrationally excited $O_2(X\,^3\Sigma_g^-)$ is most likely not participating in a bimolecular abstraction reaction, but is instead undergoing rapid multiquantum deexcitation.[48] Additionally, comparison of updated models and atmospheric measurements are in good agreement suggesting that there is no ozone deficit problem.[49]

In this work, experiments were performed to determine if the odd/even population alternation is due to a preference for forming the A′ Λ-doublet of $O_2(a^1\Delta_g)$ in the UV photodissociation of ozone. If parity-selective curve crossing is not occurring in the photodissociation, it cannot be a source of isotopic fractionation. Many molecular beam scientists consider an experiment where the

parent molecules are at 0 K to be ideal, because in this case parent molecules will be predominantly in their lowest vibrational and rotational states. Some important dynamical processes, however, are dependent on molecules having vibrational or rotational excitation. Because the degree of Λ-doublet preference is dependent on the degree of parent out-of-plane rotation, it is advantageous to study parent molecules with different degrees of rotational excitation. One way of doing this would be with an optical-optical double resonance study, where specific rotational states of the parent ozone molecules could be prepared and dissociated. The same effect can be probed, however, by changing the temperature of the molecular beam. Compared to the photon energy, the initial thermal energy of the parent molecules is small but can still alter the parent rotational distribution even if vibrational excitation is not significant. The ozone Boltzmann rotational state distribution at 60 K and 300 K are shown in Figures 1.9 and 1.10. It can be seen that many more parent rotational states are accessible to the parent at 300 K than 60 K, leading to a higher degree of rotational excitation in a 300 K bulb than in a jet-cooled molecular beam. At 60 K, the full width at half maximum (FWHM) of the K distribution is 2.4 and the FWHM of the J distribution is 4.4. At 300 K the FWHM of the K distribution is 5.4 and the FWHM of the J distribution is 9.9. According to the parity-selective curve crossing model, the degree of odd/even alternation should not change with beam temperature, as in this model the missing odd states are a measure of the triplet yield which is independent of temperature. In this model, any change in the alternation with

temperature would suggest that the coupling between the B and R states was temperature dependent. The Λ-doublet preference model, however, predicts that the odd/even alternation should decrease with increasing temperature because parent rotation increases the probability of forming fragments in odd rotational states. Initial studies by Warter *et al.*[26] have shown a clear decrease in the alternation when increasing the molecular beam temperature from 60 to 200 K, supporting the Λ-doublet preference model. The following Chapters will detail temperature dependent studies of both the odd/even population alternation and vector correlations of the $O_2(a^1\Delta_g)$ products resulting from the UV photodissociation of ozone that further support the Λ-doublet preference model. Chapter 2 describes the experimental apparatus and set up, Chapter 3 focuses on experimental measurements of the rotational distribution using 2+1 REMPI, Chapter 4 will discuss vector correlations derived from ion imaging experiments, and Chapter 5 describes a simple classical model based on a Λ-doublet preference that is able to reproduce the experimental trends discussed in Chapters 3 and 4.

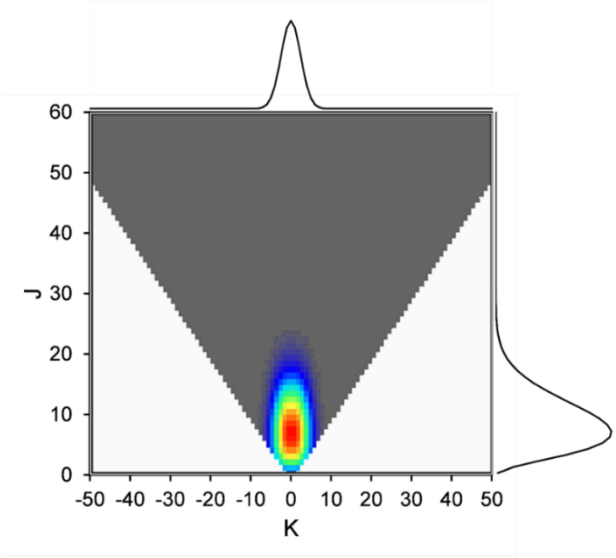


Figure 1.9. 60 K Boltzmann rotational distribution for ozone using a symmetric top approximation.

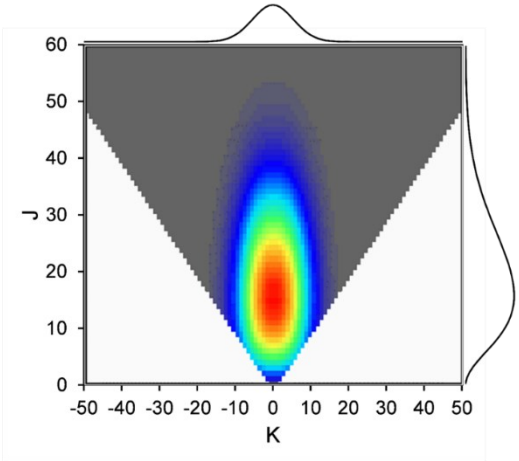


Figure 1.10. 300 K Boltzmann rotational distribution for ozone using a symmetric top approximation.

# 2. EXPERIMENTAL

## 2.1. Velocity Mapped Ion Imaging

Velocity map ion imaging (VELMI) is a powerful technique in the study of gas phase dynamics.[50, 51] The VELMI experiment requires a collision-free environment, and a specialized high vacuum apparatus. The VELMI apparatus consists of three chambers, referred to as the source, main, and detector chambers, as shown in Figure 2.1.

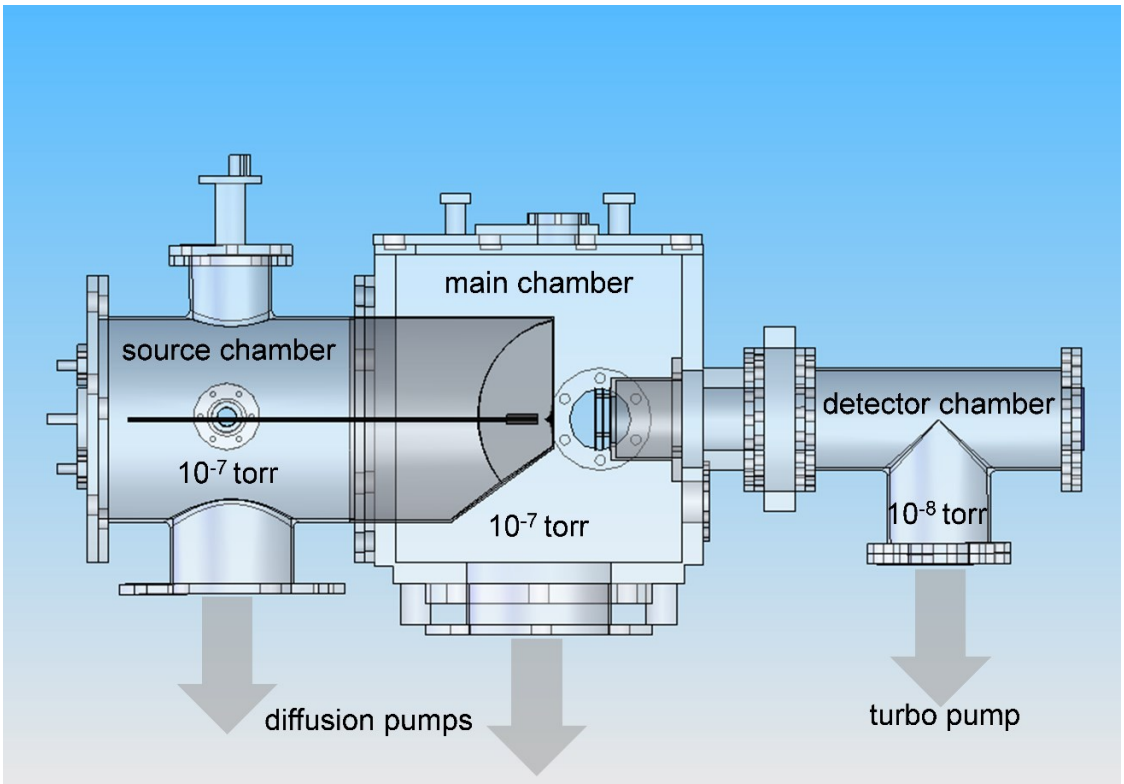


Figure 2.1. VELMI apparatus.

During experiments, both the source and main chambers are evacuated using 6″ Varian VHS-6 diffusion pumps, each backed by a Welch 1397 belt-driven mechanical pump, and reach pressures on the order of $10^{-7}$ torr. The detector region is continuously maintained under vacuum and is evacuated using a turbomolecular pump, reaching pressures on the order of $10^{-8}$ torr. The analyte is introduced in the source chamber and passes through an aperture to the main chamber where it is photodissociated. The resulting photofragments are ionized in the main chamber and accelerated towards the detector which consists of a pair of microchannel plates (MCPs) coupled to a phosphor screen. Figure 2.2 shows a schematic of the apparatus interior.

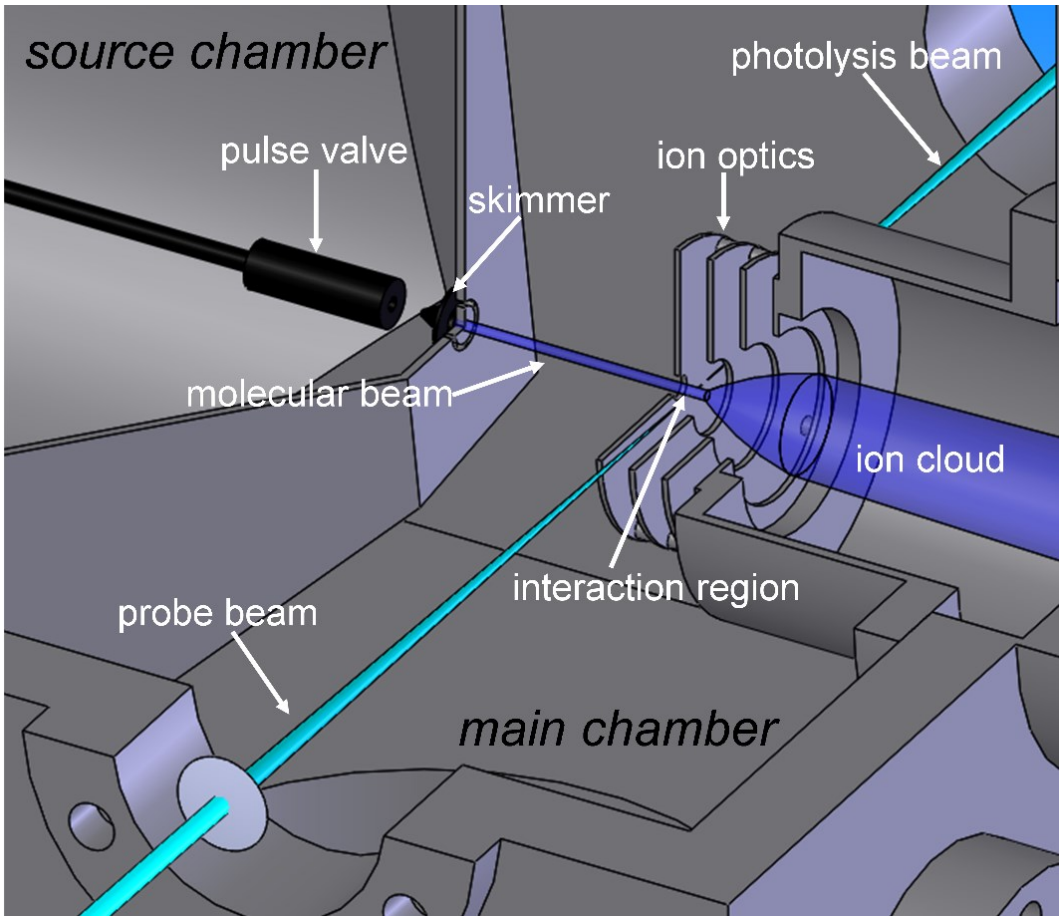

Figure 2.2. Interior of the VELMI apparatus.

### *2.1.1. Molecular Beam*

Ozone was generated from dry oxygen using a commercial ozone generator (CD Laboratory LG-7), which produces an electrical discharge. The resulting ozone was trapped on silica beads in a bubbler maintained at -78.5 °C. Prior to use, the bubbler and silica beads were baked in a vacuum oven overnight to remove any residual water. Ozone is highly reactive towards water and will not trap well on wet silica. After trapping, the headspace of the bubbler was

evacuated. During experiments, the bubbler was maintained between -20 and -40 °C. The resulting ozone vapor pressure depends both the bath temperature and how much ozone is adsorbed to the silica. Typical vapor pressures are estimated to have ranged from 50 to 150 torr.

The ozone was entrained in a flow of helium with a backing pressure of approximately 800 torr and introduced into the source chamber using a General Valve Series 9 pulse valve with a 0.5 or 1.0 mm nozzle diameter. A typical opening time for the pulse valve was 500 μs. The molecular beam undergoes jet-cooled expansion, resulting in ozone rotational temperatures ranging from 60 to 210 K (see Chapter 4). Molecules must pass through a molecular skimmer, a 1.0 or 2.0 mm atomically sharp conical opening, to progress from the source chamber to the main chamber. This collimates the molecular beam by excluding molecules with significant velocity in the x and y directions, where the z axis is along the direction of the molecular beam. While it is difficult to calculate the maximum xy velocity a molecule can have and still make it through the skimmer, it is estimated that molecules with xy velocities above 100 m/s are excluded. As demonstrated in Chapter 4, the observed product speed distributions cannot be explained without accounting for the exclusion of parent molecules with high thermal velocities.

The temperature of the molecular beam can be calibrated using NO. The rotational temperature of NO in a molecular beam with the same seed ratio and backing pressure used in experimental measurements was determined using 1+1

REMPI via the NO($A^2\Sigma^+$)←NO($X^2\Pi$) transition around 226 nm. The $P_1$ branch was probed because it contains isolated, low-*j* peaks. The NO rotational temperature was determined through forward convolution fitting in LIFBASE.[52] The spectrum for the coldest part of the molecular beam and the corresponding simulations are shown in Figure 2.3. The simulations correspond to a temperature of 60 ± 10 K. The temperature of the molecular beam can be estimated using the $O_2$($d^1\Pi$, v=2) ← ← $O_2$($a^1\Delta_g$, v=0) transition to probe the $O_2$($a^1\Delta_g$, v=0) photofragments resulting from the photodissociation of ozone. This method will be discussed in Chapter 4.

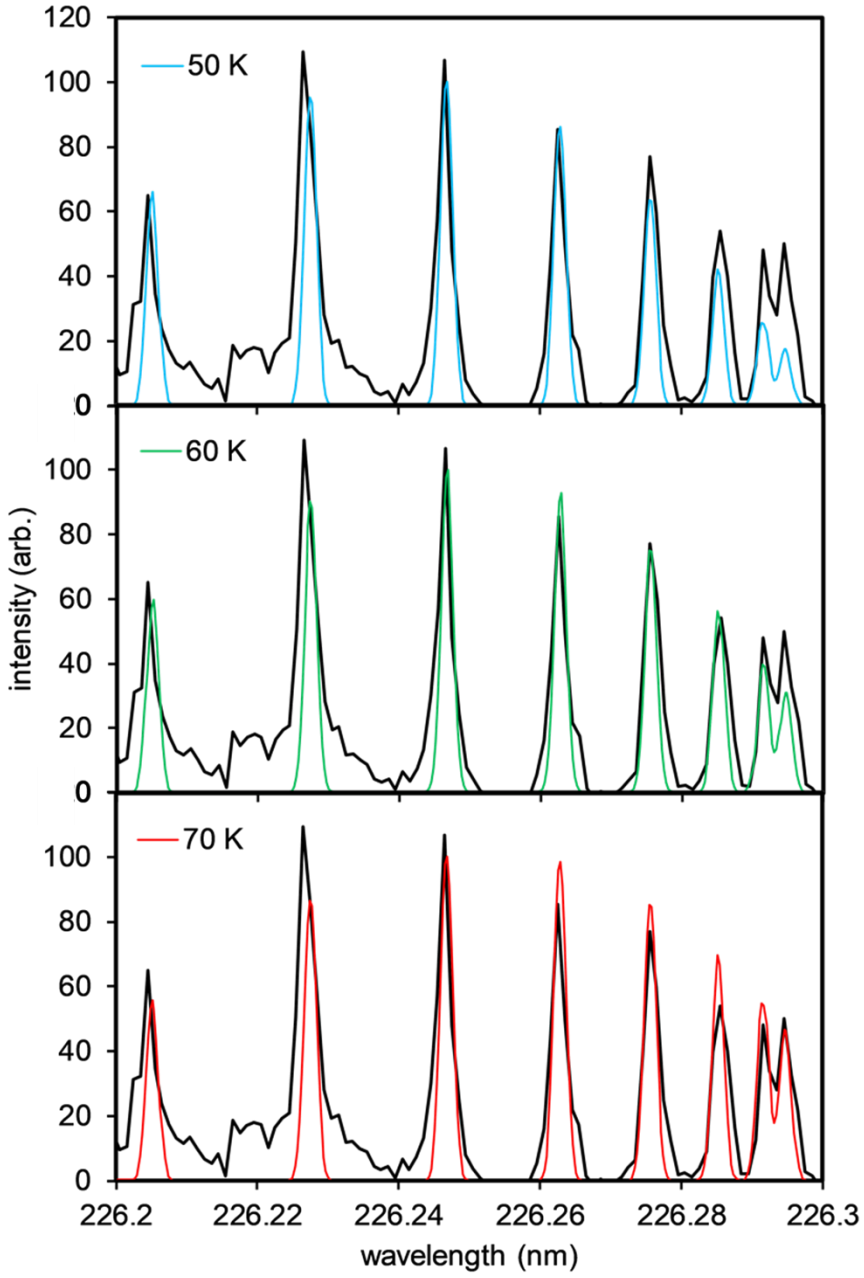


Figure 2.3. Experimental (black lines) and simulated (colored lines) spectra of the $P_1$ branch of the NO($A^2\Sigma^+$)←NO($X^2\Pi$) transition as measured using 1+1 REMPI. The simulations were generated in LIFBASE[52] using rotational temperatures of 50 K (top panel, blue), 60 K (middle panel, green), and 70 K (bottom panel, red).

### *2.1.2. Photolysis*

The 266 nm photolysis beam was produced by doubling the second harmonic of a Big Sky Ultra Nd:YAG laser. The photolysis beam was focused into the main chamber using a 30 cm focal length lens, and intersected the molecular beam at a 90 degree angle. The position of the focal lens was adjusted so the focus was just outside of the interaction region. The beam was defocused in the interaction region because image saturation occurred at higher power densities (see Figure 2.4). The low-power angular distribution has a $\beta_{eff}$ value of 1.5, in agreement with the measurements of Dylewski *et al.*[15] while the high-power angular distribution has a $\beta_{eff}$ of only 1.1.

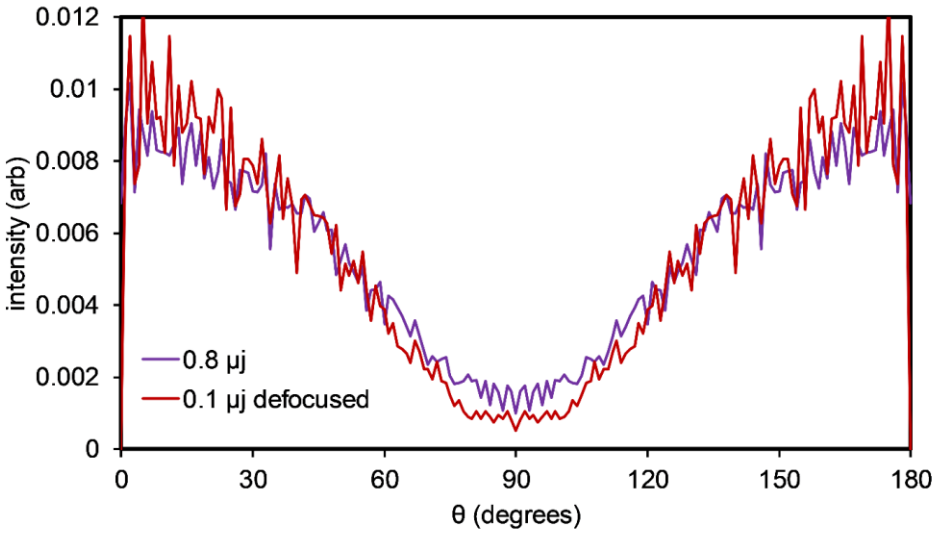


Figure 2.4. Angular distribution of $O_2(a^1\Delta_g, v=0, j=20)$ images taken at high and low power densities. Both images were taken in the S-branch at 70 K with a VH polarization geometry. The high-power angular distribution has greater intensity at node (around 90 degrees) than the lower-power image, indicating saturation in the high-power image. The $\beta_{eff}$ value for the high and low-power distributions are 1.1 and 1.5 respectively.

The 266 nm beam is linearly polarized and effectively orients the dissociating molecules in the laboratory frame. The probability of an absorption event is described by the following equation:

$$P = |E \cdot \mu|^2 = (|E||\mu|cos\theta)^2 \quad (2.1)$$

where $E$ is the electric field, $\mu$ is the transition dipole moment, and $\theta$ is the angle between $E$ and $\mu$. It can be seen from equation 2.1 that molecules with transition dipole moments parallel to the electric field of the laser have the highest probability of absorbing a photon. Consequently, the dissociating molecules are effectively oriented in the molecular frame in a $\cos^2\theta$ distribution. In the case of ozone photodissociation in the Hartley band, the dissociation time is much faster than the molecule's rotational period,[53-55] so the molecules remain aligned at the time of dissociation.

### *2.1.3. Ionization*

The resulting photofragments, either $O(^1D)$, $O(^3P)$, or $O_2(a^1\Delta_g)$, can be selectively ionized using 2+1 resonance enhance multiphoton ionization (REMPI). In the current study, we have focused on the state-selective ionization of $O_2(a^1\Delta_g)$. In the REMPI technique, the molecules are resonantly excited, and then are subsequently ionized. The resonant excitation step is responsible for the state selectivity of the technique. In a m+n REMPI scheme m photons are required for the resonant excitation step, and n photons are required to excite the molecule above the ionization threshold. As the REMPI schemes used in this dissertation

are 2+1 schemes, the resonant absorption step requires two photons, and the ionization step requires an additional photon of the same wavelength (prime symbols denote different wavelengths for the resonant and ionization steps). A diagram of the two schemes, $O_2(d^1\Pi, v=4) \leftarrow\leftarrow O_2(a^1\Delta_g, v=0)$ and $O_2(d^1\Pi, v=2) \leftarrow\leftarrow O_2(a^1\Delta_g, v=0)$ is shown in Figure 2.5. See Chapter three for a more detailed discussion of the spectroscopy. The $O_2(d^1\Pi, v=4) \leftarrow\leftarrow O_2(a^1\Delta_g, v=0)$ transition requires wavelengths around 302 nm, while the $O_2(d^1\Pi, v=2) \leftarrow\leftarrow O_2(a^1\Delta_g, v=0)$ transition requires wavelengths around 320 nm. Both wavelengths were produced by doubling the output of a LAS dye laser, pumped by a 150-10 Nd:YAG. To achieve wavelengths around 302 nm a mixture of Rhodamine 610 and Rhodamine 640 in methanol was used, and to achieve wavelengths around 320 nm DCM in methanol was used. The probe beam was aligned counterpropagating with respect to the photolysis laser and was focused into the chamber using a 30 cm focal length lens. Fragments of the desired $O_2(a^1\Delta_g, v, j)$ state were selectively ionized by tuning the probe wavelength. To monitor the relative timing of the photolysis and probe beams, a photodiode was placed near the chamber where it could simultaneously detect both laser beams. The typical delay times between the photolysis and probe lasers was 30 ns, but no appreciable change in signal was noticed between for delay times between 10 and 50 ns.

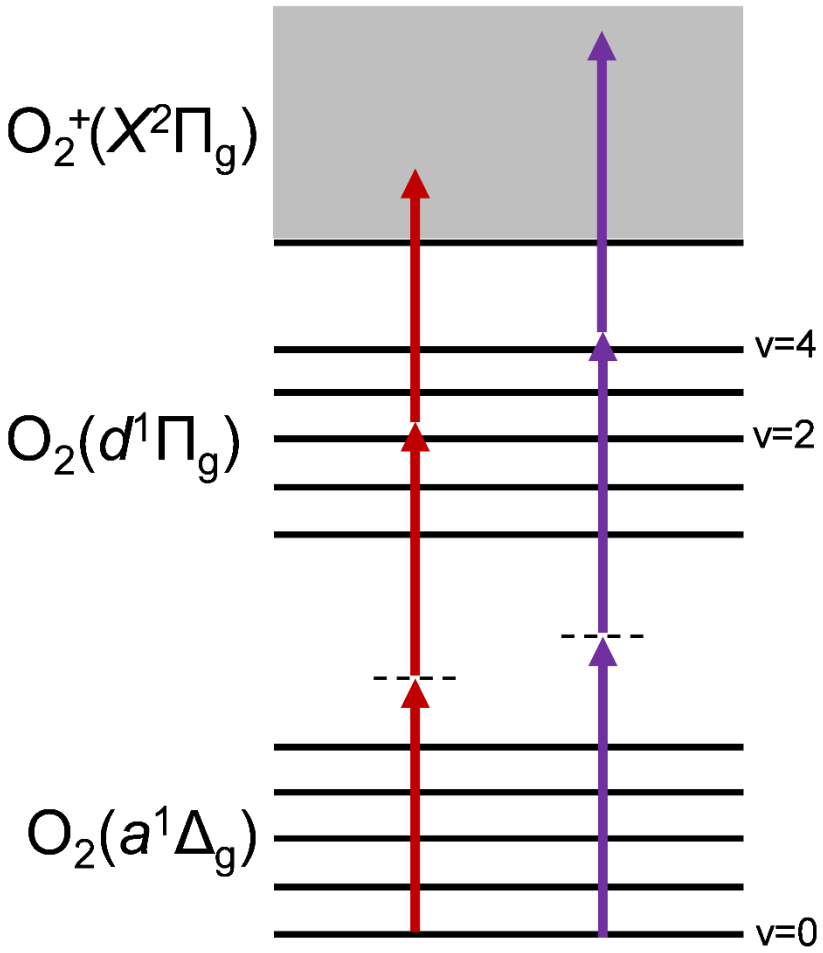


Figure 2.5. Schematic of the two 2+1 REMPI schemes used in this dissertation. The $O_2(d^1\Pi$, v=2) ← ← $O_2(a^1\Delta_g$, v=0) scheme is shown in red, and the $O_2(d^1\Pi$, v=4) ← ← $O_2(a^1\Delta_g$, v=0) scheme is shown in purple. Both schemes start with a two-photon resonant transition to the $O_2(d^1\Pi)$ state, followed the absorption of a third photon which results in ionization.

### *2.1.4. Detection*

A series of Einzel lenses, or ion optics, are used to accelerate the ionized fragments towards the detector. The ion optics are configured for velocity mapping, so that the position an ion hits the detector is a function of only its xy velocity, and not its initial position in the beam.[51] The chamber is equipped with four Einzel lenses, but only two are required for velocity mapping. The first lens, the repeller, has the highest voltage and determines the speed at which the ions move down the flight tube. The subsequent lenses are used to shape the ion cloud. Increasing the number of shaping lenses increases the control over the shape of the ion cloud. The voltages of these lenses are adjusted until the image is circular and the product radial distributions are narrow. Three ion optics were utilized in the experiments in this dissertation. Typical voltages used were 3000 V, 2652 V, and 2299 V, for the repeller, and first and second lenses respectively. The third lens was grounded.

The flight tube serves as a time of flight mass spectrometer, with an ion's arrival time depending on its mass to charge ratio $\left(t \propto \frac{1}{\sqrt{m}}\right)$. In order to selectively detect the fragments of interest, sufficient voltage to produce signal is applied to the detector only during the arrival time of the desired species. This prevents the detection of background ions with different mass to charge ratios than the fragment of interest. The detector consists of a pair of microchannel plates in a chevron configuration coupled to a P47 phosphor screen. When an ion hits the microchannel plate, a cascade of electrons is produced. The gain of the

microchannel plates is dependent on the voltage applied to the plates. During the arrival time of the fragments of interest, 2300 V is applied to the microchannel plate assembly, resulting in a gain $>10^6$. The rest of the time, 1000 V is applied to the assembly, where the gain is insufficient to produce detectable signal. The cascade of electrons hits the phosphor screen. If the sufficient voltage is applied to the microchannel plates, there will be enough electrons in the cascade to cause the phosphor to emit visible light. Two different methods were used to detect this light, based on the experiment. When collecting REMPI spectra, a Hamamatsu R928 photomultiplier tube (PMT) was used to count the emitted photons. The PMT was equipped with a neutral density filter. The typical voltage applied to the PMT ranged from 800 to 1200 V. When spatially resolved data was required, images of the phosphor screen were taken with a CCD camera. To increase resolution, a centroiding algorithm is used to reduce each emission event to a single pixel.[56]

## 2.2. Image Processing

### *2.2.1. Centering and Symmertrization*

Each quadrant of the image is effectively a separate experiment. Under perfect conditions, the four image quadrants will be identical. In practice, there are often distortions and variations in intensity that cause differences in the four quadrants. To account for this, images are often symmetrized. The image is

symmetrized through the use of two perpendicular mirror planes. This effectively creates four mirror images of the original image, as shown in Figure 2.6. The intersection point of the two mirror planes is adjusted until the four mirror images overlap. This occurs when the mirror planes intersect at the image center. The result is an image with four identical quadrants, with each quadrant being the sum of the four quadrants in the raw image.

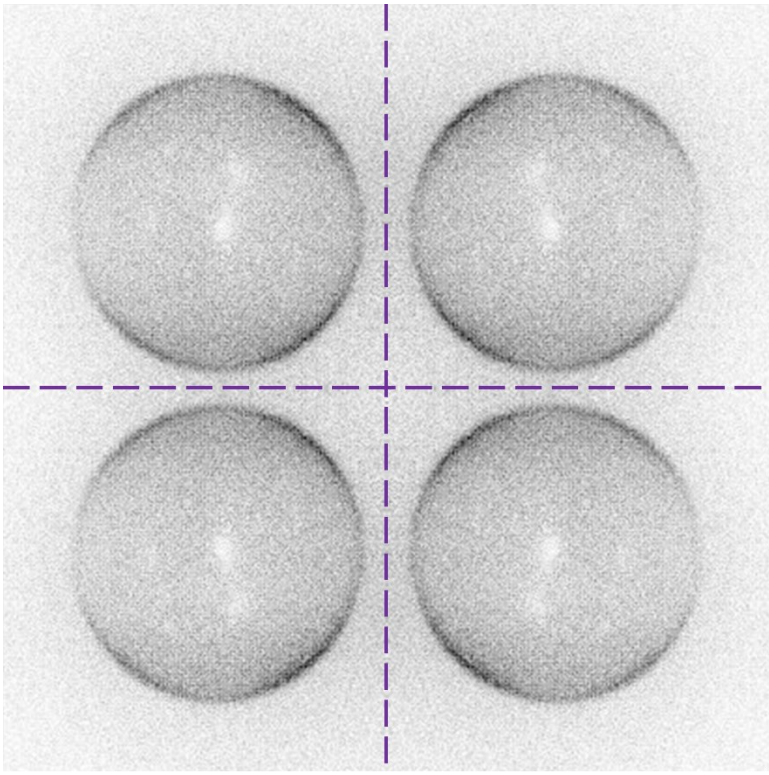

Figure 2.6. Example showing the four mirror images of the raw image, which are effectively overlapped during the symmetrization process. The location of the two perpendicular mirror planes are indicated by the dashed lines. When the intersection of the two mirror planes coincides with the image center, the result will be a single image where every quadrant is the sum of the original four quadrants. The image is of $O_2(a^1\Delta_g$, v=0, j=20) and was taken in the R-branch with VV polarization at 105 K.

### *2.2.2. Image Reconstruction*

All of the images shown in this dissertation are crushed images, meaning that the image is a 2D projection of the entire 3D ion cloud. Many algorithms exist to reconstruct the 3D ion cloud from this 2D projection. All of these algorithms assume that the 3D ion cloud is cylindrically symmetric about an axis parallel to the 2D projection, thus reconstruction methods are only valid for images taken with both the photolysis and probe beams linearly polarized in the imaging plane (VV geometry). To obtain the reconstructed image, the algorithm calculates the 2D cross section of the reconstructed sphere. The reconstruction algorithm used in this work is the polar onion peeling (POP) method.[57] The POP method takes advantage of the fact that for the largest radius signal (highest speed fragments), the angular distribution of the crushed image is equivalent to that of the 2D center slice. The largest radius signal is used to calculate the outer layer of the 3D ion cloud. The contribution from this layer is subtracted from the crushed image, and the process is repeated until the entire image has been processed. An example raw, symmetrized, and reconstructed image is shown in Figure 2.7. In this dissertation, angular distributions were extracted from raw images and radial distributions were extracted from reconstructed images. All images shown have been symmetrized unless stated otherwise.

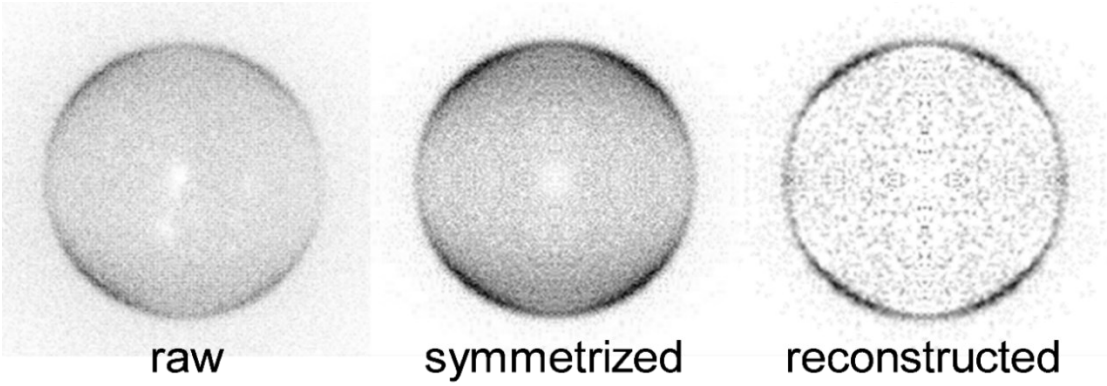


Figure 2.7. Image of $O_2(a^1\Delta_g, v=0, j=20)$ taken in the R-branch with VV polarization at 105 K shown in its raw, symmetrized, and reconstructed forms.

### *2.2.3. Radial Distribution*

The radial distribution of the image contains scalar information about both the detected and undetected fragment. The radial distribution is the signal intensity as a function of radius from the image center, and can be extracted from the reconstructed image. The radial distribution can be used to determine the speed of the detected fragments. Because the molecules with velocity in the xy plane are skimmed prior to photodissociation, the majority of the fragment velocity arises from the photodissociation event. A small amount of velocity is also imparted on the fragment during the ionization process, which is usually neglected. Due to its relatively small mass, the electron carries most of the kinetic energy after ionization. In the REMPI schemes used in this work, a recoil velocity of up to 11 m/s can be imparted on the $O_2$ fragment upon ionization.

The radial distribution is extracted in terms of intensity versus pixel. The radial distributions for the symmetrized and reconstructed images in Figure 2.7

are shown in Figure 2.8. The relationship between speed and number of pixels is linear and is dependent on the ion optic voltages and the length of the flight tube. The speed to pixel ratio is determined empirically by measuring fragments with known speeds. The speed of the detected fragment is determined directly from the radial distribution, and the speed of the cofragment can be calculated using conservation of linear momentum, i.e. $m_1v_1=m_2v_2$.

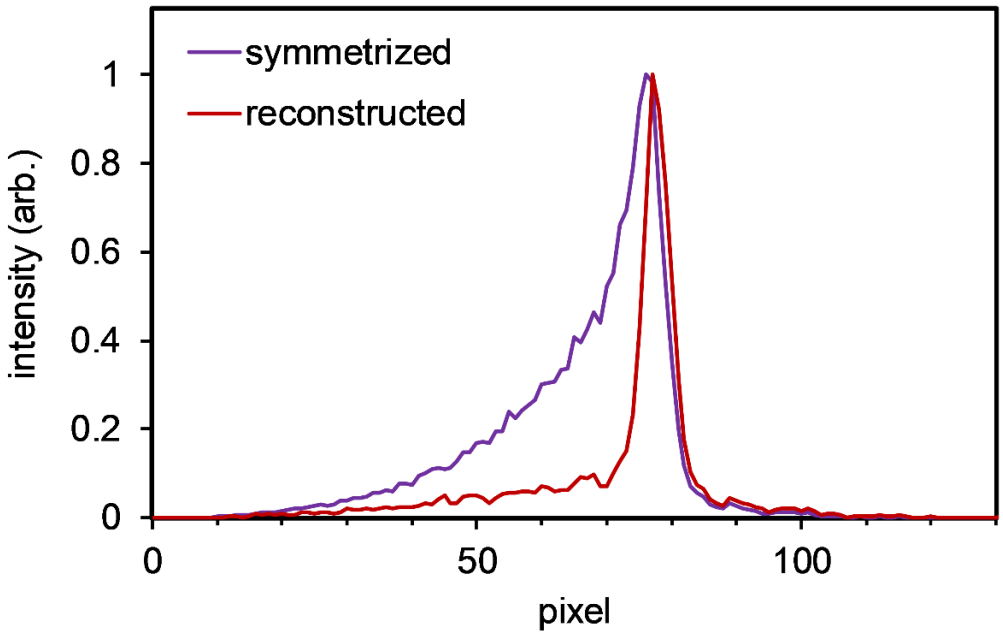


Figure 2.8. Radial distributions of the symmetrized and reconstructed images shown in Figure 2.7. Each pixel represents approximately 14.2 m/s.

One of the reasons velocity map ion imaging is such a power technique is it provides information about the coincident fragment as well as the detected

fragment. This is achieved through a conservation of energy analysis as described by the following equation:

$$E_{avail} = h\upsilon + E_{int}, AB = D_0 + E_{int}, A + E_{int}, B + E_{trans}, A + E_{trans}, B \qquad (2.2)$$

where $h\upsilon$ is the energy of the photon, $E_{int}, X$ and $E_{trans}, X$ are the internal and translational energy of species X, respectively, and $D_0$ is the bond energy. The total energy available to the system is equal to the sum of the photon energy and internal energy of the parent. The internal energy of the parent is often assumed to be zero because the molecular beam is jet-cooled. Alternately, an average parent internal energy can be calculated based on beam temperature. A portion of the available energy goes into breaking the bond, and the remainder goes into product internal and translational energy. Due to the state selectivity of the REMPI technique, the internal energy of the detected fragment is known. Using the speeds calculated from the radial distribution, the translational energy of both fragments can be calculated. Thus, the only unknown variable in equation 2.2 is the internal energy of the undetected fragment, which can be determined by rearranging the equation. The rovibronic state of the cofragment can often be inferred from its internal energy. The work in this dissertation focuses on the singlet dissociation channel, $O_3 \rightarrow O_2(a^1\Delta_g, v=0, j) + O(^1D)$. As $O(^1D)$ is the only spin-allowed cofragment for $O_2(a^1\Delta_g)$ resulting from ozone photodissociation in the Hartley band, images consisted of a single speed component.

### *2.2.4. Angular Distribution*

The angular distribution contains information about the vectors involved in the dissociation process. The angular distribution is the image intensity as a function of angle as shown in Figure 2.9. One method of obtaining the angular distribution is extracting it from the reconstructed image as a function of radius. This method was not possible for this work, because a majority of images were taken with laser polarizations that did not result in a cylindrically symmetric ion cloud and thus could not be accurately reconstructed. Fortunately, it has been shown that, for the signal at the largest radius, the angular distribution of the outer slice (5-9 pixels) of the crushed signal is equivalent to that of the reconstructed image.[58] As all of the $O_2(a^1\Delta_g)$ images analyzed consisted of a single speed component over a narrow range of radii, this method could be used to extract the angular distributions from the crushed images. The first step in angular distribution extraction is finding the image center. The center of the image was found using the procedure described in section 2.2.1. The angular distribution was then extracted from the raw image. The angular distribution for each quadrant was averaged, excluding any quadrants with significant distortion. The resulting angular distributions were analyzed to obtain vector correlations, as described in Chapter 4.

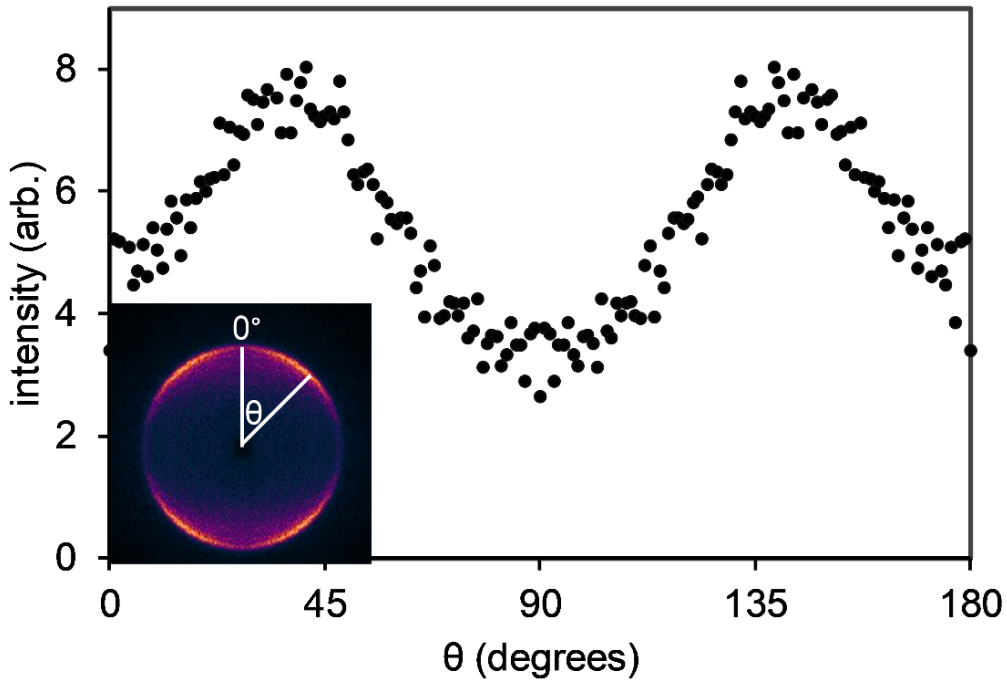


Figure 2.9. Angular distribution of the $O_2(a^1\Delta_g, v=0, j=20)$ image taken in the R-branch with VV polarization. Inset shows symmetrized image.

# 3. ROTATIONAL DISTRIBUTIONS*

## 3.1. REMPI Scheme

*Following the work of Valentini *et al.*[17] there have been multiple experimental studies characterizing the $O_2(a^1\Delta_g)$ photoproducts resulting from the UV photodissociation of ozone.[27-30, 59-61] These works, however, primarily focused on the vector properties of the photofragments and did not report $O_2(a^1\Delta_g)$ scalar distributions. This is likely the result of the REMPI scheme employed to detect the $O_2(a^1\Delta_g)$ photofragments. Similar to the work presented in this dissertation, these previous studies employed 2+1 REMPI via the $O_2(d^1\Pi_g) \leftarrow \leftarrow O_2(a^1\Delta_g)$ resonant transition. While previous studies utilized the v=1 and v=2 levels of the $O_2(d^1\Pi_g)$ state, this work also utilizes the v=4 state.

Of the low-lying vibrational levels of the $O_2(d^1\Pi_g)$ state, the v=4 level is particularly suited for use as in determining $O_2(a^1\Delta_g)$ rotational state distributions. While the v=0 level is relatively unperturbed, the $O_2(d^1\Pi_g, v=0) \leftarrow \leftarrow O_2(a^1\Delta_g, v=0)$ transition requires the use of a 2+2 REMPI scheme, in which both the resonant absorption and subsequent ionization steps involve two-photon transitions.[62] REMPI schemes involving a multiphoton ionization step are nonideal for use in the determination of product scalar distributions. In addition to requiring higher laser powers, multiphoton ionization steps are much less likely to be saturated

*Part of this chapter was reprinted with permission from Han and Gunthardt et al., *PNAS*, **accepted**, doi:10.1073/pnas.2006070117.

than single-photon ionization steps. For example, any *j*-dependent variations in the efficiency of the ionization step will lead to relative signal intensities that are no longer directly proportional to initial rotational state population and absorption probability. Unless the *j*-dependence of the efficiency of the ionization step is known, extraction of quantitative rotational state populations is not possible. In fact, the $O_2(d^1\Pi_g, v=0) \leftarrow \leftarrow O_2(a^1\Delta_g, v=0)$ spectrum exhibits anomalous intensities which arise from *j*-dependent resonances in the ionization step.[63] The v=1-3 levels of the $O_2(d^1\Pi_g)$ state are highly perturbed by the neighboring $O_2(II^1\Pi_g)$ state.[62] As can be seen in Figure 3.1, the vibrational spacing of the valance $O_2(II^1\Pi_g)$ state is much smaller than that of the Rydberg $O_2(d^1\Pi_g)$ state.

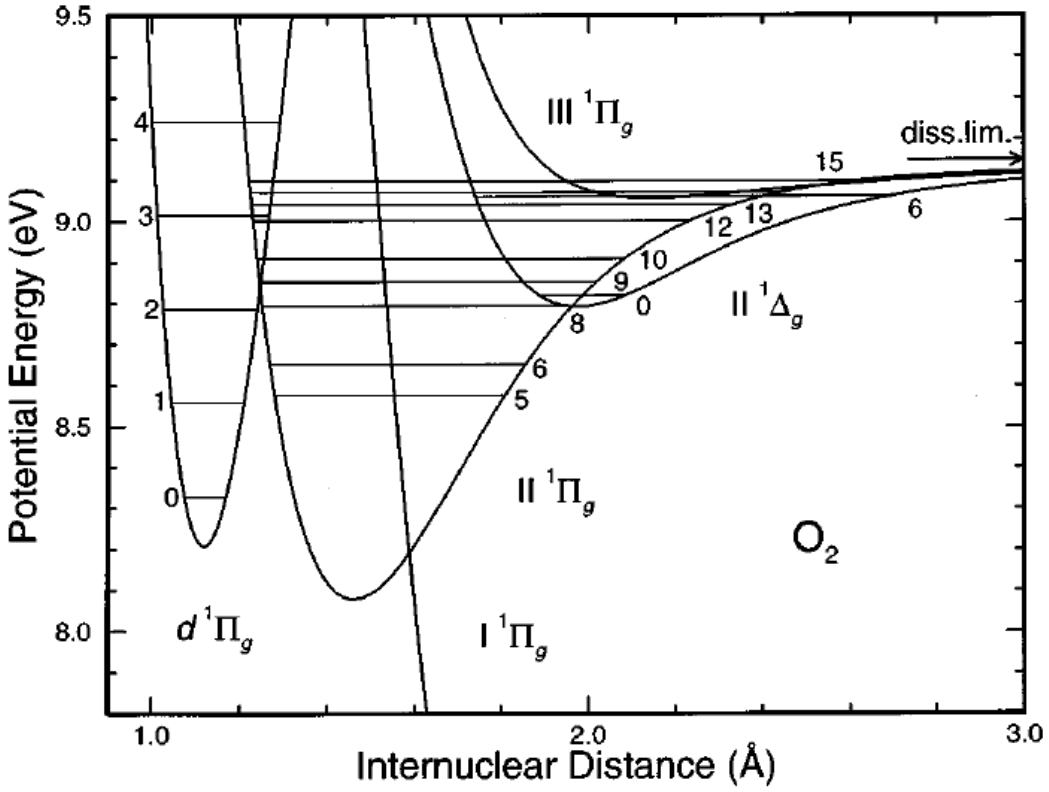


Figure 3.1. Diabatic potential energy curves for the $O_2(d^1\Pi_g)$ state and neighboring valence states. Figure reprinted from Lewis *et al.*, *J. Chem. Phys.* **111**, 186 (1999)[62] with the permission of AIP Publishing.

The difference in vibrational spacing arises because, as can be seen in Figure 3.1, the equilibrium internuclear distance for the $O_2(II^1\Pi_g)$ state is significantly larger than that for the $O_2(d^1\Pi_g)$ state. The $O_2(d^1\Pi_g, v=1\text{-}3)$ levels each have avoided crossings with multiple $O_2(II^1\Pi_g)$ vibrational states, leading to segmented spectra. These perturbations also lead to irregular intensities in the spectra which prevents the determination of an accurate $O_2(a^1\Delta_g)$ rotational state distribution if the $O_2(d^1\Pi_g, v=1\text{-}3)$ levels are used as the resonant state. As shown in Figure

3.1, the v=4 level of the $O_2(d^1\Pi_g)$ state lies above the dissociation limit of the $O_2(II^1\Pi_g)$ state and is thus largely unperturbed.[62] Accordingly, the v=4 level has regular rotational level spacing and the $O_2(d^1\Pi_g, v=4) \leftarrow\leftarrow O_2(a^1\Delta_g)$ spectrum does not exhibit anomalous intensity effects, making it a suitable candidate for determination of $O_2(a^1\Delta_g)$ rotational state distributions.

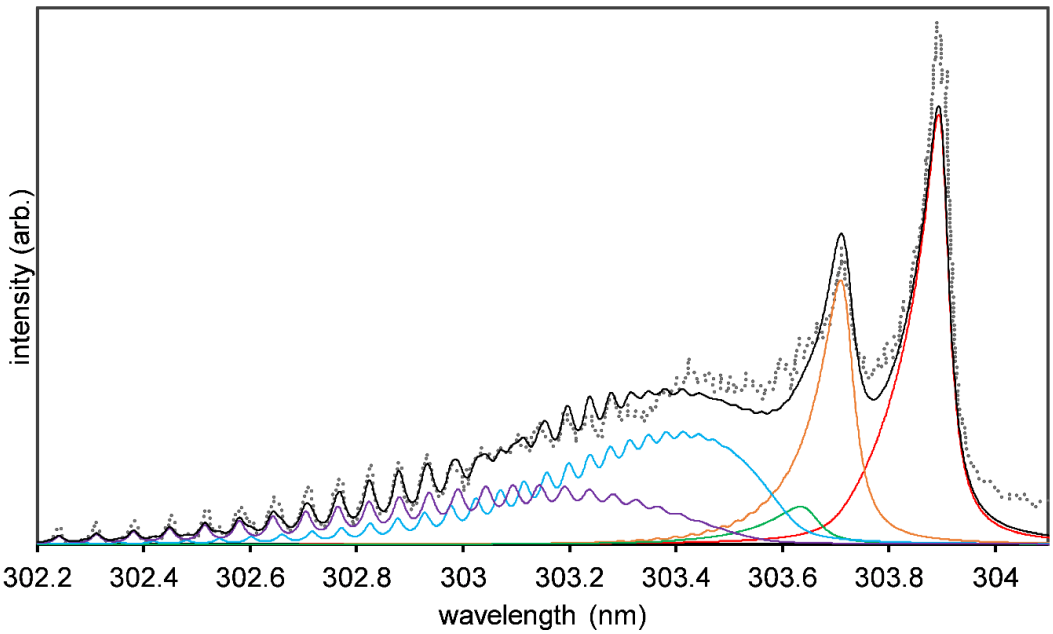


Figure 3.2. Experimental 2+1 REMPI spectrum via the $O_2(d^1\Pi_g, v=4) \leftarrow\leftarrow O_2(a^1\Delta_g, v=0)$ transition following the one-color photodissociation of ozone at 300 K (solid circles) and simulation (solid lines). In the simulation, the $O_2(a^1\Delta_g)$ rotational state distribution is approximated by a 300 K Boltzmann distribution. The simulation uses Lorentzian lineshapes with *j*-dependent linewidths (see section 3.5.2). The O-branch is shown in red, P-branch in orange, Q-branch in green, R-branch in blue, and S-branch in purple. The sum of all branches is shown in black. Experimental data from Morrill *et al.*[63]

We have verified the regular behavior of the 2+1 REMPI transition via $O_2(d^1\Pi_g, v=4) \leftarrow \leftarrow O_2(a^1\Delta_g, v=0)$ has been verified through the simulation of the one-color, ozone photodissociation, (4,0) spectrum published by Morrill *et al.*[63] The probe wavelength utilized in the $O_2(d^1\Pi_g, v=4) \leftarrow \leftarrow O_2(a^1\Delta_g, v=0)$ transition (~302 nm), is near the threshold for the singlet channel (~310 nm). Consequently, there is very little available energy for vibrational or rotational excitation of the $O_2(a^1\Delta_g)$ fragments, and most of the energy that goes into fragment rotation originates from parent rotational energy.[64] As Morrill conducted his one-color ozone photodissociation experiment at room temperature, it is expected that the resulting $O_2(a^1\Delta_g, v=0)$ rotational distribution will resemble a 300 K Boltzmann distribution. A spectral simulation using the term values and constants of Morrill *et al.* (see Table 3.1) and a 300 K Boltzmann rotational distribution provides excellent agreement with the experimental data (Figure 3.2).

Warter previously measured $O_2(a^1\Delta_g)$ rotational distributions arising from the photodissociation of ozone in a jet-cooled molecular beam, using 2+1 REMPI via the $O_2(d^1\Pi_g, v=4) \leftarrow \leftarrow O_2(a^1\Delta_g, v=0,1)$ transition.[26, 65] Distributions were measured for the v=0 and v=1 photoproducts resulting from photolysis at 248 and 266 nm, and the v=0 photoproducts resulting from photolysis at 282 nm. In these experiments, a bubbler with ozone trapped on silica beads was maintained at -50 C. The ozone was entrained in a flow of helium, with a backing pressure between 760 and 800 torr. The ozone/helium mixture was introduced into the ion imaging apparatus with a pulse valve, resulting in a molecular beam with a rotational

temperature of approximately 60 K. The probe and photolysis lasers were overlapped colinearly and intersected the molecular beam at 90 degrees. The phosphorescence from the detector was measured with a PMT. The REMPI spectra were each collected in segments, with multiple scans of each segment averaged together to increase signal to noise. The REMPI spectra were then fit using forward convolution simulation in order to determine the rotational distributions. Section 3.5 describes the improvements we have made to the experiment and simulation that allowed for the measurement of a more accurate rotational state distribution.

### 3.2. Spectral Simulation

Because $O_2$ is a diatomic molecule, the two-photon absorption spectroscopy depends on relatively few parameters and can, in principle, be simulated very precisely. If the ionization step in the 2+1 REMPI scheme is saturated and fast enough to compete with any predissociation in the final state, the 2+1 REMPI spectrum should be identical to the two-photon absorption spectrum. In a 2+1 REMPI scheme, the ionization step is often assumed to be saturated as it is a one-photon process, and experiments are conducted using the very high photon densities that are required for the two-photon absorption step. We have measured the power dependence for the S(30) peak and determined a dependence less than quadratic (see section 3.5.1) which indicates that saturation of the ionization step is a valid assumption for this experiment.

The first parameters needed for accurate simulation of the absorption spectrum of a diatomic molecule are the transition energies. If the final and initial vibronic states are sufficiently unperturbed, the transition energies can be calculated using the vibronic state energies and rotational constants. The initial vibronic states of the REMPI scheme used by Warter, $O_2(a^1\Delta_g, v=0,1)$, are fairly unperturbed. Rotational constants for the v=0 and v=1 levels of the $O_2(a^1\Delta_g)$ state were tabulated by fitting the term values provided by Morrill *et al.* using the following equation:

$$E(j) = T_{0v} + B_v j(j+1) - D_v j^2(j+1)^2 \qquad (3.1)$$

where E(*j*) is the term value (energy) of the given *j* state, $T_{0v}$ is the energy of the given vibronic state with respect to the energy of the $O_2(X^3\Sigma_g^-, v=0)$ state, and $B_v$ and $D_v$ are rotational constants. The resulting fits are shown in Figure 3.3, and the resulting constants are listed in Table 3.1. As discussed in section 3.1, the v=4 level of the $O_2(d^1\Pi_g)$ state is also sufficiently unperturbed. The simulation employed $O_2(d^1\Pi_g)$ rotational constants as determined by Morrill *et al.* using Equation 3.1. These constants are provided in Table 3.1.

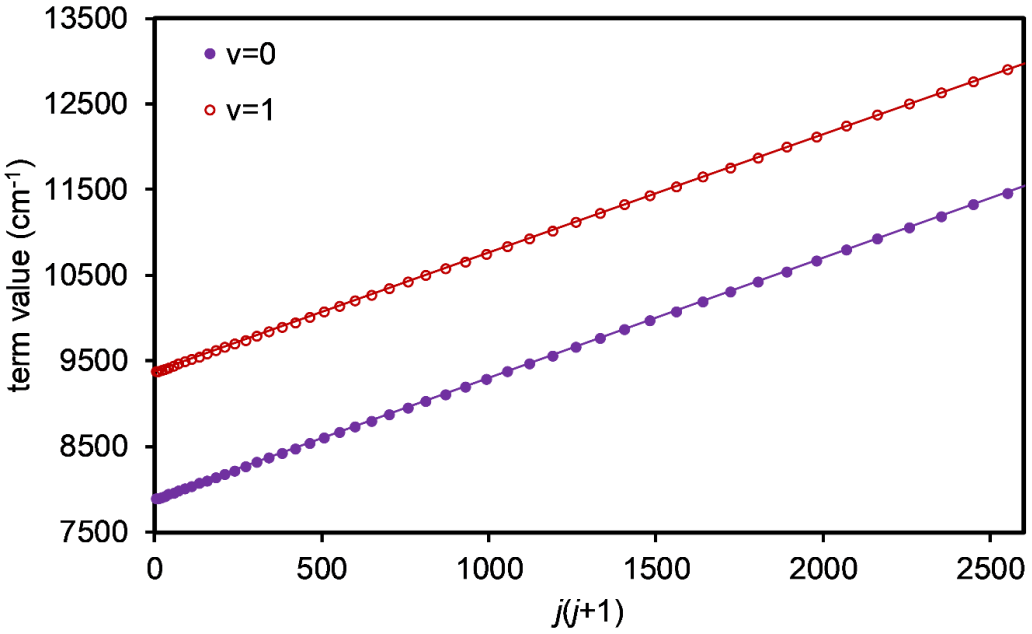


Figure 3.3. Term values for the v=0 (solid purple circles) and v=1 (open red circles) levels of the O2(a1Δg) state. The solid lines represent the best fit to Equation 3.1. Resulting constants are reported in Table 3.1. Term value data from Morrill *et al.*[63]

Table 3.1. Rotational constants used in the simulations in this Chapter, in $cm^{-1}$. Rotational constants for ($d^1\Pi_g$), and term values used in the calculation of rotational constants for ($a^1\Delta_g$) from Morrill *et al.*[63]

| vibronic state | | $T_{0v}$ | $B_v$ | $D_v$ |
|---|---|---|---|---|
| $a^1\Delta_g$ | v=0 | 7883.752 | 1.417839 | $5.0939 \times 10^{-6}$ |
| | v=1 | 9367.302 | 1.400792 | $5.1644 \times 10^{-6}$ |
| $d^1\Pi_g$ | v=4 | 73746.87 | 1.588308 | $4.7023 \times 10^{-6}$ |

Another set of parameters is needed to describe peak shape in the simulation. There are several mechanisms which serve to broaden each transition, resulting

in line profiles that can be described by Gaussian, Lorentzian, or Voight functions. Broadening mechanisms include lifetime broadening, pressure broadening, power broadening, and Doppler broadening. While lifetime, pressure, and power broadening all lead to Lorentzian lineshapes, Doppler broadening results in Gaussian lineshapes. A combination of Doppler broadening with lifetime, pressure, or power broadening will lead to Voigt line profiles. The Voigt profile is a convolution of the Gaussian and Lorentzian functions and is described by the following equation:

$$V(a,z) = \frac{a}{\pi}\int_{-\infty}^{\infty} \frac{e^{-(y)^2}}{a^2 + (z-y)^2}\,dy \qquad (3.2)$$

where $a = \sqrt{ln2}\,\frac{\Delta v_L}{\Delta v_D}$ and $z = 2\sqrt{ln2}\,\frac{(v_0 - v - \Delta)}{\Delta v_D}$. In the preceding equations, $\Delta v_L$ and $\Delta v_D$ are the FWHM of the Lorentzian and Gaussian functions respectively, $v_0$ is the unperturbed transition frequency, and Δ is the shift in experimental frequency with respect to $v_0$. Initial fits employed Gaussian lineshapes with *j*-independent linewidths, while it was later determined that Lorentzian lineshapes and *j*-dependent linewidths are more appropriate due to predissociation of the $O_2(d^1\Pi_g)$ state (see section 3.5.2).

The final set of parameters needed for the accurate simulation of a diatomic spectrum model is the transition intensities. The intensity of a transition is proportional to two variables: the transition probability and the population of the initial state. Bray and Hochstrasser have derived formulas for two-photon absorption linestrengths, which are a function of the orbital and rotational angular

momentum of the final and initial states. These formulas were used to tabulate the linestrength factors used in all of the simulations in this work and are provided in Appendix A. In the case of photodissociation, the initial state populations correspond to the nascent rotational state distribution, the determination of which is the goal of these experiments. If all of the other parameters are known, or can be empirically determined, initial populations can be obtained through a forward convolution simulation, as was done in this study.

### 3.3. Initial 266 nm, v=0 Rotational Distribution

The 2+1 REMPI spectrum of the $O_2(a^1\Delta_g, v=0)$ fragments following the 266 nm photolysis of jet cooled ozone (~60 K) reported by Warter and the initial fit are shown in Figure 3.4.[65] While the rotational distribution used in the simulation is the same as the distribution reported by Warter in her dissertation,[65] the overall fit is slightly different as a result of the correction of a small error in the calculated linestrength factors. The rotational distribution used in the simulation is shown in Figure 3.5.[26] For comparison, Figure 3.5 also includes the $O_2(a^1\Delta_g, v=0)$ rotational distribution reported by Valentini *et al.*[17] for the 266 nm photolysis of ozone at 300 K.

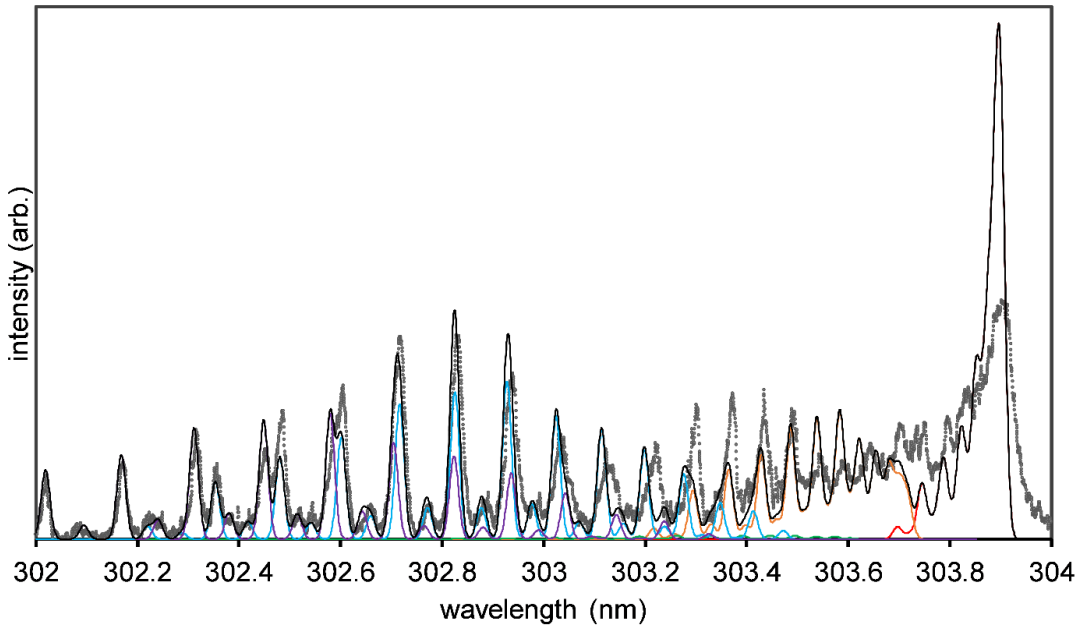


Figure 3.4. Experimental (solid circles) and simulated (solid lines) 2+1 REMPI spectrum via the $O_2(d^1\Pi_g, v=4) \leftarrow \leftarrow O_2(a^1\Delta_g, v=0)$ transition following the 266 nm photodissociation of ozone at 60 K. In the simulation, the O-branch is shown in red, P-branch in orange, Q-branch in green, R-branch in blue, and S-branch in purple. The sum of all branches is shown in black. The simulation uses Gaussian lineshapes and a constant linewidth of 4.5 $cm^{-1}$. The rotational distribution used in the simulation is shown in Figure 3.4. Experimental data from Warter.[65]

Compared to the distribution reported by Valentini *et al.*, the distribution reported by Warter *et al.* is shifted to lower *j* states. This apparent discrepancy was explained by the increased parent energy at 300 K compared to 60 K. The greater the internal energy of the parent molecules, the more energy available for fragment rotational motion. It is also apparent that the odd/even population alternation is significantly greater in magnitude in the 60 K distribution than in the 300 K distribution. The odd/even alternation observed in the other $O_2(a^1\Delta_g)$ rotational distributions measured at 60 K (248 nm v=0 and v=1, 266 nm v=1, and

282 nm v=0) was similar in magnitude to that observed in the 60 K 266 nm, v=0 distribution suggesting that the population alternation is temperature dependent.

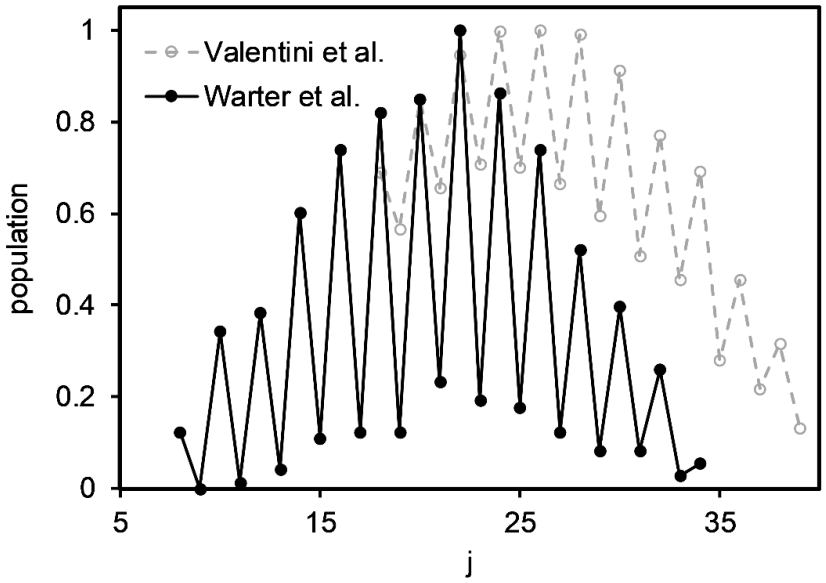


Figure 3.5. Rotational state distributions of the $O_2(a^1\Delta_g)$ photoproducts following the photodissociation of ozone at 60 K (black, closed circles), and 300 K (gray, open circles). 60 K data from Warter *et al.*[26] and 300 K data from Valentini *et al.*[17]

To test this theory, Warter *et al.* investigated the change in relative odd/even populations for different molecular beam temperatures.[26] As the temperature of the molecular beam is not constant throughout the length of the pulse, different temperatures could be accessed by changing the laser timing to dissociate in different regions of the pulse. As discussed in section 3.1, the v=2 level of the $O_2(d^1\Pi_g)$ state is highly perturbed. This perturbation results in odd state intensities

that are greatly enhanced compared to the even state intensities in the $O_2(d^1\Pi_g$, v=2) ← ←$O_2(a^1\Delta_g$, v=0) REMPI spectrum. This enhanced intensity makes the odd states easier to see and the relative changes in odd state population more intense, making the (2,0) spectrum particularly sensitive to changes in the relative populations of the odd and even rotational states. Warter *et al.* measured the (2,0) spectrum at two beam temperatures, 60 K and 200 K, and found that the relative population of the odd states increased with the increase in beam temperature, verifying the temperature dependence of the magnitude of the odd/even population alternation.[26]

### 3.4. Inconsistencies with the Curve-Crossing Model

The curve crossing model proposed by Valentini *et al.*[17] is inconsistent with the observed temperature dependence of the odd/even alternation. In the curve crossing model, the degree of odd/even alternation is directly tied to the singlet/triplet branching ratio. The model assumes that the singlet channel is depleted of odd-states because only molecules occupying odd rotational states can cross from the singlet channel to the triplet channel. Thus, the "missing" odd states in the $O_2(a^1\Delta_g)$ rotational distribution have crossed over to the triplet channel. Accordingly, an increase in magnitude of the odd/even alternation should correlate to an increased triplet yield. While it has been demonstrated that the magnitude of odd/even alternation is strongly temperature dependent, throughout most of the Hartley band (wavelengths < 310 nm) the triplet yield is approximately

10 percent, independent of temperature.[18, 19] Thus, the new evidence that the odd/even alternation is temperature dependent is inconsistent with the curve crossing model.

As will be elaborated on in Chapters 4 and 5, another model based on the preferential formation of one Λ-doublet is consistent with the observed temperature dependence. Due to symmetry restrictions involving the exchange of two identical nuclei, the A′ Λ-doublet can only occupy even rotational states while the A″ Λ-doublet can only occupy odd rotational states. Consequently, a preference for the formation of the A′ Λ-doublet would result in the preferential formation of fragments occupying even rotational states. As the B-state of ozone has A′ symmetry, in the absence of parent rotation, conservation of symmetry dictates the exclusive formation of $O_2(a^1\Delta_g)$ fragments in the A′ Λ-doublet. Parent rotation relaxes this restriction and allows for the formation of A″ fragments. This mechanism predicts increasing production of fragments occupying the A″ Λ-doublet, and thus odd rotational states, with increasing temperature, consistent with the observed experimental trend.

### 3.5. New Measurements of the 266nm, v=0 Rotational Distribution

New quantum dynamic calculations of the 266 nm $O_2(a^1\Delta_g, v=0)$ rotational state distribution prompted the remeasurement of the 266 nm experimental rotational state distribution. Comparison between experiment and theory (see Chapter 5) required an experimental rotational distribution that was more accurate

and had a quantitative assessment of uncertainty. This was accomplished by collecting and fitting the 2+1 REMPI spectrum of these photofragments via the $O_2(d^1\Pi_g, v=4) \leftarrow \leftarrow O_2(a^1\Delta_g, v=0)$ transition. Changes in both the experimental techniques and the fitting processes employed allowed for the quantitative determination of rotational populations.

### *3.5.1. Experimental Techniques*

The new experiments focused on the R and S-branch overlapping region (301.65 nm to 303.2 nm), because this region contains the most isolated peaks. As with the previous measurements, the REMPI spectrum was collected in segments. The segments were chosen in such a way that adjacent segments contained at least one shared peak. This enabled accurate scaling between segments.

As the threshold for the singlet channel is around 310 nm, the probe beam produced some one-color signal, as can be seen in Figure 3.6. The one-color photodissociation signal increases with increasing wavelength and is strongest at the O-branch bandhead. In addition to the one-color photodissociation signal, there is a small center feature resulting from non-resonant ionization of residual $O_2$ molecules in the ozone sample.

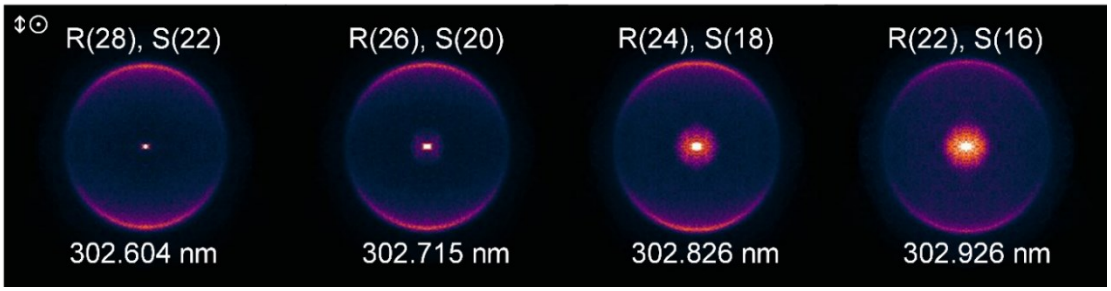


Figure 3.6. Image of overlapping R and S branch peaks. Images taken in the HV geometry. Outer ring is signal from $O_2(a^1\Delta_g)$ photofragments resulting from the 266 nm photodissociation of ozone. The larger inner circle is signal from $O_2(a^1\Delta_g)$ photofragments resulting from the photodissociation by the probe laser. The one color photodissociation signal increases with increasing wavelength. The bright center dot is signal from ionization of residual $O_2$ present in the molecular beam.

To keep the one-color photodissociation and ionization signal from contributing to the 266 nm photodissociation spectrum, a mask was employed between the phosphor screen and PMT. The mask consisted of black cardstock adhered to black, anti-reflective felt and was taped onto the backside of the phosphor screen, which is on the outside of the chamber. Any emission under the mask was blocked from reaching the PMT. To increase the signal to noise of the spectrum, in addition to masking the one-color signal, an outer mask was used to isolate the 266 nm photofragment signal. The purpose of this mask was to block the non-resonant background signal which primarily arose from the photolysis laser. A schematic of the mask is shown in Figure 3.7.

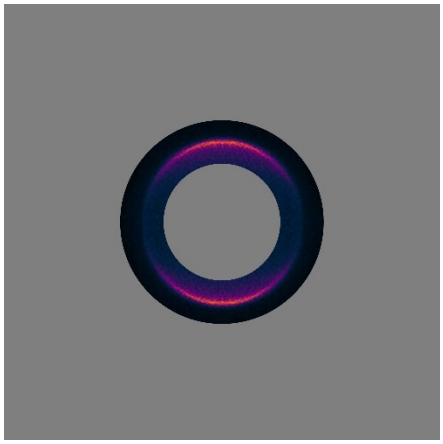

Figure 3.7. Schematic of mask superimposed on an image. The mask is represented in gray. Only the emission occurring between the outer and inner masks is visible to the PMT.

The power of the probe laser was attenuated to reduce power broadening of the REMPI peaks. The power broadening observed at higher laser powers blurs the peaks so clearly resolved odd peaks were not observed. Attenuation of the probe power allowed for the resolution of these peaks. To calculate photon flux at these higher laser powers, the diameter of the beam at the interaction region must be estimated. If it is assumed that the beam follows Gaussian beam optics and the focal point is in the interaction region, the beam waist diameter can be calculated according to the following equation:

$$2w_0 = \left(\frac{4\lambda}{\pi}\right)\left(\frac{F}{D}\right) \tag{3.3}$$

where $w_0$ is the diameter of the beam waist, $\lambda$ is the beam wavelength, $F$ is the focal length of the lens, and $D$ is the diameter of the beam when it hits the focusing lens. In this experiment the spot diameter of the 302 nm beam was approximately 2.5 mm when it reached the 30 cm focal length lens, leading to a beam waist

diameter of approximately 2.3 x $10^{-3}$ cm, corresponding to a cross-sectional area of approximately 420 $cm^2$. The maximum probe power used was approximately 3 mJ/pulse, so the photon flux at the interaction region is on the order of $10^{22}$ photons $cm^{-2}$ $s^{-1}$. The power broadening was first noticed when comparing scans with an iris allowing the entire beam to pass through and closed to the point where part of the beam is cut off, reducing the overall photon flux. As can be seen in Figure 3.8, closing the iris resulted in slightly narrower peaks, allowing for better resolution of the odd peaks. While using an iris to block some of the probe beam from reduces the overall number of photons reaching the chamber, the density of photons within the beam remains unchanged. Therefore, instead of reducing photon flux using an iris, in the final experiments attenuating optics were used to reduce the power (and thus photon flux) of the probe beam. Attenuating optics included a PEM and polarizer, both set to horizontal polarization, and a glass filter. These attenuating optics were used in all scans included in the final spectrum.

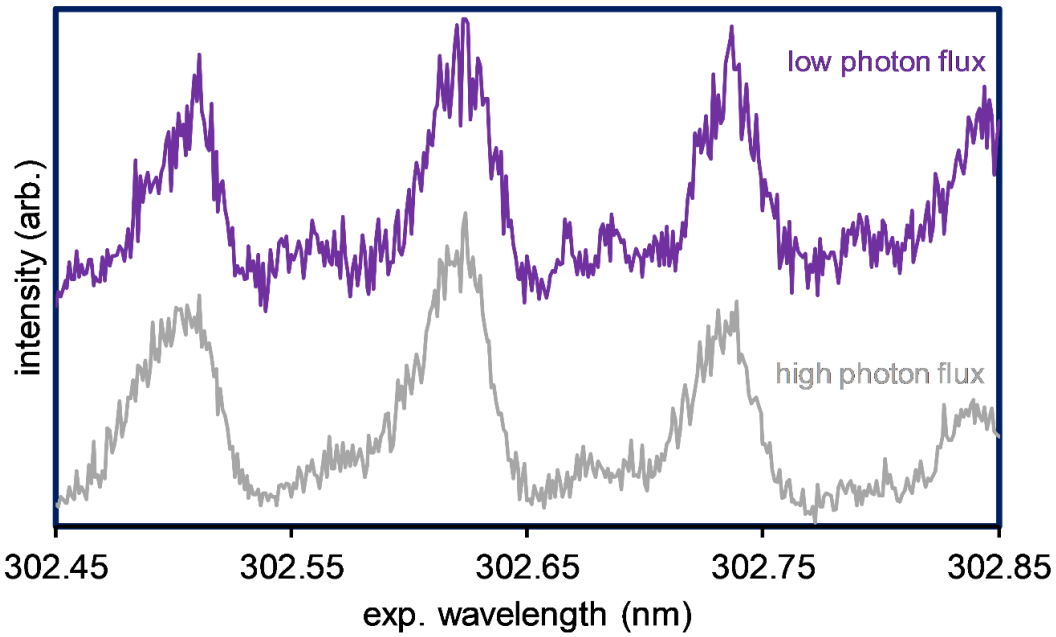


Figure 3.8. Two consecutive scans of the R(22 to 28) and S(16 to 22) overlapping region. The bottom scan (gray) was taken with the iris fully open, resulting in a high photon flux. The top scan (purple) was taken with the iris partially closed, resulting in a lower photon flux. This scan has been offset for clarity. The peaks in the bottom scan are slightly broader than the peaks in the top scan, resulting odd-j peaks that are less resolved than in the top scan.

As will be discussed in detail in the section 3.5.2, the main mechanism of peak broadening in the spectrum is lifetime broadening due to predissociation of the $O_2(d^1\Pi_g)$ state.[66] Lifetime broadening is Lorentzian in nature and can be described by the following equation:

$$L(v) = \frac{1}{\pi} \frac{\frac{1}{2}\Delta v_L}{(v - v_0)^2 + (\frac{1}{2}\Delta v_L)^2} \tag{3.4}$$

where $\Delta v_L$ is the FWHM and $v_0$ is the transition frequency. Compared to Gaussian functions, Lorentzian functions have significant intensity in the wings (see Figure 3.9), which results in significant overlap of adjacent peaks, and thus a spectrum

with greater signal between peaks.

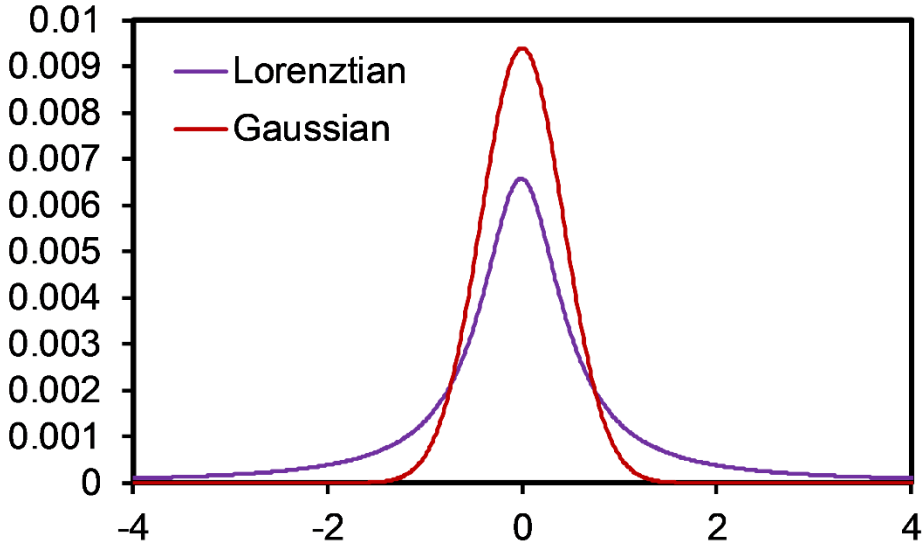


Figure 3.9. Area normalized Lorentzian and Gaussian functions, each with a FWHM value of 1.

Because of this, exact background correction was critical to obtaining an accurate spectrum. Several approaches were tried in order to determine the appropriate choice of parameters for the background scan. One method involved collecting a scan with both the photodissociation and probe lasers on, but the pulse valve off. This accounts for the background signal from both lasers, but does not include any pulse valve dependent one-color signal resulting from the probe laser. Another method involved collecting a scan with both the pulse valve and probe lasers on, but the photolysis laser off. This method captures the pulse-valve dependent and independent one-color signal from the probe laser, but does not

capture the background signal from the photolysis laser. Additionally, the pulse valve dependent one-color signal is more intense in this background scan than in a typical signal scan, because in the signal scan the majority of ozone molecules are dissociated by the 266 nm laser before the probe laser reaches the molecular beam. Initially, both types of background scans were collected and compared. Figure 3.10 shows consecutive background scans collected using the two different methods. It can be seen that both the two-color pulse valve-off scan and the one-color (probe), pulse valve-on scan have similar slopes. The two-color pulse valve-off scan signal is greater in intensity than that of the probe only pulse valve-off scan. The offset in intensity between the two scans can be explained by the lack or presence of the one-color, photolysis laser background.

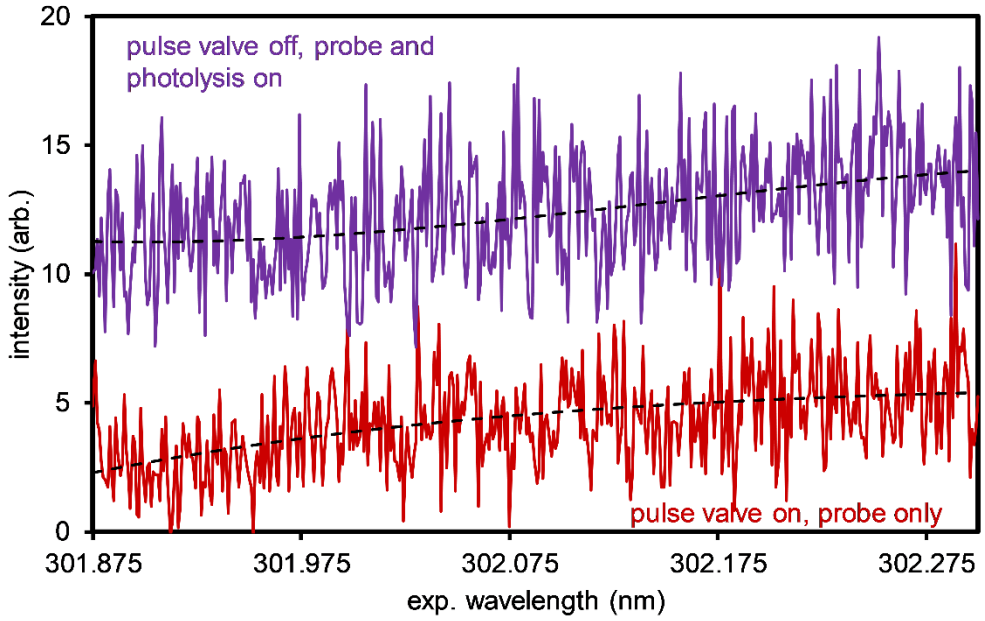


Figure 3.10. Comparison of two different background scan methods. The top (purple) trace was collected with the pulse valve off, and both the probe and photolysis laser on. The bottom (red) trace was collected with the pulse valve and probe laser on, and the photolysis laser off. Third-order polynomial fits of each trace are represented by black dashed lines.

The 266 nm one-color background is independent of probe wavelength, explaining why the two scans have similar slopes but are shifted in intensity. The fact that the slope does not change between the two methods suggests that there is not significant one-color, pulse valve dependent signal contributing to the scan. This inference is supported by the lack of structure in the pulse valve on, one-color scan. These trends are no longer observed once the probe power is above a certain threshold and the one-color signal increases in intensity. The use of relatively low probe powers, along with the central mask, successfully prevents the majority of the pulse valve dependent, one-color signal from contributing to the signal scans. In light of this, it was determined that pulse valve off, both lasers

on was the best combination to use for background scans.

A pulse valve-off, both lasers-on background scan was collected after every three to five signal scans. Conditions for these scans were identical (laser power, PMT voltage, attenuating optics, etc.), with the exception of turning the pulse valve off for the background scans. To background correct the signal scans, the corresponding background scan was fit with a third-order polynomial. The resulting polynomial was then subtracted from the appropriate signal scans. This method of background correction yielded spectra that were consistent from scan to scan, and day to day.

In addition to background correction, the signal scans also needed to be corrected for laser power changes over the scan. To complete the power correction, it was necessary to know the power dependence of the REMPI signal. To measure the power dependence, with the photolysis beam on, the probe wavelength was set to a mostly isolated S-branch peak, S(30). At each probe power a time scan (collects signal for a specified amount of time, laser wavelength stays constant) was taken for 30 seconds. For each scan, the average integrated PMT signal was calculated and recorded. Probe power was varied by adjusting the angle of the doubling crystal. Because the probe powers used in the experiment were less than 1.5 mJ/pulse, only data points for powers < 1.5 mJ/pulse were used in the fit. To extract the power dependence for the S(30) peak, a log-log plot was created, with $\log_{10}$(PMT signal) vs $\log_{10}$(probe power) (Figure 3.11). A log-log plot of a power curve will result in a linear function with a

slope equal to the power dependence. A linear regression was performed on the data points for powers < 1.5 mJ/pulse (solid circles), resulting in a power dependence of 1.7. A priori, a power dependence of 3 is expected for 2+1 REMPI as it is a 3-photon process. In practice, the power dependence is often less than 3, due to saturation or partial saturation of one or both of the steps. The most likely scenario for a power dependence below 2 is a fully saturated ionization step and a partially saturated absorption step. Evidence of further saturation is seen for powers > 1.5 mJ/pulse. A plot of PMT signal versus probe laser power is shown in Figure 3.12. For probe powers < 1.5 mJ/pulse the data points (closed circles) could be fit by the power curve (dotted line, $y=A*x^{1.7}$). The data points for probe powers > 1.5 mJ/pulse (open circles), fall below the power curve, indicating a power dependence below 1.7.

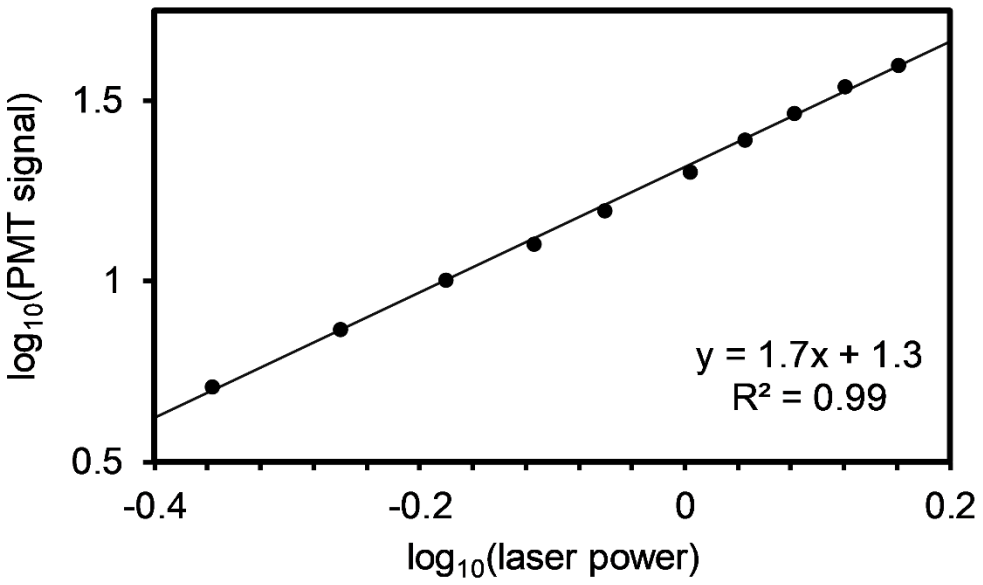


Figure 3.11. Log log plot of PMT signal versus probe laser power for S(30). Data points for powers < 1.5 mJ/pulse are represented as solid circles. The linear regression (solid line) indicates a power dependence of 1.7.

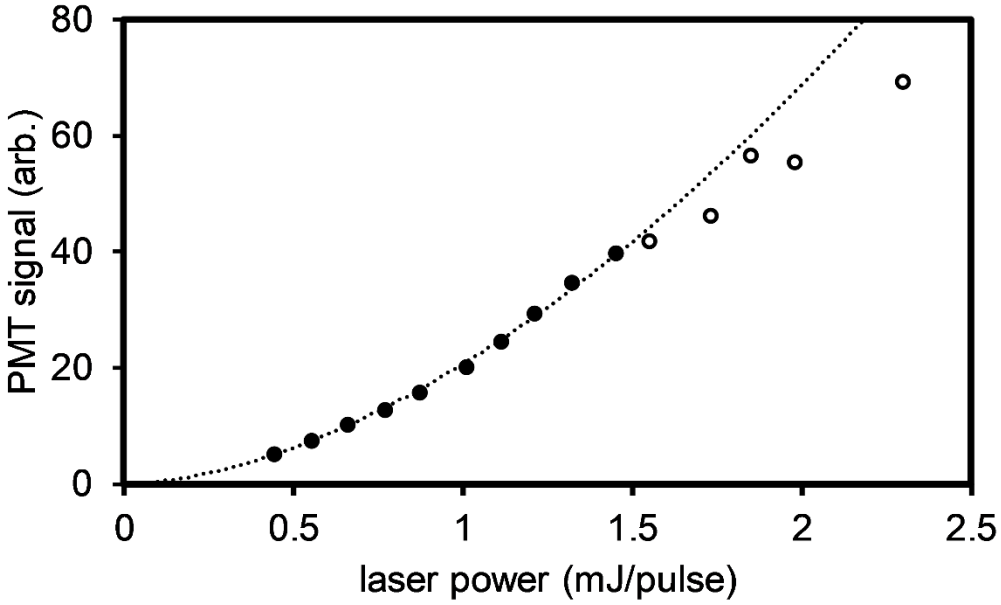


Figure 3.12. Power dependence of S(30). Photolysis wavelength of 266 nm, probe wavelength fixed at peak of S(30). Ion signal was measured by integrating PMT signal and probe laser power was measured with a power meter. Data points for powers < 1.5 mJ/pulse (closed circles) fit a power curve (dotted line). Data points at powers > 1.5 mJ/pulse (open circles) deviate from the power curve.

It is possible that the power dependence varies slightly with rotational branch and/or fragment rotational state. The only isolated peaks in the highly overlapped REMPI spectrum are the high-*j* S peaks, making power dependence measurements of other branches or lower *j* states difficult. It was found that the power correction for most scans was minor, and showed little dependence on the exact power dependence value used in the power correction step (see Figure 3.13). As can be seen in the bottom panel of figure 3.13 the maximum difference between the corrected scans using 1.4 and 2.0 power dependecies is around six percent. Because of this, no attempts to quantify any branch or *j*-dependence of the power dependence were made.

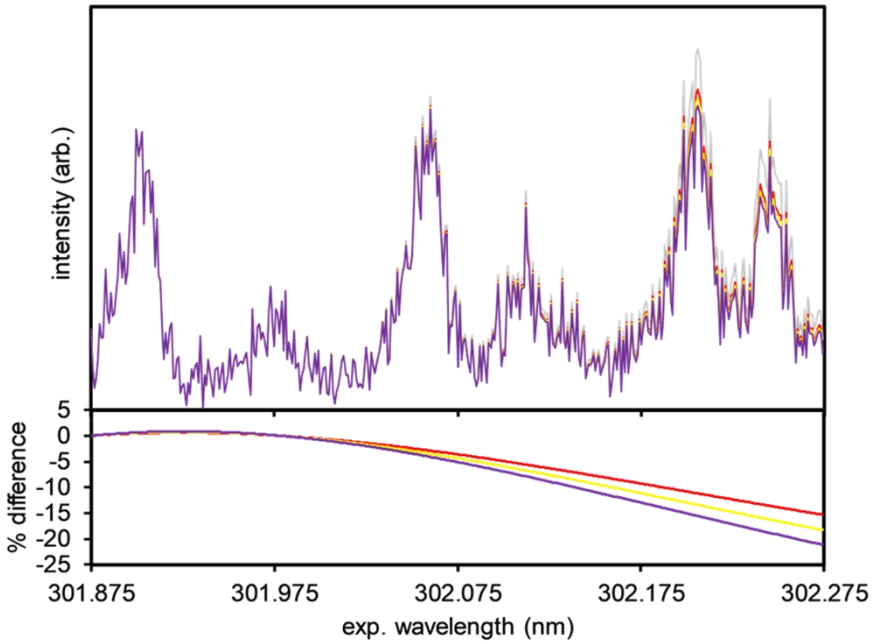


Figure 3.13. Effect of power dependence used in the power correction step on the final scan. Top panel: Gray trace is the background corrected scan, prior to power correction. Power correction of the gray trace leads to the colored traces, red using a power dependence of 1.4, yellow using a power dependence of 1.7, and purple using a power dependence of 2.0. It can be seen that the relative intensity difference between the power corrected traces is minor. Bottom panel: Percent difference between uncorrected and power corrected scans. Color assignment same as top panel.

For power correction scans, a photodiode was used to monitor the power of the probe laser. The photodiode was positioned to detect the probe light after it had exited the chamber. A UV-photodiode was used, so the beam could be detected directly, versus looking at the visible fluorescence from a business card. This eliminated the complication of photobleaching of a business card over time. To verify that the relationship between photodiode signal and laser power was linear, the laser power (as measured by a power meter) was compared to the corresponding photodiode signal for multiple different laser powers. Different probe powers were achieved by adjusting the angle of the doubling crystal. The

photodiode signal was integrated with a boxcar integrator, the output of which was sent to an analog to digital convertor. To obtain an average photodiode signal, the signal was measured for approximately 30 seconds and the average was taken of the resulting data points. A representative plot of integrated photodiode signal versus laser power is shown in Figure 3.14. and is well represented by a linear fit. The negative intensity of the lowest power point is due to inaccurate zeroing of the boxcar. While the exact slope of the photodiode signal versus laser power data changed from day to day, the numerical value of the slope does not factor into the power correction. What is important is the relative change in signal, which requires knowledge of the true offset, or zero, of the photodiode signal for accurate power correction.

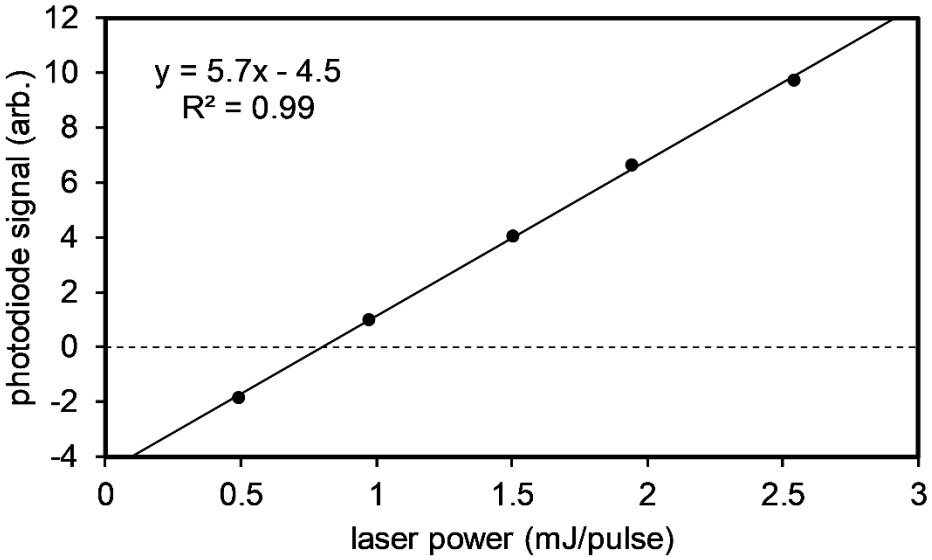


Figure 3.14. Relationship between integrated photodiode signal and probe laser power. The photodiode was set to view the probe laser as it exits the chamber. Photodiode signal was integrated with a boxcar integrator, and laser power was measured using a power meter.

Because of the challenge of accurately setting a zero for the boxcar, as well as the tendency for the boxcar signal to drift throughout the experiment, an offset scan was taken before each signal scan. During the offset scan, the probe laser was physically blocked from reaching the chamber. The scan was run for about thirty seconds with the probe laser blocked. The average of the photodiode signal was found and taken as the zero point. During each signal scan, the signal from the PMT and photodiode as a function of probe wavelength were recorded simultaneously. The offset value was subtracted from each point in the photodiode trace resulting in a baseline corrected power trace. To power correct a scan, the power trace was fit with a third order polynomial. The spectrum is then power corrected using the following formula:

$$F(\lambda) = I(\lambda) / [P(\lambda)]^{1.7} \quad (3.5)$$

Where $I(\lambda)$ is the background corrected intensity, $P(\lambda)$ is the polynomial fit of the power trace, and $F(\lambda)$ is the power corrected intensity.

To increase the signal to noise of the spectrum, multiple scans of each section were coadded. Figures 3.15 and 3.16 show the individual baseline and power corrected scans and the coadded spectrum, respectively for the S(26 to 30) and R(32 to 37) region. For a given section the baseline and power corrected individual scans can be almost perfectly overlapped through scaling alone (no vertical shifting), indicating the power and baseline correction leads to consistent spectra. In the coadded spectrum shown in Figure 3.16, the S(27) peak appears as a clear shoulder on the R(34) peak. This shoulder is difficult to resolve in many of the individual scans.

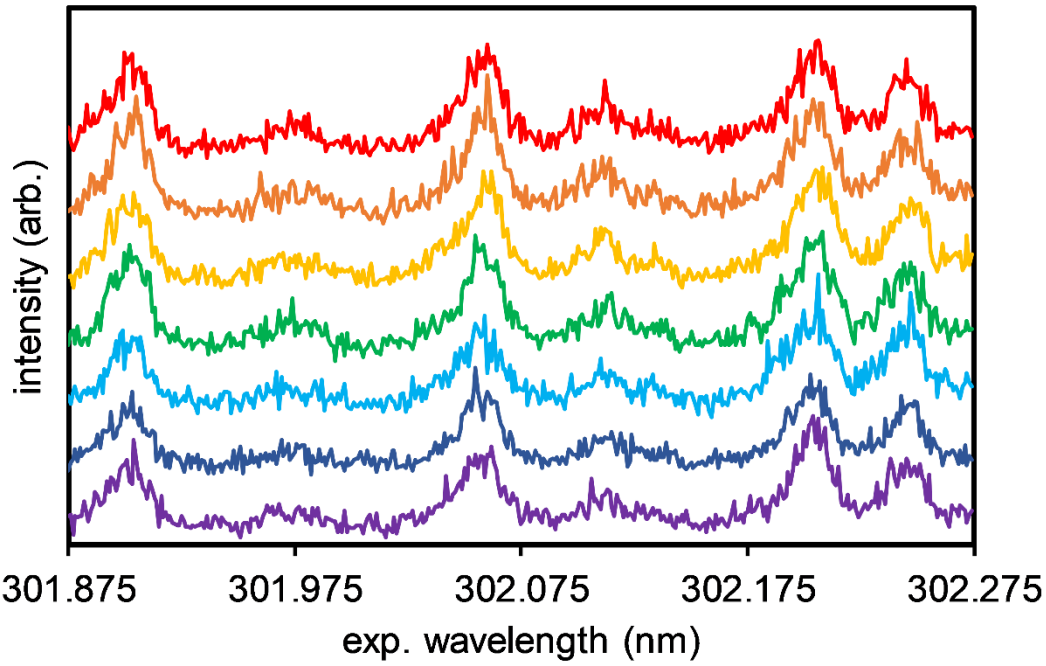


Figure 3.15. Individual baseline and power corrected scans for the S(26 to 30) and R(32 to 37) region. Scans are offset for clarity.

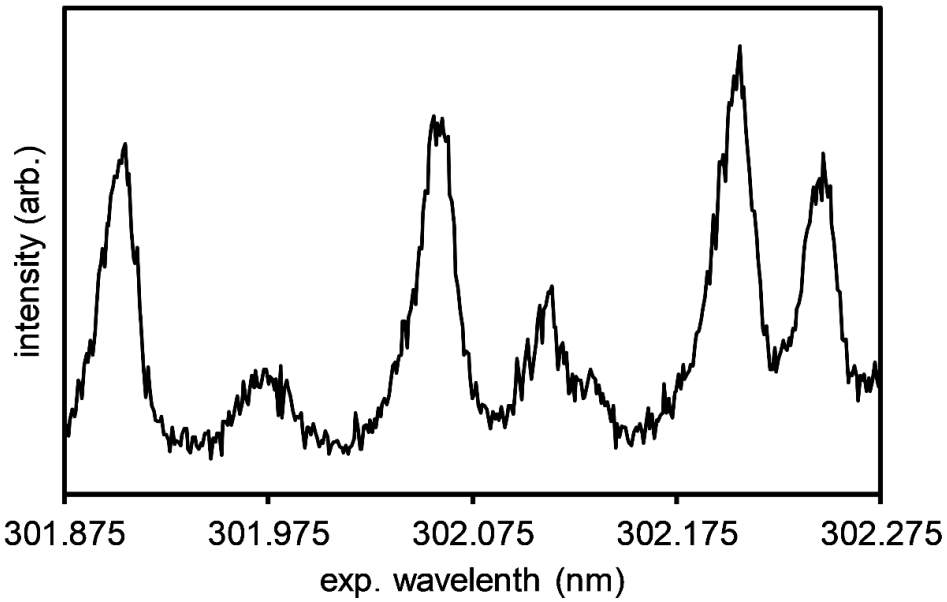


Figure 3.16. Sum of scans from figure 3.15.

Not only did the background and power corrected individual scans of a given section overlap almost perfectly without any vertical shifting, but so did the overlapping region of adjacent sections, as shown in Figure 3.17. Figure 3.17 shows the coadded spectrum for each individual section, which each section being represented by a different color. Again, these different segments were able to be almost perfectly overlapped through adjusting the individual scaling of each section. No vertical shifting was required, indicating that the background and power correction methods led to a reproducible baseline and spectrum. The individual segments shown in Figure 3.17 were combined into a single spectrum by averaging the overlapping regions. The resulting spectrum was fit using a forward convolution simulation method.

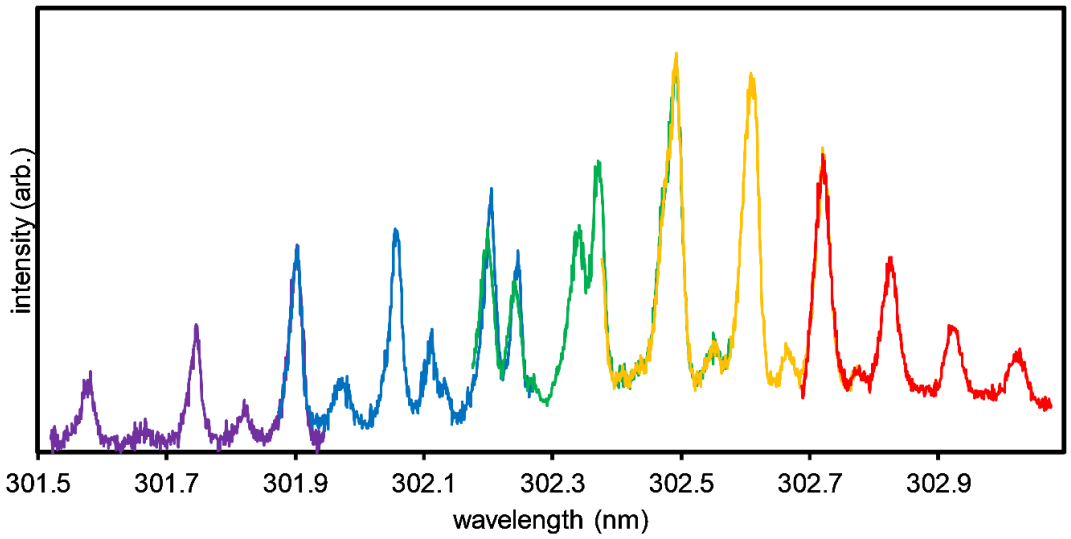


Figure 3.17. Overlapped, coadded sections shown in different colors. Individual sections were scaled to maximize overlap, but no vertical shifting was employed.

### *3.5.2. Fitting Techniques*

The greatest departure from the past analysis of Warter *et al.* in the fitting procedure concerned changes to the lineshape function. As stated above, the initial fits used Gaussian functions to simulate lineshape. The Gaussian contribution to the peaks arise from Doppler broadening, which can be described by the following equation:

$$\nu = \nu_0 (1 + v/c) \tag{3.6}$$

where $\nu_0$ is the transition frequency, v is the projection of the particle velocity along the probe axis, and c is the speed of light. Following ozone dissociation at 266 nm, the velocity of an $O_2(a^1\Delta_g, v=0, j=20)$ fragment is 1081 m/s, and the S-branch probe frequency is 33,036 $cm^{-1}$. According to Equation 3.3, the expected Doppler broadening in this case is 0.12 $cm^{-1}$. The experimental linewidths, on the other hand, are on the order of wavenumbers, indicating that other broadening mechanisms are more important. While the v=4 level of the $O_2(d^1\Pi_g)$ state lies above the bound levels of the $O_2(II^1\Pi_g)$ state, the v=4 state is still coupled to the continuum of the $O_2(II^1\Pi_g)$ state. This coupling results in the predissociation of molecules in the v=4 level of the $O_2(d^1\Pi_g)$ state.[66] Using translational energy spectroscopy, van der Zande *et al.* studied the lifetime broadening of rotational peaks in the v=4 level of the $O_2(d^1\Pi_g)$ state, and obtained linewidths similar to those observed in this experiment. This suggests that the primary mechanism of broadening in the $O_2(d^1\Pi_g, v=4) \leftarrow\leftarrow O_2(a^1\Delta_g, v=0,1)$ transition is lifetime broadening due to predissociation of the $(d^1\Pi_g, v=4)$ state. Lifetime broadening

results in a Lorentzian line profile. Strictly speaking, the line profiles in the spectrum are Voight in nature, because the system undergoes both lifetime broadening (Lorentzian) and Doppler broadening (Gaussian), but because the Doppler broadening is expected to be an order of magnitude smaller than the lifetime broadening, the peak shapes are well approximated using a pure Lorentzian function. For comparison, the new 266 nm, $O_2(d^1\Pi_g, v=4) \leftarrow \leftarrow O_2(a^1\Delta_g, v=0,1)$ REMPI spectrum has been fit using Gaussian lineshapes (Figure 3.18) and Lorentzian lineshapes (Figure 3.19). A constant peak width of 4.5 $cm^{-1}$ was used in both fits. It can be seen that the fit using Lorentzian lineshapes does a much better job capturing the intensity between peaks, as well as the overall shapes of the peaks.

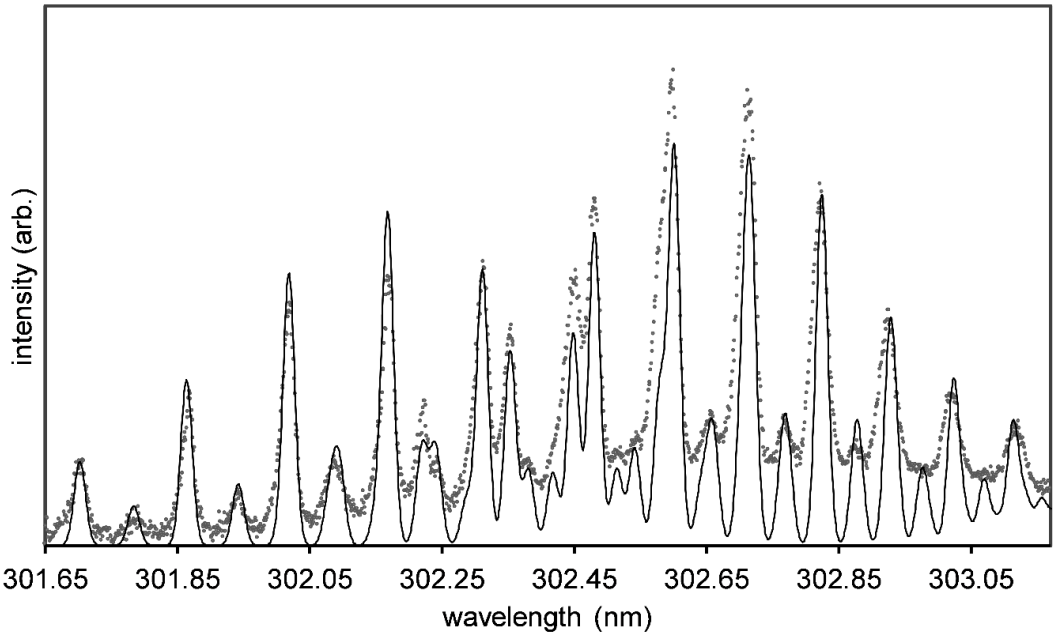


Figure 3.18. New 266 nm, $O_2$(a, v=0) REMPI spectrum (solid circles) and simulation (solid line) using Gaussian peaks with a constant FWHM of 4.5 $cm^{-1}$.

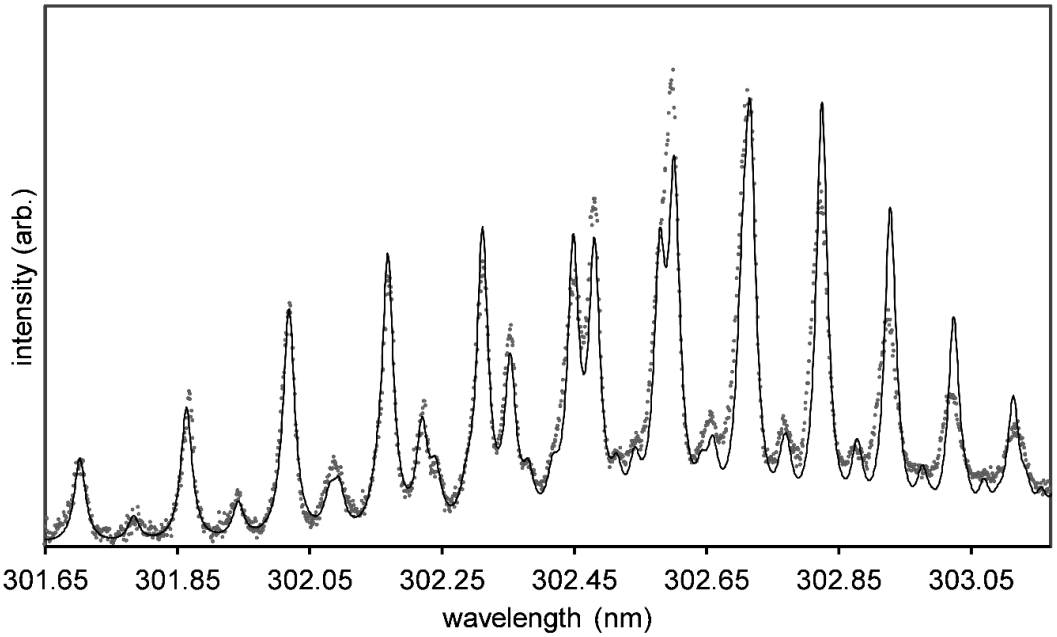


Figure 3.19. New 266 nm, $O_2$(a, v=0) REMPI spectrum (solid circles) and simulation (solid line) using Lorentzian peaks with a constant FWHM of 4.5 $cm^{-1}$. The rotational distribution used in the simulation is presented in Figure 3.22

The fit was further improved through the use of *j*-dependent linewidths. In the study by van der Zande *et al.* the authors saw evidence for *j*-dependent predissociation in their spectrum of the v=4 level of the $O_2(d^1\Pi_g)$ state.[66] They found that peaks for $j>20$ had widths corresponding to the detector resolution (10 $cm^{-1}$) and thus had natural linewidths < 10 $cm^{-1}$. The lower *j* peaks ($j<20$) had widths of approximately 10 to 13 $cm^{-1}$. These results suggest *j*-dependent linewidths, with linewidths decreasing with increasing *j*. In addition, van der Zande *et al.* calculated theoretical linewidths for a number of rotational states using Fermi's golden rule, and the theoretical values showed the same trend. The *j*-dependence arises due to changes in the overlap between the v=4 wavefunction and the continuum of the $O_2(II^1\Pi_g)$ state with rotational state. An empirical exponential decay based on linewidths from this study and from the study of van der Zande *et al.* was used to model the *j*-dependent linewidths in the simulations. As can be seen in Figure 3.20, employing *j*-dependent linewidths further improves the fit and better reproduces many of the peak shapes. As a second example, Morrill's one-color spectrum is shown fit with constant linewidths in Figure 3.21. The simulation in Figure 3.2, which uses the same *j*-dependent linewidths as Figure 3.20, agrees much better with the experimental spectrum than the fit in Figure 3.21.

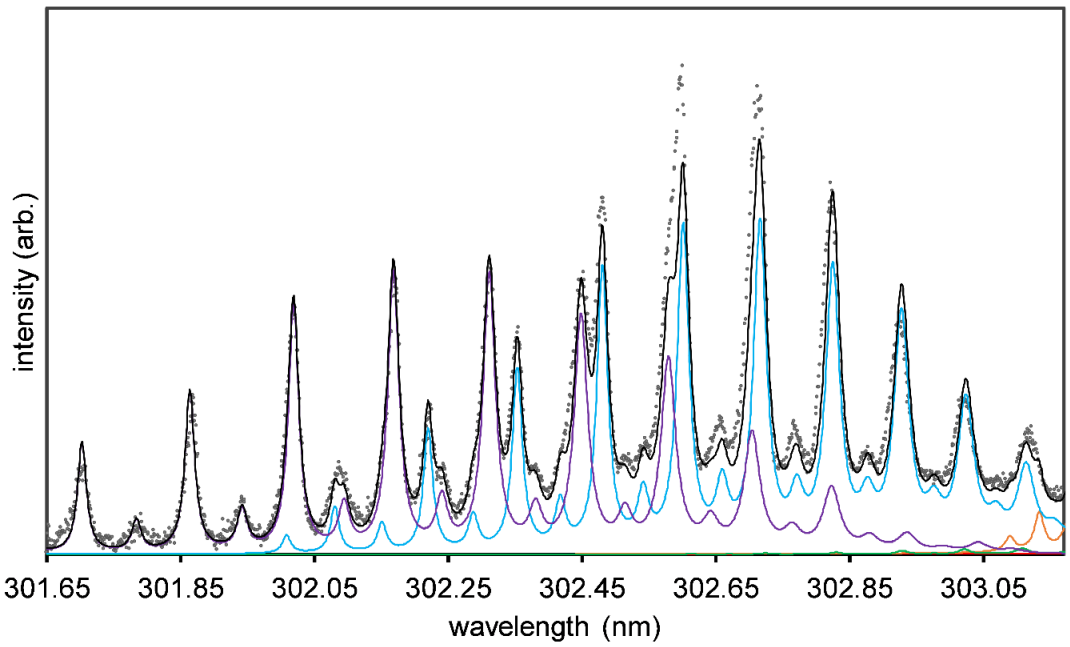


Figure 3.20. New 266 nm, $O_2$(a, v=0) REMPI spectrum (solid circles) and simulation (solid lines) using Lorentzian peaks with j-dependent FWHM values. The rotational distribution used in the simulation is presented in Figure 3.22 The S branch is shown in purple, the R branch in blue, the P branch in orange, and the sum of all branches in black. Figure reproduced from Han and Gunthardt *et al.*, *PNAS*, **accepted**, (2020) doi: 10.1073/pnas.2006070117.

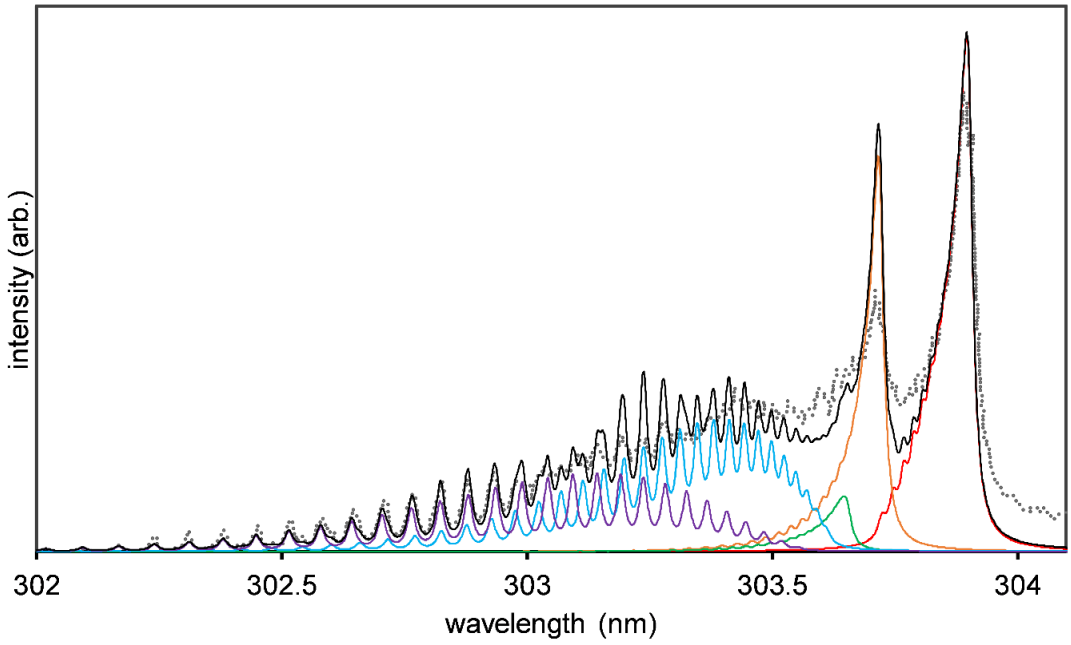


Figure 3.21. Experimental 2+1 REMPI spectrum via the $O_2(d^1\Pi_g, v=4) \leftarrow \leftarrow O_2(a^1\Delta_g, v=0)$ transition following the one-color photodissociation of ozone at 300 K (solid circles) and simulation (solid lines). In the simulation, the $O_2(a^1\Delta_g)$ rotational state distribution is simulated by a 300 K Boltzmann distribution. The simulation uses Lorentzian lineshapes with a constant FWHM of 4.5 $cm^{-1}$. The O-branch is shown in red, P-branch in orange, Q-branch in green, R-branch in blue, and S-branch in purple. The sum of all branches is shown in black. Experimental data from Morrill *et al.*[63]

The experimental rotational distribution and error bars were determined using a Monte Carlo approach. The experimental spectrum was first fit by eye by individually adjusting rotational populations in a forward convolution spectral simulation to generate an initial rotational distribution. For the Monte Carlo simulations, the population for each *j* state was determined by using a random number generator to select a value in between 50 and 150 percent of the corresponding best guess population. For each of these randomly generated rotational distributions, a simulated spectrum was calculated. The $\chi^2$ value for the

simulated and experimental spectra was calculated to assess goodness of fit. If the $\chi^2$ value is below a chosen threshold, the fit is considered acceptable and the rotational distribution was saved. This process was repeated until thousands of acceptable rotational distributions were accumulated. For each *j*, the populations from the acceptable rotational distributions were compiled into a histogram and fit with a Gaussian function. The final experimental rotational distribution populations were determined by taking the centerline of each best fit Gaussian and the error bars represent one standard deviation. The resulting rotational distribution is shown in Figure 3.22.

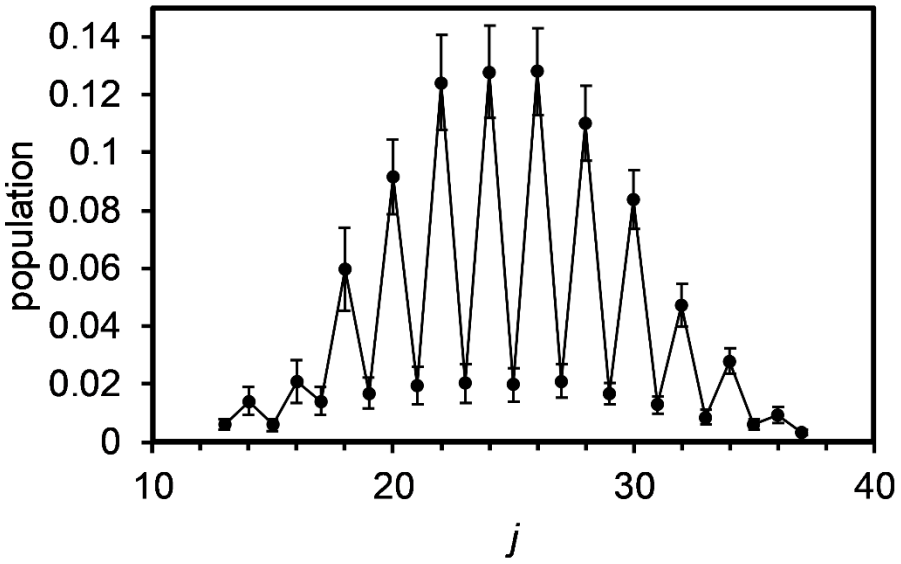


Figure 3.22. Quantitative rotational state distribution of the $O_2(a^1\Delta_g, v=0)$ fragments resulting from the 266 nm photodissociation of ozone at 60 K. Error bars represent one sigma.

### *3.5.3. Comparison of Old and New Rotational State Distributions*

Compared to the original rotational distribution depicted in Figure 3.4, the new distribution is slightly narrower and is shifted towards higher *j* states. The new distribution peaks in between *j*=24 and 26, while the previous distribution peaks at *j*=22. Both distributions show excellent agreement on the magnitude of the odd/even population alternation. The discrepancies between the two rotational state distributions can largely be explained by inaccurate baseline correction. The high-*j* regions of the R and S-branches in the original spectrum were baseline corrected to bring the intensity between peaks down to zero, artificially reducing the high-*j* intensities. As can be seen in Figures 3.4 and 3.18, the simulation using Gaussian peak shapes suggests that the intensity should be quenched in between peaks. In a simulation using Lorentzian peaks (Figures 3.19 and 3.20), it is apparent that there is significant intensity between peaks, due to the tailing of the Lorentzian function (see Figure 3.9).

## 3.6. Refitting Previous Spectra

The 248 nm v=0 and v=1, 266 nm v=1, and 282 nm v=0 spectra reported by Warter *et al.*[26, 65] were refit using Lorentzian lineshapes and the same *j*-dependent linewidths used in the new 266 nm, v=0 fit described in section 3.5.1. When fitting the spectra, more weight was given to regions that did not appear to be artificially baseline corrected. The resulting fits and rotational state distributions are shown in figures 3.23-3.30 below. While the quality of the fit was

improved upon refitting in all cases, the rotational distributions did not shift significantly from what was previously reported.[26]

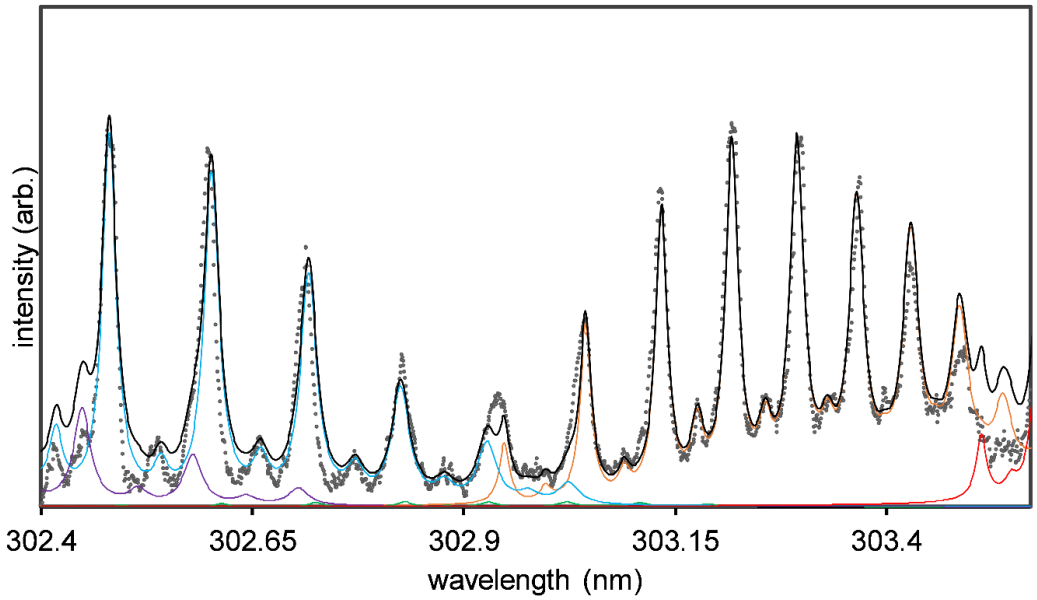


Figure 3.23. Experimental (solid circles) and simulated (solid lines) 2+1 REMPI spectrum via the $O_2(d^1\Pi_g, v=4) \leftarrow \leftarrow O_2(a^1\Delta_g, v=0)$ transition following the 248 nm photodissociation of ozone at 60 K. In the simulation, the O-branch is shown in red, P-branch in orange, Q-branch in green, R-branch in blue, and S-branch in purple. The sum of all branches is shown in black. The simulation uses Lorentzian lineshapes and *j*-dependent linewidths (see section 3.5.2). The rotational distribution used in the simulation is shown in Figure 3.24. Experimental data from Warter *et al.*[26]

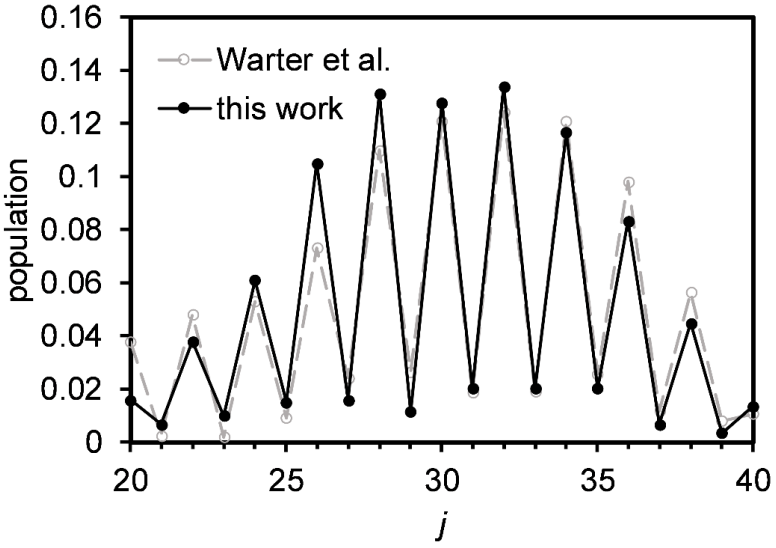


Figure 3.24. Rotational state distributions of the $O_2(a^1\Delta_g, v=0)$ fragments resulting from the 248 nm photodissociation of ozone at 60 K. Distribution from this work (black, solid circles) is compared to that published in Warter *et al.*[26]

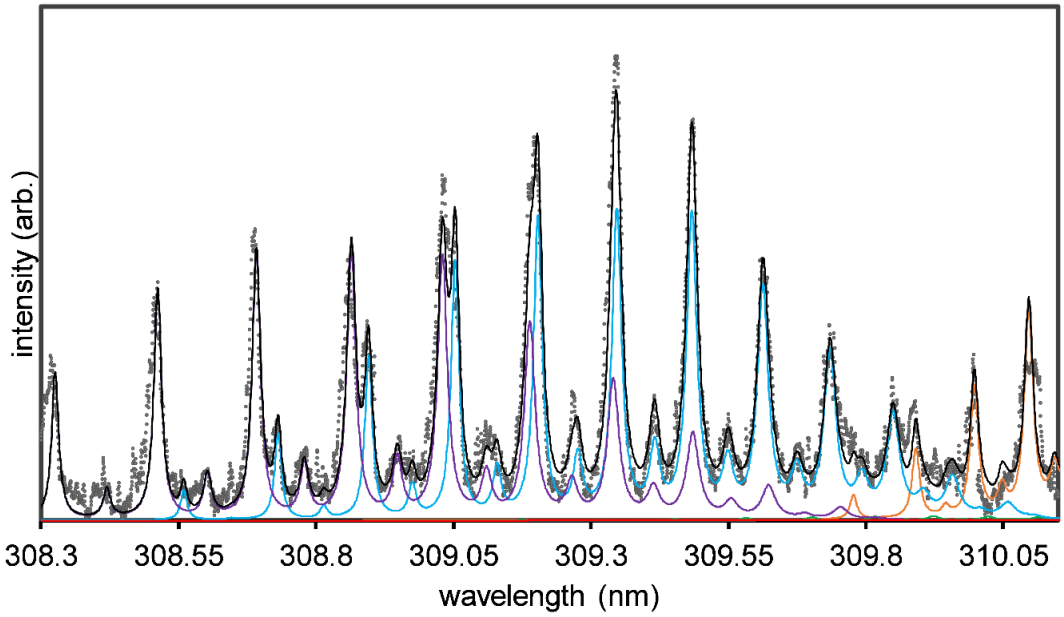


Figure 3.25. Experimental (solid circles) and simulated (solid lines) 2+1 REMPI spectrum via the $O_2(d^1\Pi_g, v=4) \leftarrow \leftarrow O_2(a^1\Delta_g, v=1)$ transition following the 248 nm photodissociation of ozone at 60 K. In the simulation, the O-branch is shown in red, P-branch in orange, Q-branch in green, R-branch in blue, and S-branch in purple. The sum of all branches is shown in black. The simulation uses Lorentzian lineshapes and *j*-dependent linewidths (see section 3.5.2). The rotational distribution used in the simulation is shown in Figure 3.26. Experimental data from Warter *et al.*[26]

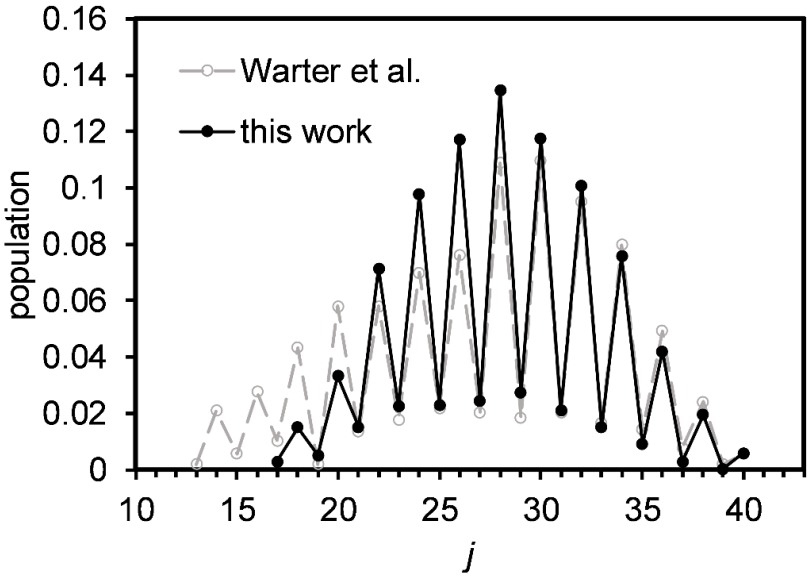


Figure 3.26 Rotational state distributions of the $O_2(a^1\Delta_g, v=1)$ fragments resulting from the 248 nm photodissociation of ozone at 60 K. Distribution from this work (black, solid circles) is compared to that published in Warter *et al.*[26] (gray, open circles).

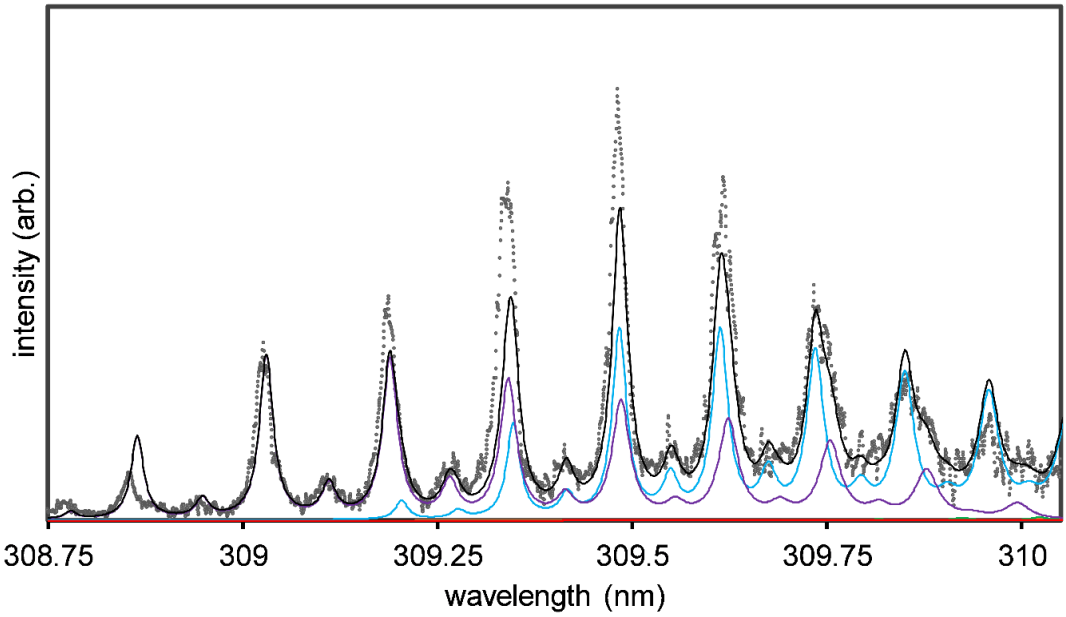


Figure 3.27. Experimental (solid circles) and simulated (solid lines) 2+1 REMPI spectrum via the O2(d1Πg, v=4) ← ←O2(a1Δg, v=1) transition following the 266 nm photodissociation of ozone at 60 K. In the simulation, the O-branch is shown in red, P-branch in orange, Q-branch in green, R-branch in blue, and S-branch in purple. The sum of all branches is shown in black. The simulation uses Lorentzian lineshapes and j-dependent linewidths (see section 3.5.2). The rotational distribution used in the simulation is shown in Figure 3.28. Experimental data from Warter.[65]

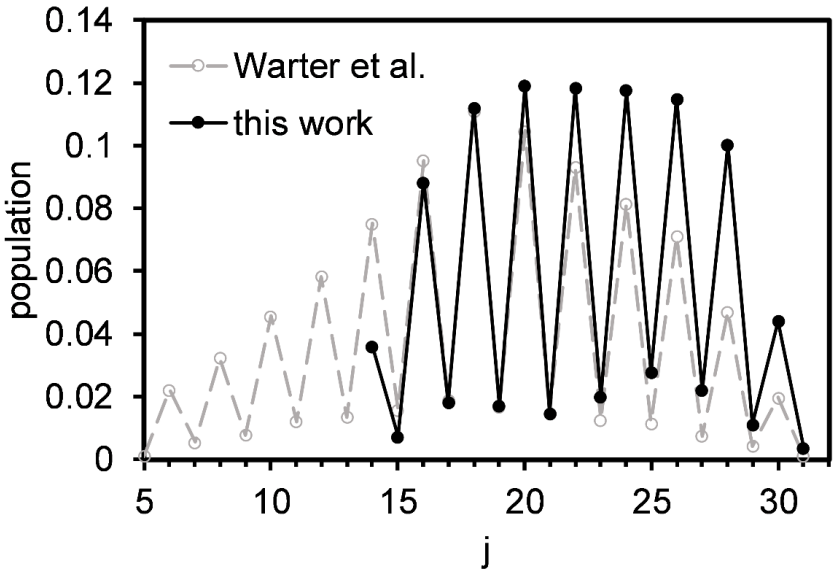


Figure 3.28. Rotational state distributions of the $O_2(a^1\Delta_g, v=1)$ fragments resulting from the 266 nm photodissociation of ozone at 60 K. Distribution from this work (black, solid circles) is compared to that published Warter *et al.*[26] (gray, open circles).

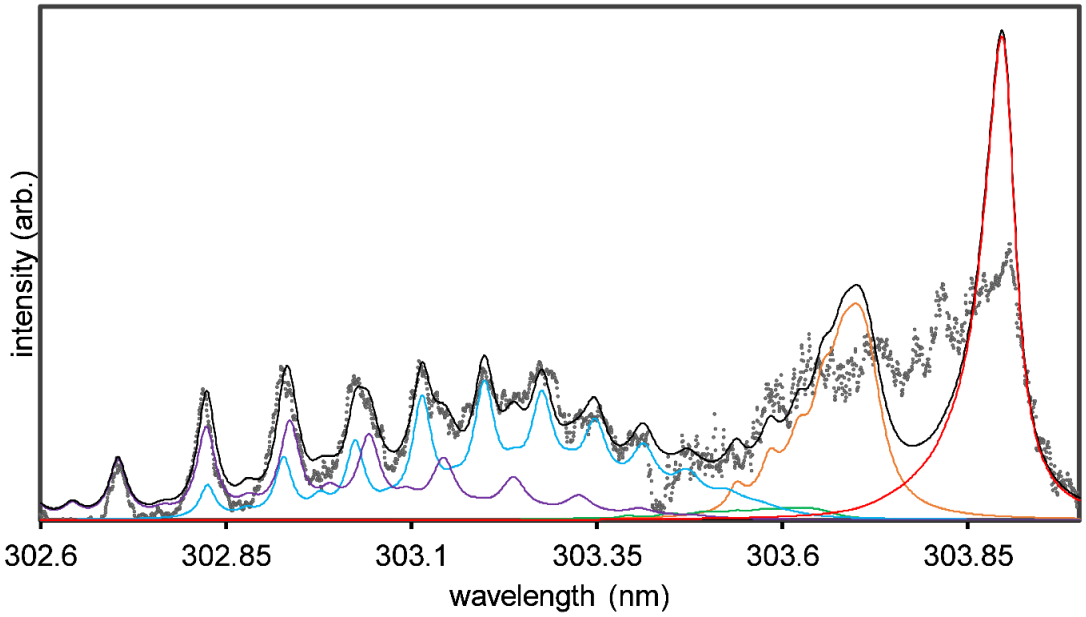


Figure 3.29. Experimental (solid circles) and simulated (solid lines) 2+1 REMPI spectrum via the $O_2(d^1\Pi_g, v=4) \leftarrow \leftarrow O_2(a^1\Delta_g, v=0)$ transition following the 282 nm photodissociation of ozone at 60 K. In the simulation, the O-branch is shown in red, P-branch in orange, Q-branch in green, R-branch in blue, and S-branch in purple. The sum of all branches is shown in black. The simulation uses Lorentzian lineshapes and *j*-dependent linewidths (see section 3.5.2). The rotational distribution used in the simulation is shown in Figure 3.30. Experimental data from Warter.[65]

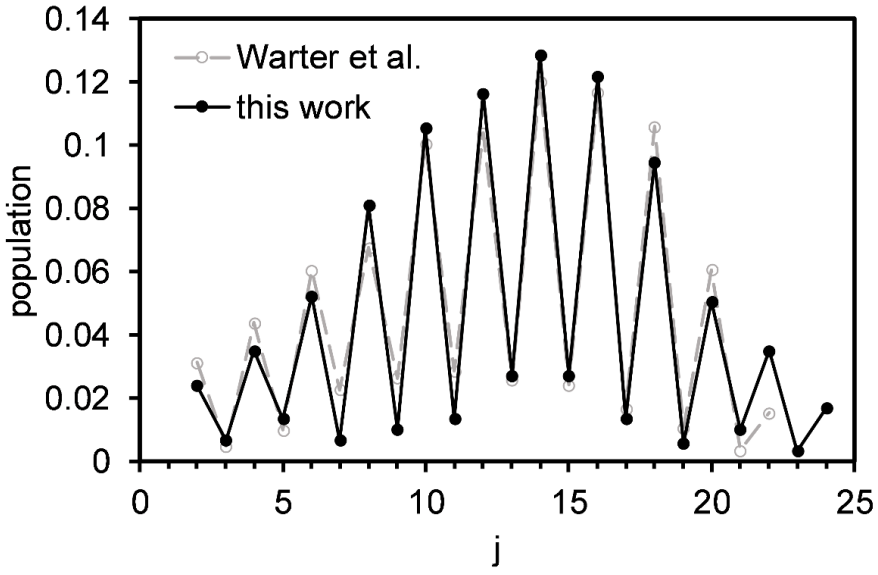


Figure 3.30. Rotational state distributions of the $O_2(a^1\Delta_g, v=0)$ fragments resulting from the 282 nm photodissociation of ozone at 60 K. Distribution from this work (black, solid circles) is compared to that published in Warter *et al.*[26] (gray, open circles).

### 3.7. Conclusions

The $O_2(a^1\Delta_g, v=0)$ rotational distribution resulting from the 266 nm photodissociation of 60 K ozone was remeasured. Significant improvement to the previously measured distribution was achieved through refined experimental procedures and analysis techniques involving the $O_2(d^1\Pi_g, v=4) \leftarrow \leftarrow O_2(a^1\Delta_g, v=0)$ REMPI spectrum. The spectrum was accurately background and power corrected, and more appropriate lineshapes (Lorentzians with *j*-dependent widths) were used in the forward convolution simulation. The new fitting technique was used to refit the spectra at other photolysis wavelengths reported by Warter *et al.* Despite the noticeable improvement in agreement between the simulated and experimental spectra, the corrections between the new and previous rotational state distributions are modest.

# 4. VECTOR CORRELATIONS

## 4.1. $O_2(a^1\Delta_g)$ Vector Correlations

Multiple studies have investigated the vector correlations of the singlet channel in the Hartley band. In the pioneering work of Suits *et al.*,[59] ion images of the $O_2(a^1\Delta_g)$ fragments resulting from the 248 nm photolysis of ozone were analyzed. The images where characteristic of a prompt dissociation following a parallel transition and indicated a strong **v-j** correlation with **v** preferentially oriented perpendicular to **j**. A Monte Carlo forward convolution process was used to simulate the images, and no attempt was made to quantify the observed vector correlations. A subsequent study by Dylewski *et al.*[15] imaged the $O(^1D)$ cofragment. Images were collected at multiple dissociation wavelengths, and it was found that the **μ-v** correlation increased with increasing wavelength, ranging from 0.55 at 235 nm to 0.95 at 298 nm for dissociations resulting in $O_2(a^1\Delta_g, v=0)$ fragments. Analysis of the $O(^1D)$ images also yielded atomic alignment information, with the majority of $O^1(D)$ fragments formed in the $|m_J|=0$ state, some formed in the $|m_J|=1$ state, and almost none formed in the $|m_J|=2$ state.

Vector correlations can also be obtained by analyzing the Doppler profiles measured using photofragment translational spectroscopy. Fairchild *et al.*,[41] Thelen *et al.*,[18] and Takahashi *et al.*[67] have all used this method to determine the **μ-v** correlation of the dissociation at various photolysis wavelengths. Later studies by Ritchie and coworkers extended this analysis to extract the **μ-v**, **v-j**,

and **μ-j** correlations from the Doppler profiles of $O_2(a^1\Delta_g)$ fragments. An initial study at 270 nm revealed odd/even alternations in both the **v-j** and **μ-j** correlations, with the correlations for the odd rotational states being more depolarized than the correlations for the even states.[27] No such alternation was observed for the **μ-v** correlation, which was observed to increase with wavelength as previously reported. The odd/even alternation of the **v-j** and **μ-j** correlations was found to persist at multiple wavelengths between 265 and 300 nm,[28, 29] but was absent at 248 nm.[29] While multiple theories were proposed, the mechanism behind the alternation in the vector correlations was not established.

Following these studies, Warter used ion imaging of the $O_2(a^1\Delta_g)$ fragments to determine the vector correlations for dissociation at 248, 266, and 282 nm.[65] In agreement with previous results, no odd/even alternation was observed in the **μ-v** correlation at any wavelength measured. Additionally, no odd/even alternation was observed in the **v-j** and **μ-j** correlations at 248, 266, or 282 nm. While the lack of alternation at 248 nm is consistent with previous results, Ritchie and coworkers observed alternation in the vector correlations at both 265[29] and 280 nm.[28] This apparent discrepancy warranted further experimental investigation.

In this work, ion imaging experiments were performed to investigate the temperature-dependent vector correlations of the odd and even $O_2(a^1\Delta_g, v=0)$ fragments resulting from the 266 nm photodissociation of ozone. Vector correlations describe the angles between three vectors: the transition dipole moment of the parent molecule (**μ**), the recoil velocity vector of the detected

fragment (**v**), and the angular momentum vector of the detected fragment (**j**). Vector correlations can provide information about the nature and lifetime of the excited state, as well as the forces and torques involved in the dissociation, including those arising from parent motion. As mentioned in Chapter 2, the linearly polarized photolysis laser will preferentially dissociate molecules which have **μ** aligned parallel to the electric field of the laser. Thus, in dissociations with relatively short excited state lifetimes, **μ** provides orientation in the laboratory frame. If the lifetime of the excited complex is longer than the rotational period of the parent molecule, the memory of **μ** is lost, and there will be no correlations involving **μ**. In the case of the photodissociation of ozone in the Hartley band, the lifetime of the excited parent is much shorter than its rotational period,[53-55] so vector correlations involving **μ** are preserved. While there have been previous studies which investigated the vector correlations in the singlet channel for both the $O(^1D)$ and $O_2(a^1\Delta_g)$ fragments,[15, 27-30, 59-61, 68, 69] this study is the first to quantify the temperature dependence of the vector correlations.

### *4.1.1. Experimental*

Images of the $O_2(a^1\Delta_g, v=0)$ photofragments resulting from the 266 nm photolysis of ozone were collected. The $O_2(a^1\Delta_g)$ fragments of interest were ionized using 2+1 REMPI via the $O_2(d^1\Pi_g, v=2) \leftarrow \leftarrow O_2(a^1\Delta_g, v=0)$ transition. As discussed in Chapter 3, the v=2 level of the $O_2(d^1\Pi_g)$ state is highly perturbed. These perturbations result in highly isolated S and R-branch peaks for $j$=16-20,

making this band particularly suited for an imaging study. Additionally, the increased odd state intensity in this band allows for the collection of images with better signal to noise. The perturbations are not expected to affect the angular distributions of the images. In order to compare vector correlations between even and odd rotational states, images were taken at *j*=18, 19, and 20. A total of six images were taken for each *j* state at three temperatures (70, 115, and 170 K). The six-image set consisted of images taken with three laser polarization geometries (VV, HV, VH) in both the R and S-branches for a single rotational state. The polarization of the photolysis beam was vertical after doubling, and could be changed to horizontal using a double Fresnel rhomb. The polarization of the probe beam was horizontal after doubling and could be rotated to vertical using a photoelastic modulator. Polarizers were used to ensure complete polarization of both the photolysis and probe beams. Because the beam temperature, and thus the vector correlations, changed from day to day, all images used in the analysis for a given temperature were taken in a single run.

The temperature of the beam was determined using the relative the peak heights of *j*=16-18 in the S-branch of the $O_2(d^1\Pi_g, v=2) \leftarrow \leftarrow O_2(a^1\Delta_g, v=0)$ REMPI spectrum. As mentioned in Chapter 3, perturbations in this spectrum lead to enhanced odd state populations which makes this region of the spectrum particularly sensitive to parent ozone temperature. In previous studies, this region of the (2,0) spectrum has been measured at four different temperatures, 60 K,[26] 140 K,[60] 200 K,[26] and 300 K.[63] The beam temperatures of the 60 K, 140 K, and

200 K data points were determined using NO calibration. As discussed in Chapter 3, the room temperature experiment was one-color and thus had a photolysis wavelength near the threshold for the dissociation. In this case of near-threshold dissociations, the rotational temperature of the product distribution is expected to be similar to the rotational temperature of the parent distribution.[64] As shown in Figure 3.2, the room temperature REMPI spectrum can be reproduced in a forward convolution simulation with rotational populations determined by a 300 K Boltzmann distribution, supporting the assignment of a parent temperature of 300 K. To develop a calibration curve, a suppression factor was calculated at each temperature according to the following equation:

$$S_{17} = \frac{P_{16,18} - P_{17}}{P_{16,18}} \tag{4.1}$$

where $P_{16,18}$ is the average of the j=16 and j=18 peak heights and $P_{17}$is the j=17 peak height. The results are shown in Figure 4.1. When creating the calibration curve, it was assumed that the relationship between $S_{17}$ and temperature is linear, and that there is complete suppression ($S_{17} = 1$) at 0 K. The assumption of complete suppression at 0 K neglects the angular momentum of the O($^1$D) cofragment and thus is not rigorous. We find, however, that the resulting calibration curve provides a reasonable fit to the experimental data. Figure 4.1 shows best fits with and without assuming complete suppression at 0 K for comparison. The difference between the two curves is about 20 degrees at 70 K, 15 degrees at 115 K, and 10 degrees at 170 K.

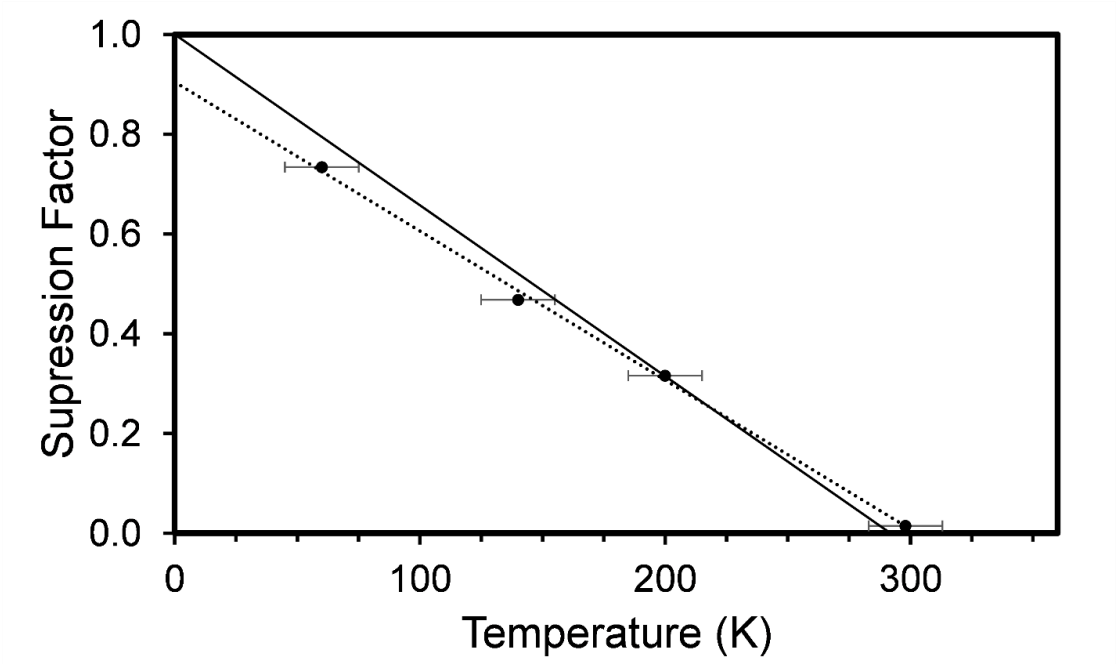


Figure 4.1. Calibration curve used to estimate temperature of molecular beam. Suppression factors shown are for $O_2(a^1\Delta_g, v=0, j=17)$ and were calculated according to equation 4.1. Suppression factors were calculated using REMPI spectra from Warter *et al.*[26] (60 K and 200 K), Hancock *et al.*[60] (140 K) and Morrill *et al.*[63] (300 K). The best fit assuming complete suppression at 0 K is represented by the solid line. The best fit without assuming complete suppression at 0 K is represent by the dotted line.

As confirmation of the beam temperatures calculated using the calibration curve, the radial distribution of the VV $O_2(a^1\Delta_g, v=0, j=20)$ images taken at 70 K, 115 K, and 170 K were analyzed. As can be seen in Figure 4.2, the radial distribution broadens with increasing beam temperature, as expected. In the model, the speed distributions of the $O_2(a^1\Delta_g, v=0, j=20)$ fragments at each parent temperature were calculated using conservation of energy (see Chapter 2). A Gaussian convolution was performed on each resulting distribution to account for parent velocity spread in the imaging plane. To accurately fit the measured speed

distributions, the Gaussians used in the convolution were colder than the estimated parent temperature. This can be explained by the exclusion of high-velocity parent molecules due to the molecular skimmer. The blurring Gaussians had σ values between 20 and 35 m/s. The agreement between the model and experimental data is excellent. Additionally, the measured depolarization of the **μv** correlation is consistent with the reported temperatures (vide infra).

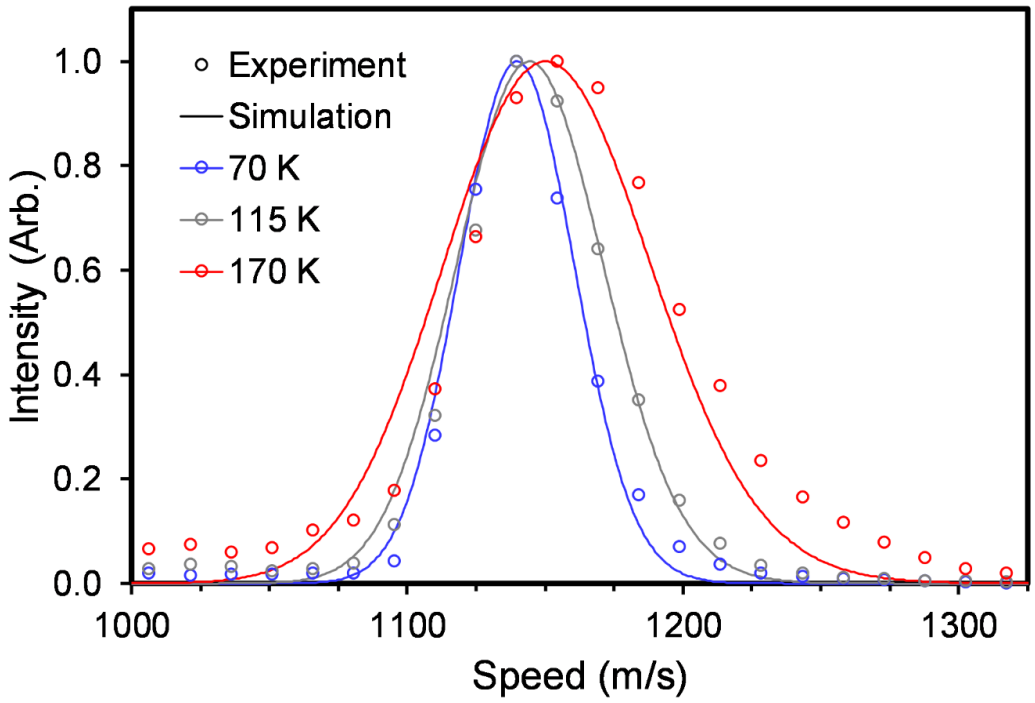


Figure 4.2. Experimental (open circles) and simulated (solid lines) speed distributions for $O_2(a^1\Delta_g$, v=0, *j*=20) at 70 K (blue), 115 K (gray) and 170 K (red). Figure reprinted from Gunthardt *et al. J. Chem. Phys.* **151**, 224302 (2019), with the permission of AIP Publishing.

### *4.1.2. Image Analysis*

Vector correlations were determined by analyzing the image angular distributions. The observed angular distribution is a function of the vector correlations of the photodissociation, the polarizations of the photolysis and probe beams respective to the imaging plane, the number of photons in the photolysis and probe steps, and the rotational branch probed. Because the angular distribution is dependent on all of these factors, additional information is obtained by taking images of the same rovibronic state with different laser polarization geometries in different rotational branches. The laser polarizations employed were VV, HV, VH, and HH where the first letter represents the polarization of the photolysis laser, and the second letter represents to polarization of the probe laser. In this notation, V stands for vertical polarization (parallel to the imaging plane), and H stands for horizontal polarization (perpendicular to the imaging plane). The image angular distributions for VH, HV, and VV polarizations can be described by the following weighted sums of Legendre Polynomials:[70]

$$I^{VH}(\theta) = 1 + \beta_2^{VH} P_2(cos\theta) \tag{4.2}$$

$$I^{HV}(\theta) = 1 + \beta_2^{HV} P_2(cos\theta) + \beta_4^{HV} P_4(cos\theta) \tag{4.3}$$

$$I^{VV}(\theta) = 1 + \beta_2^{VV} P_2(cos\theta) + \beta_4^{VV} P_4(cos\theta) + \beta_6^{VV} P_6(cos\theta) \tag{4.4}$$

As can be seen in equations 4.2-4.4 each vertical photon can add a factor of $\cos^2\theta$ to the angular distribution. The angular distribution of the HH image will always be completely isotropic and thus does not contain any information about vector correlations. If the HH image shows anisotropy at least one of the lasers is not

completely polarized in the H direction, so an HH image was often collected to verify complete laser polarization (see Figure 4.3).

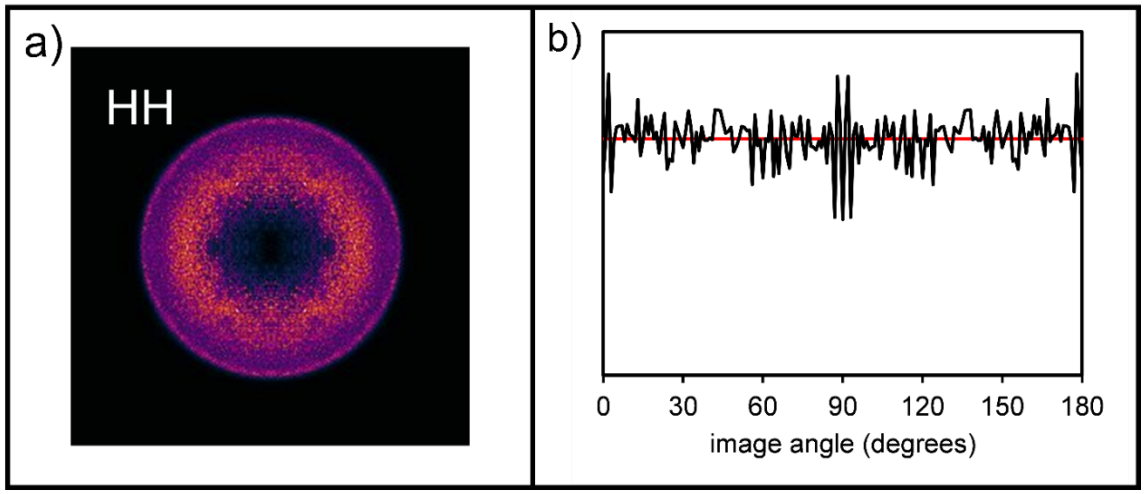


Figure 4.3. a) Image of $O_2(a^1\Delta_g$, v=0, $j$=20) taken in the S-branch with HH laser polarization geometry at 115 K b) Angular distribution of image in panel a. The red line is a guide to the eye. The angular distribution is isotropic, indicating complete polarization of both lasers.

Vector correlations can be described using a semiclassical bipolar moment formalism defined by Dixon.[71] When probing with a 2+1 REMPI scheme, the vector correlations are described by 9 bipolar moments. This work will be focus on the three lower order bipolar moments, $\beta_0^2(20)$, $\beta_0^2(02)$, and $\beta_0^0(22)$. In the semiclassical picture, these lower order bipolar moments represent the expectation values of the second Legendre polynomial $\langle P_2(cos\varphi)\rangle$, where $\varphi$ represents the angle between the **μ** and **v**, **μ** and **j**, and **v** and **j** vectors, respectively. A limiting value of -0.5 indicates the two vectors are aligned

perpendicular, while a limiting value of 1 indicates that the two vectors are aligned parallel. Wei *et al.* have developed a set of equations for use with images taken using a 2+1 REMPI scheme that connect the $\beta^{FG}$ weighting factors from equations 4.2-4.4 to the nine relevant bipolar moments (see Appendix B),[70] based on the approach of Grubb *et al.* for a 1+1 REMPI scheme.[58]

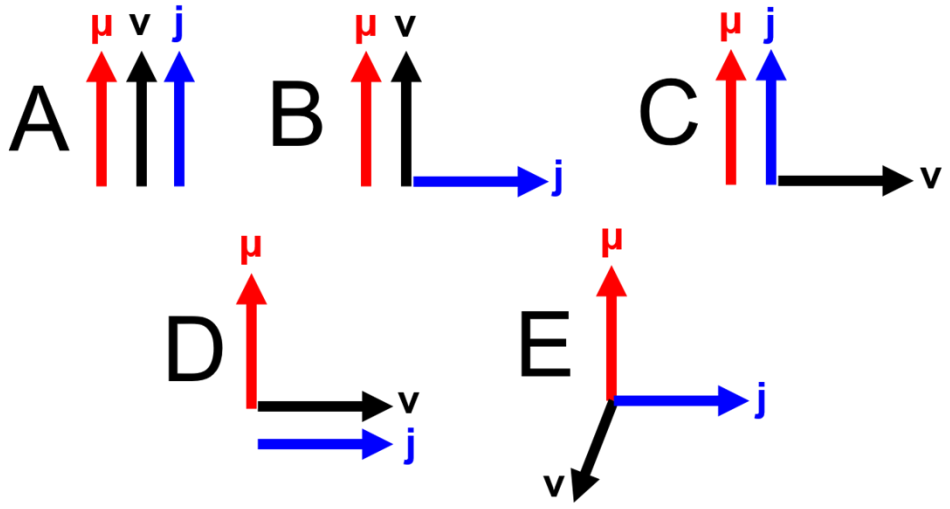


Figure 4.4. Five limiting cases developed by Dixon.[71]

To extract the vector correlations from the measured angular distributions, the forward convolution simulation method described by Wei *et al.* was utilized.[70] In order to restrict the results to physically meaningful combinations of bipolar moments, the Monte Carlo forward convolution fitting process employed the five limiting cases developed by Dixon[71] and depicted in Figure 4.4. Briefly, a random

number generator is used to generate the relative contributions from cases A-E. Each limiting case has a corresponding set of bipolar moments as listed in Table 4.1. The values for the individual bipolar moments (with the exception of $\beta_0^0(44)$) were determined by taking a linear combination of the limiting case values, according to the randomized weightings. Unlike the other bipolar moments, the full range of the $\beta_0^0(44)$ moment cannot be generated from linear combinations of the limiting case values. Because of this, the $\beta_0^0(44)$ moment was independently determined using a random number generator. The resulting bipolar moments were used to calculate a simulated angular distribution, which was compared to experiment through the calculation of a $\chi^2$ value. A $\chi^2$ threshold was set for each angular distribution, and if the $\chi^2$ criterion was met for all distributions, the fit was considered acceptable and the bipolar moment set was saved. A histogram of acceptable values was compiled for each lower order bipolar moment. The resulting histograms were fit with Gaussian functions, and the center line of the Gaussian was taken to be the best fit value of the given bipolar moment, with error bars determined by 2σ. It should be noted that when this work was published the best fit values reported were based on hand fit results, so the values reported in this thesis vary slightly from those reported in Gunthardt *et al.*[72] In most cases, the best fit values derived using both methods agree within mutual error bounds.

Table 4.1. Bipolar moments corresponding to the five limiting cases.[71, 73]

| Bipolar Moment | Case A | Case B | Case C | Case D | Case E |
|---|---|---|---|---|---|
| $\boldsymbol{\beta_0^2(20)}$ | 1 | 1 | -0.5 | -0.5 | -0.5 |
| $\boldsymbol{\beta_0^2(02)}$ | 1 | -0.5 | 1 | -0.5 | -0.5 |
| $\boldsymbol{\beta_0^0(22)}$ | 1 | -0.5 | -0.5 | 1 | -0.5 |
| $\boldsymbol{\beta_0^2(22)}$ | -1 | 0.5 | 0.5 | 0.5 | -1 |
| $\boldsymbol{\beta_0^2(42)}$ | 1 | -0.5 | 0.375 | -0.5 | 0.125 |
| $\boldsymbol{\beta_0^0(44)}$ | 1 | 0.375 | 0.375 | 1 | 0.375 |
| $\boldsymbol{\beta_0^2(24)}$ | 1 | 0.375 | -0.5 | -0.5 | 0.125 |
| $\boldsymbol{\beta_0^2(44)}$ | -1 | -0.375 | -0.375 | 0.5 | 0.75 |
| $\boldsymbol{\beta_0^2(64)}$ | 1 | 0.375 | -0.3125 | -0.5 | -0.0625 |

### *4.1.3. Results*

Six images (S and R-branches; VV, HV, and VH polarizations) were measured for each $O_2(a^1\Delta_g$, v=0, $j$=18, 19, 20) state at 70 K, 115 K, and 170 K. The images and angular distributions for $j$=20 at 70 K and $j$=19 at 170 K are shown in Figures 4.5-4.6 and 4.7-4.8, respectively. The angular distributions of the images change with detection branch and laser polarization geometry, indicating the presence of vector correlations. Comparing the images taken at 70 K (Figure 4.5) and 115 K (Figure 4.7) it can be seen that the signal broadens with increased temperature. Additionally, clear differences can be seen in the R-branch VV and

HV images between $j$=20 (Figure 4.5) and $j$=19 (Figure 4.7) signifying a difference in vector correlations of even and odd rotational states. In the forward convolution simulations, the major contribution was from case B, with significant contributions from cases A and E and minor contributions from cases C and D.

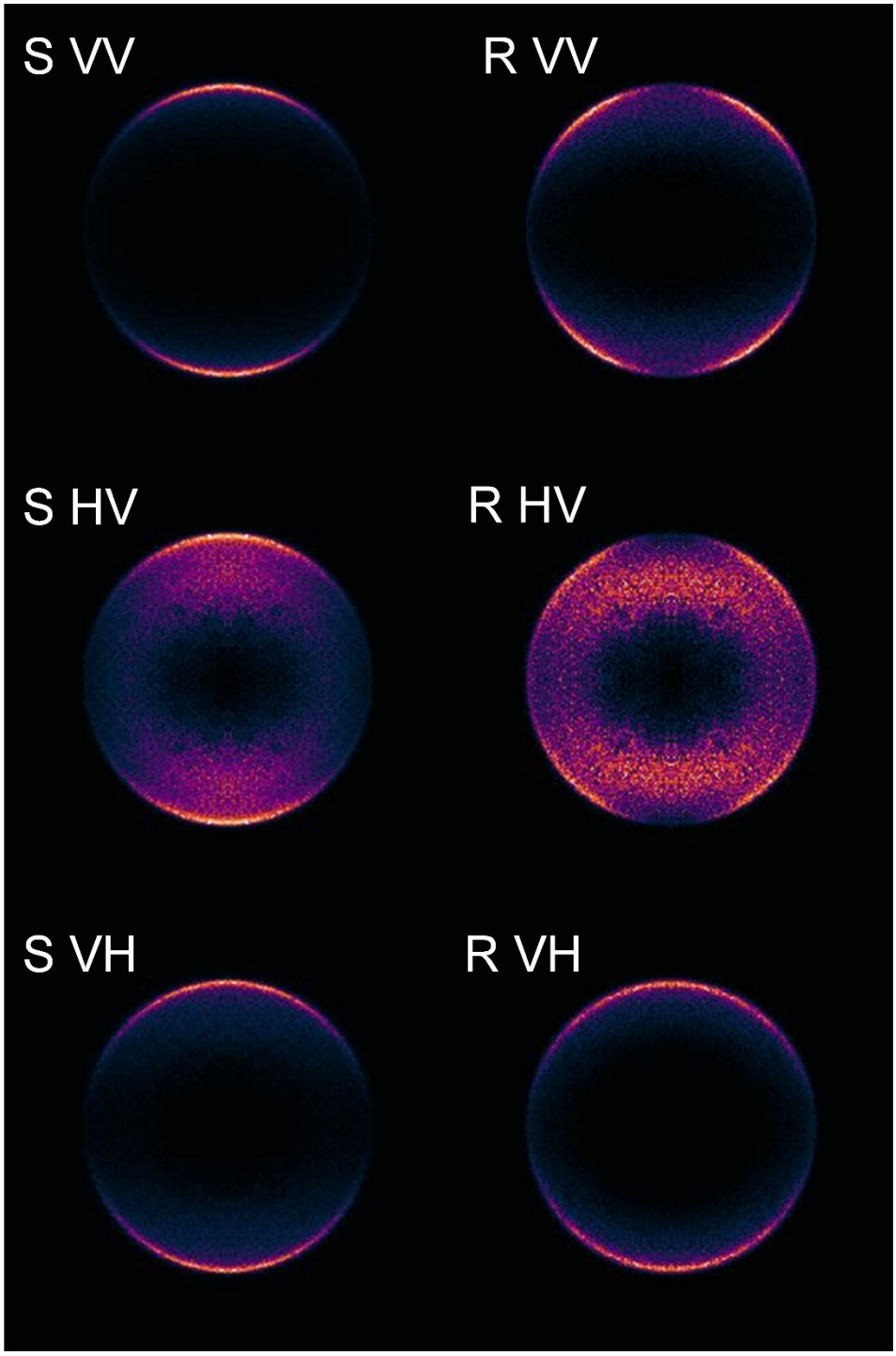


Figure 4.5. Images of $O_2(a^1\Delta_g, v=0, j=20)$ taken at 70 K. The images in the left panel were taken in the S-branch and the images in the right panel were taken in the R-branch. Three laser polarization geometries were used in each branch, as indicated on the figure.

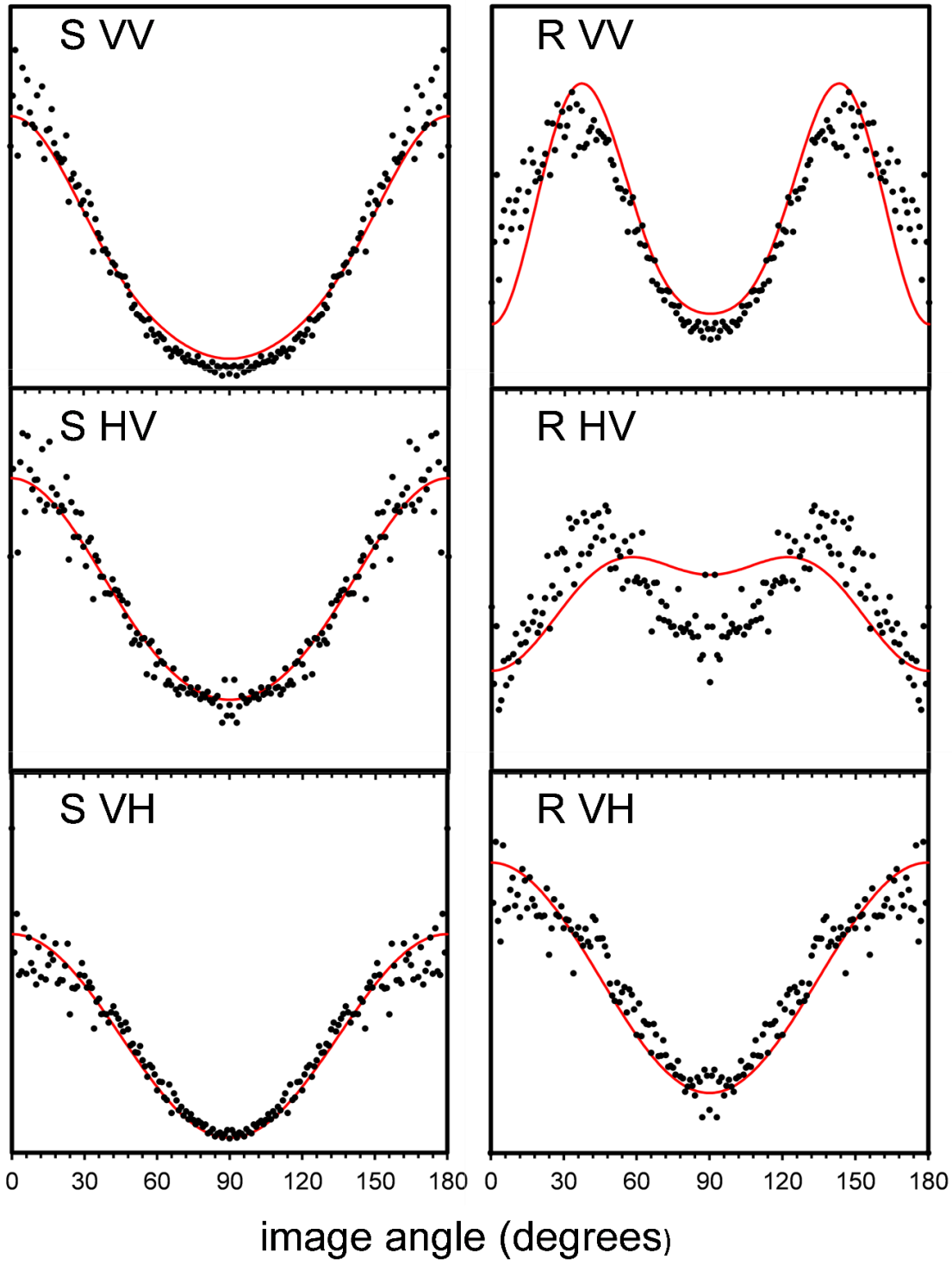


Figure 4.6. Experimental (closed circles) and simulated (solid line) angular distributions for $O_2(a^1\Delta_g, v=0, j=20)$ at 70 K. The experimental angular distributions were extracted from the images shown in Figure 4.5. The bipolar moments used in the forward convolution simulation were determined through Monte Carlo analysis.

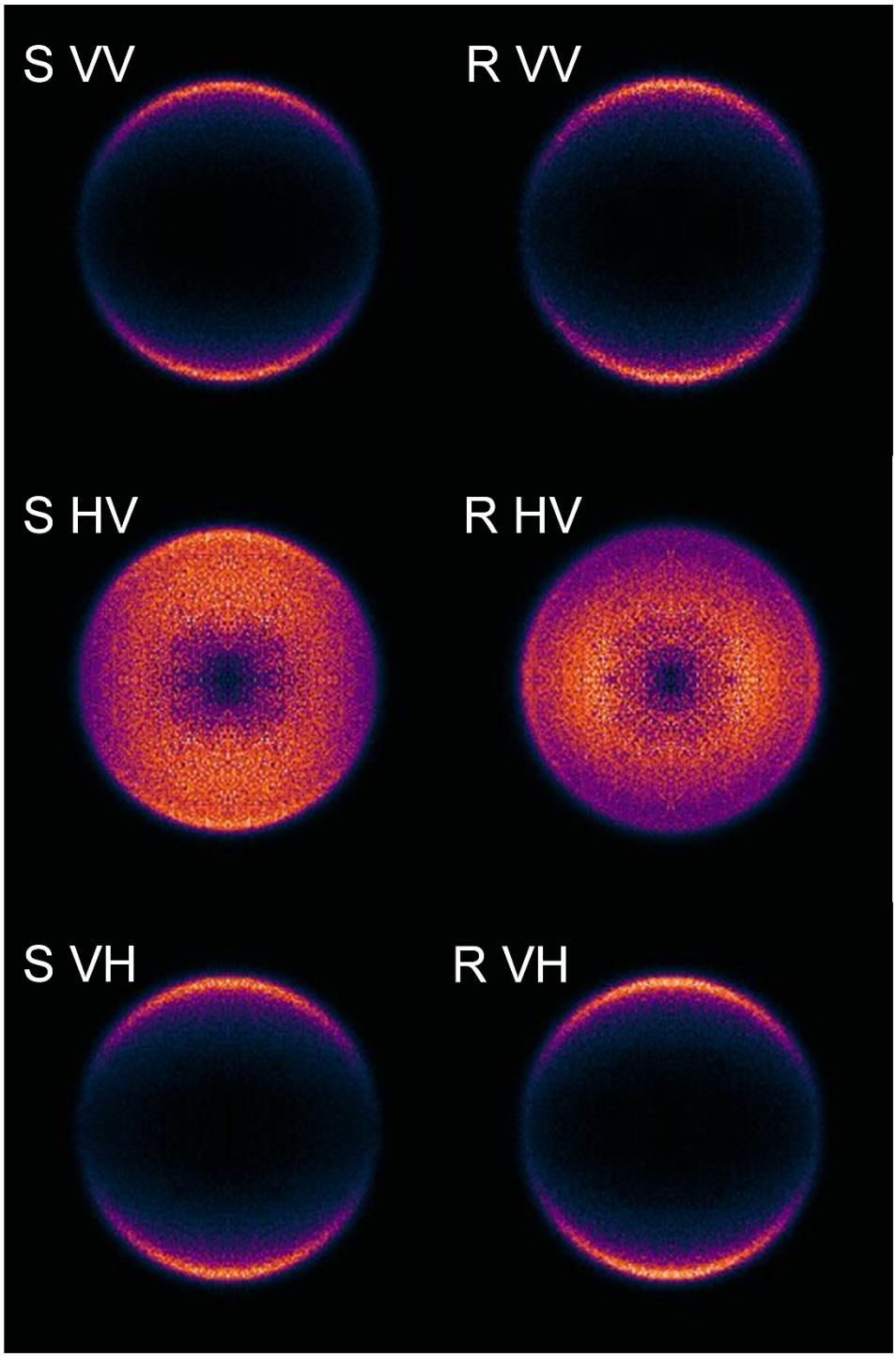


Figure 4.7. Images of $O_2(a^1\Delta_g, v=0, j=19)$ taken at 170 K. The images in the left panel were taken in the S-branch and the images in the right panel were taken in the R-branch. Three laser polarization geometries were used in each branch, as indicated on the figure.

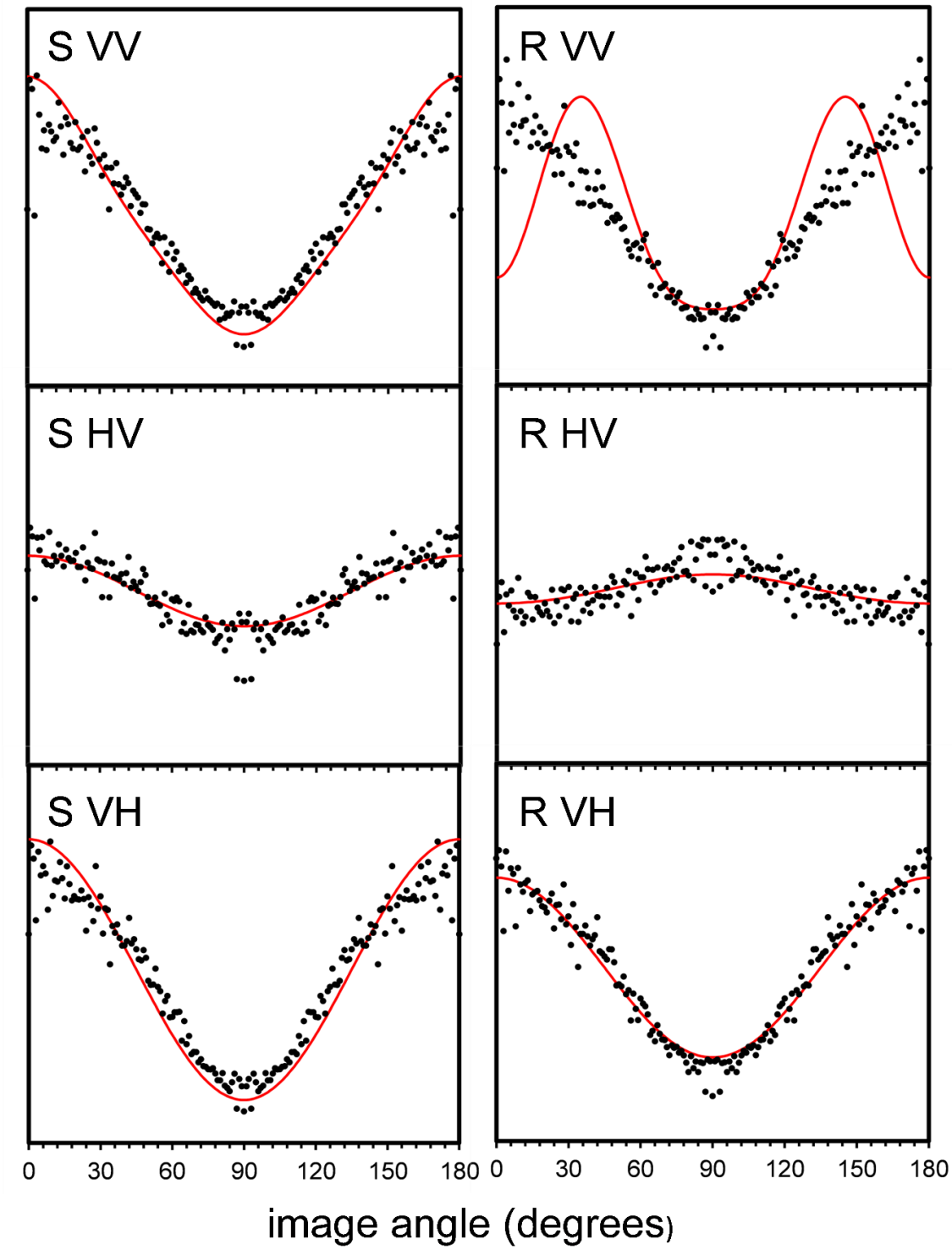


Figure 4.8. Experimental (closed circles) and simulated (solid line) angular distributions for $O_2(a^1\Delta_g, v=0, j=19)$ at 170 K. The experimental angular distributions were extracted from the images shown in Figure 4.7. The bipolar moments used in the forward convolution simulation were determined through Monte Carlo analysis.

The corresponding $\beta_0^2(20)$ (**μ-v**) values are given in Table 4.2. All values are positive and relatively close to the limiting value of 1, indicating a prompt, parallel dissociation, consistent with previous results.[15] A slight temperature dependence is observed, with the **μ-v** correlation decreasing slightly with increasing temperature. The decrease in **μ-v** correlation with increasing temperature is well established and can be explained by increased tangential velocity as well as parent excited state lifetime effects associated with increased parent rotation. The treatment of Busch and Wilson[74] was used to model the temperature dependent depolarization. In this treatment the measured $\beta_0^2(20)$ value can be described by the following equation:

$$b = \left[\frac{P_2(a) + \psi^2 - 3\psi \sin(a) \cos(a)}{1 + 4\,\psi^2}\right] P_2(\beta_0) \qquad (4.5)$$

where $a$ is the deflection angle due to tangential velocity, $\psi$ is the angle the parent molecule rotates through during the average excited state lifetime, and $\beta_0$ is the intrinsic angle between the **μ** and **v** vectors. A $\beta_0^2(20)$ value of 0.75 was used as the intrinsic **μ-v** correlation corresponding to measurements in a jet-cooled molecular beam by Dylewski *et al.*,[15] and the parent lifetime was estimated to be 50 fs. The calculated values, also shown in Table 4.2, are in good agreement with experimental measurements. As reported previously, no significant difference was found for $\beta_0^2(20)$ values between even and odd rotational states of $O_2(a^1\Delta_g)$.[27-29]

Table 4.2. $\beta_0^2(20)$ values for $O_2(a^1\Delta_g$, v=0, *j*=18, 19, 20) at 70 K, 115 K, and 170 K. Quoted errors are 2σ.

| $\boldsymbol{\beta_0^2(20)}$ | *j*=18 | *j*=19 | *j*=20 | model |
|---|---|---|---|---|
| 70 K | 0.63 ± 0.02 | 0.76 ± 0.03 | 0.65 ± 0.07 | 0.69 |
| 115 K | 0.61 ± 0.02 | 0.63 ± 0.07 | 0.60 ± 0.13 | 0.66 |
| 170 K | 0.58 ± 0.04 | 0.58 ± 0.03 | 0.54 ± 0.03 | 0.63 |

The $\beta_0^0(22)$ (**v-j**) values are reported in Table 4.3. For dissociation of a nonrotating triatomic parent molecule, conservation of angular momentum dictates that the **v** and ***j*** vectors of the molecular fragment are perpendicular ($\beta_0^0(22)$ value of -0.5). Parent rotation relaxes this constraint and depolarizes the **v-j** correlation. In most cases, the $\beta_0^0(22)$ value was negative, but not limiting, at all temperatures measured, as expected. The value for *j*=19 at 170 K is positive, but is very close to zero (0.01). For a given *j* state, the **v-j** correlation decreases with increasing parent temperature as a result of greater parent rotational excitation. Within a temperature, the **v-j** correlation for *j*=19 was depolarized compared to that of *j*=18 and *j*=20, indicating that the odd-state fragments arise from a more rotationally excited parent population than the even-state fragments. Ritchie and coworkers have previously reported an alternation in the **v-j** correlation for odd and even rotational states at multiple wavelengths.[27-30] This alternation supports the lambda doublet propensity model, in which the production of $O_2(a^1\Delta_g)$ fragments in odd rotational states is facilitated by parent rotation (vide infra).

Table 4.3. $\beta_0^0(22)$ values for $O_2(a^1\Delta_g$, v=0, *j*=18, 19, 20) at 70 K, 115 K, and 170 K. Quoted errors are 2σ.

| $\boldsymbol{\beta_0^0(22)}$ | *j*=18 | *j*=19 | *j*=20 |
|---|---|---|---|
| 70 K | -0.32 ± 0.08 | -0.22 ± 0.07 | -0.33 ± 0.09 |
| 115 K | -0.14 ± 0.08 | -0.07 ± 0.16 | -0.23 ± 0.20 |
| 170 K | -0.10 ± 0.09 | 0.01 ± 0.06 | -0.14 ± 0.06 |

The measured $\beta_0^2(02)$ (**μ-j**) values are shown in Table 4.4. The **μ-j** values show the same trends as the **v-j** values. This is expected because of the near parallel relationship between the **v** and **μ** vectors. Alternation in the $\beta_0^2(02)$ bipolar moment has also been previously reported by Ritchie and coworkers .[27-30]

Table 4.4. $\beta_0^2(02)$ values for $O_2(a^1\Delta_g$, v=0, *j*=18, 19, 20) at 70 K, 115 K, and 170 K. Quoted errors are 2σ.

| $\boldsymbol{\beta_0^2(02)}$ | *j*=18 | *j*=19 | *j*=20 |
|---|---|---|---|
| 70 K | -0.34 ± 0.08 | -0.25 ± 0.08 | -0.33 ± 0.06 |
| 115 K | -0.20 ± 0.06 | -0.09 ± 0.20 | -0.29 ± 0.22 |
| 170 K | -0.14 ± 0.15 | 0.07 ± 0.09 | -0.13 ± 0.01 |

The differences in vector correlations between odd and even rotational states is most dramatically manifested in the VV and HV R-branch images. As demonstrated in Figure 4.9, the *j*=18 and 20 images show additional nodal

structure at 0° and 180° that is not present in the *j*=19 image. The observed differences in vector correlations and image shape would not be expected if the odd/even rotational state population alternation was a result of parity dependent curve crossing, as previously suggested. Instead, the results suggest differences in the formation of fragments in odd versus even rotational states, as discussed in the following Chapter.

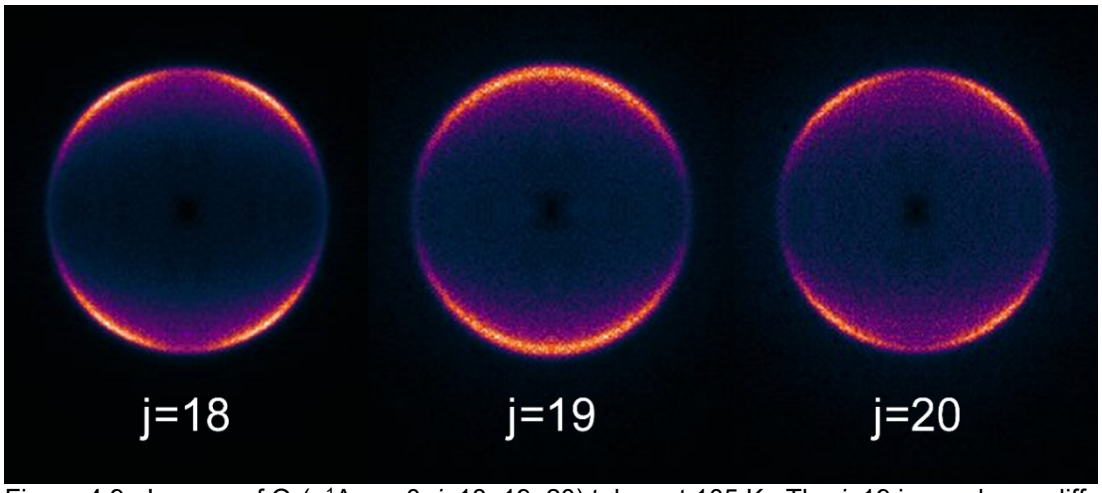


Figure 4.9. Images of $O_2(a^1\Delta_g$, v=0, *j*=18, 19, 20) taken at 105 K. The *j*=19 image has a different angular distribution than the *j*=18 and 20 images, indicating differences in the vector correlations between even and odd rotational states. Figure reprinted from Gunthardt *et al. J. Chem. Phys.* **151**, 224302 (2019), with the permission of AIP Publishing.

### 4.2. Monte Carlo Analysis using Image Subsets

One key factor that allowed for the ability to discern differences in the vector correlations between odd and even images was the use of six images in the fitting process versus the conventional three images with different photolysis and probe

laser geometries (VV, HV, VH) in a single rotational branch. This study employed two rotational branches, the S- and R-branches, taking three images with different laser polarization geometries in each branch. In the imaging studies by Warter, vector correlations were determined using three images taken in either the S-branch or the P-branch.[65] (In the high-*j* limit, angular distributions for images taken in the P and R-branches are equivalent. The same holds true for the O and S-branches). Using this method, Warter was unable to measure differences in vector correlations for the odd and even rotational states.

The use of six images versus three provides an additional six constraints on the results and narrows the experimental error bars. To illustrate this fact, for the 170 K data, Monte Carlo simulations were run with only the S-branch images and with only the R-branch images, using the same chi2 criterion as in the six image simulations. To compare to a one-color experiment where VV is the only possible laser geometry, such as imaging of the CO($X^1\Sigma^+$) fragments following 215 nm photodissociation of OCS,[70, 75, 76] simulations were also run using only the S- and R-branch VV images. The results for the lower order bipolar moments are shown in Figure 4.10 and Tables 4.5-4.7 below.

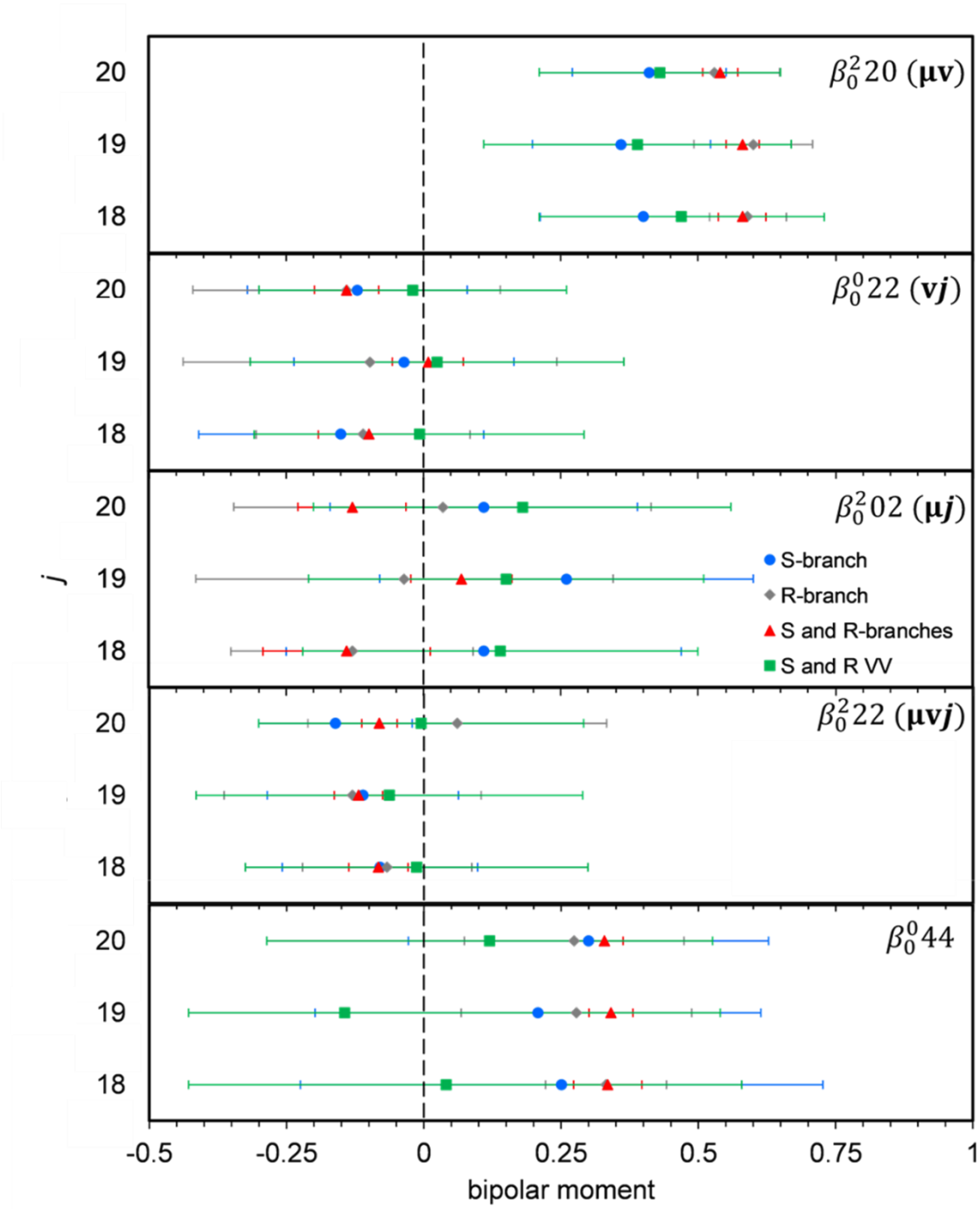


Figure 4.10. Lower order bipolar moments, $\beta_0^2(22)$, and $\beta_0^0(44)$ for $O_2$($a^1\Delta_g$, v=0, $j$=18, 19, 20) at 170 K as determined through Monte Carlo forward convolution simulations using different image sets. Error bars represent 2σ.

It can be seen from the figure that the use of six images, three from the S-branch and three from the R-branch, results in the smallest error bars. In most cases, the largest error bars result from using the S and R-branch VV subset of images. It should be noted that the R-branch VV image showed the largest deviation from the forward convolution simulation in all experimental data sets, so this may be the cause of the large error bars for the S and R VV image subset. This does not hold true for the synthetic data sets discussed below (Figures 4.11 and 4.13), suggesting an issue with either the R-branch VV experimental images or equations. Along with the six-image case, both the S-branch only and the S and R-branch VV image subsets were able to capture the odd/even alternation in the **v-j** correlation. Additionally, the S-branch only subset was also able to capture the odd/even alternation in the **μ-j** correlation that was observed in the six-image case. It was surprising that the R-branch only image subset was not able to reproduce these trends, given the R-branch images showed the greatest differences between even and odd rotational states (see Figures 4.5, 4.7, and 4.9). Based on the large error bars associated with the three image subset results, it is understandable that Warter did not observe any clear alternation in her imaging experiments.[65]

Table 4.5. Low order bipolar moments and $\beta_0^2(22)$ and $\beta_0^0(44)$ for $O_2(a^1\Delta_g$, v=0, *j*=18) as determined by Monte Carlo analysis using different image sets. Quoted errors are 2σ.

| *j*=18 | R only | S only | S and R VV only | S and R all images |
|---|---|---|---|---|
| $\beta_0^2(20)$ | 0.59 ± 0.07 | 0.40 ± 0.19 | 0.47 ± 0.26 | 0.58 ± 0.04 |
| $\beta_0^0(22)$ | -0.11 ± 0.19 | -0.15 ± 0.26 | -0.01 ± 0.30 | -0.10 ± 0.09 |
| $\beta_0^2(02)$ | -0.13 ± 0.22 | 0.11 ± 0.36 | 0.14 ± 0.36 | -0.14 ± 0.15 |
| $\beta_0^2(22)$ | -0.07 ± 0.15 | -0.11 ± 0.17 | -0.01 ± 0.31 | -0.08 ± 0.05 |
| $\beta_0^0(44)$ | 0.33 ± 0.11 | 0.25 ± 0.48 | 0.04 ± 0.54 | 0.34 ± 0.06 |

Table 4.6. Low order bipolar moments and $\beta_0^2(22)$ and $\beta_0^0(44)$ for $O_2(a^1\Delta_g$, v=0, *j*=19) as determined by Monte Carlo analysis using different image sets. Quoted errors are 2σ.

| *j*=19 | R only | S only | S and R VV only | S and R all images |
|---|---|---|---|---|
| $\beta$02(20) | 0.60 ± 0.11 | 0.36 ± 0.16 | 0.39 ± 0.28 | 0.58 ± 0.03 |
| $\beta_0^0(22)$ | -0.10 ± 0.34 | -0.04 ± 0.20 | 0.03 ± 0.34 | 0.01 ± 0.06 |
| $\beta_0^2(02)$ | -0.04 ± 0.38 | 0.26 ± 0.34 | 0.15 ± 0.36 | 0.07 ± 0.09 |
| $\beta_0^2(22)$ | -0.13 ± 0.23 | -0.11 ± 0.17 | -0.06 ± 0.35 | -0.12 ± 0.04 |
| $\beta_0^0(44)$ | 0.28 ± 0.21 | 0.21 ± 0.41 | -0.14 ± 0.68 | 0.34 ± 0.04 |

Table 4.7. Low order bipolar moments and $\beta_0^2(22)$ and $\beta_0^0(44)$ for $O_2(a^1\Delta_g$, v=0, *j*=20) as determined by Monte Carlo analysis using different image sets. Quoted errors are 2σ.

| *j*=20 | R only | S only | S and R VV only | S and R all images |
|---|---|---|---|---|
| $\beta_0^2(20)$ | 0.53 ± 0.12 | 0.41 ± -0.14 | 0.43 ± 0.22 | 0.54 ± 0.03 |
| $\beta_0^0(22)$ | -0.14 ± 0.28 | -0.12 ± 0.20 | -0.02 ± 0.28 | -0.14 ± 0.06 |
| $\beta_0^2(02)$ | 0.04 ± 0.38 | 0.11 ± 0.28 | 0.18 ± 0.38 | -0.13 ± 0.01 |
| $\beta_0^2(22)$ | 0.06 ± 0.27 | -0.16 ± 0.14 | 0.00 ± 0.30 | -0.08 ± 0.03 |
| $\beta_0^0(44)$ | 0.27 ± 0.20 | 0.30 ± 0.33 | 0.12 ± 0.41 | 0.33 ± 0.03 |

To verify the above results were not simply a result of experimental artifacts, the same analysis was conducted on a set of simulated data. Simulated data also has the advantage that the true values of the bipolar moments are known. The simulated data set was generated to be similar to the experimental even rotational state ozone data and is shown in Figure 4.11. The simulated data has the following fractions of limited cases: 0.2 A, 0.51 B, 0.04 C, 0.06 D, and 0.19 E, corresponding to a $\beta_0^2(20)$ value of 0.565, a $\beta_0^2(02)$ value of -0.14 and a $\beta_0^0(22)$ value of -0.11. Intensity-dependent (± 5%) and intensity-independent noise was added to the simulated data using a random number generator. The results for the majority case B synthetic data are shown in Figure 4.12 and Table 4.8 below.

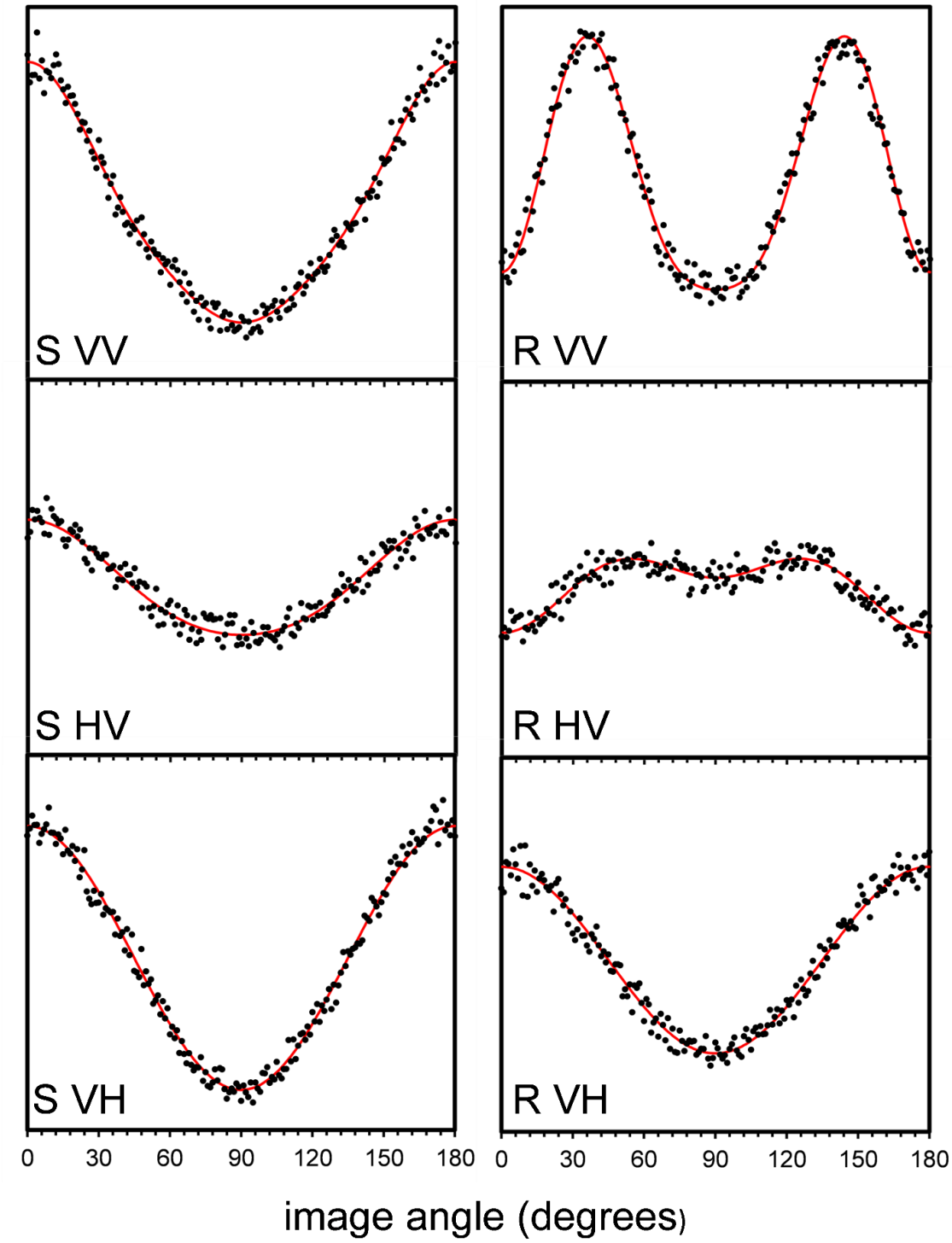


Figure 4.11. Majority case B synthetic data (closed circles) and best fit (red line). The bipolar moments used in the best fit forward convolution simulation were determined through Monte Carlo analysis.

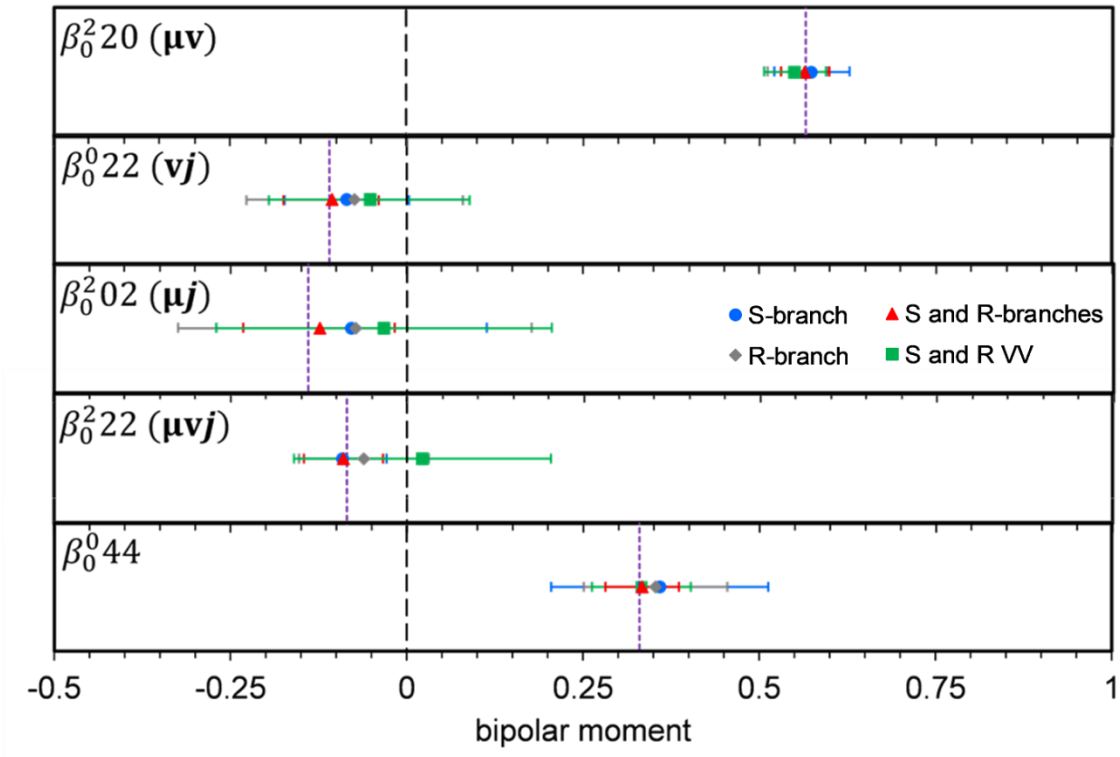


Figure 4.12. Lower order bipolar moments and $\beta_0^2(22)$ and $\beta_0^0(44)$ for the majority case B synthetic data as determined through Monte Carlo forward convolution simulations using different image sets. The true value for each bipolar moment is indicated by the purple dashed line. Error bars represent 2σ.

Table 4.8. Low order bipolar moments and $\beta_0^2(22)$ and $\beta_0^0(44)$for the majority case B synthetic data as determined by Monte Carlo analysis using different image sets. Quoted errors are 2σ.

| | R only | S only | S and R VV only | S and R all images | true value |
|---|---|---|---|---|---|
| $\boldsymbol{\beta_0^2(20)}$ | 0.55 ± 0.04 | 0.57 ± 0.05 | 0.55 ± 0.04 | 0.56 ± 0.03 | 0.565 |
| $\boldsymbol{\beta_0^0(22)}$ | -0.07 ± 0.15 | -0.09 ± 0.09 | -0.05 ± 0.14 | -0.11 ± 0.07 | -0.11 |
| $\boldsymbol{\beta_0^2(02)}$ | -0.07 ± 0.25 | -0.08 ± 0.19 | -0.03 ± 0.24 | -0.13 ± 0.11 | -0.14 |
| $\boldsymbol{\beta_0^2(22)}$ | -0.06 ± 0.09 | -0.09 ± 0.06 | 0.02 ± 0.18 | -0.09 ± 0.06 | -0.085 |
| $\boldsymbol{\beta_0^0(44)}$ | 0.35 ± 0.10 | 0.36 ± 0.15 | 0.33 ± 0.07 | 0.33 ± 0.05 | 0.33 |

While the difference in the relative magnitude of the error bars is less extreme for the synthetic data set than in the experimental data set, the six-image set consistently leads to smaller error bars than the other subsets, as expected. The bipolar moments determined using all six images are also closer to the true value than the values determined using only a subset of images. These results suggest that the advantage of using all six images to determine the bipolar moments goes beyond experimental artifacts.

To test the generality of these results, another set of synthetic data was created, this time with majority contributions from cases C and E and is shown in Figure 4.13. This case corresponds to the dissociation of a triatomic with a perpendicular transition, similar to one of the channels in the UV photodissociation of OCS.[77] The limiting case fractions of this synthetic data set is as follows: 0.06 A, 0.08 B, 0.40 C, 0.02 D, and 0.44 E, corresponding to $\beta_0^2(20)$ of -0.29, $\beta_0^0(22)$ of -0.38, and $\beta_0^2(02)$ of 0.19. The same analysis was performed on the majority case C and E data set, and the results are presented in Figure 4.14 and Table 4.9.

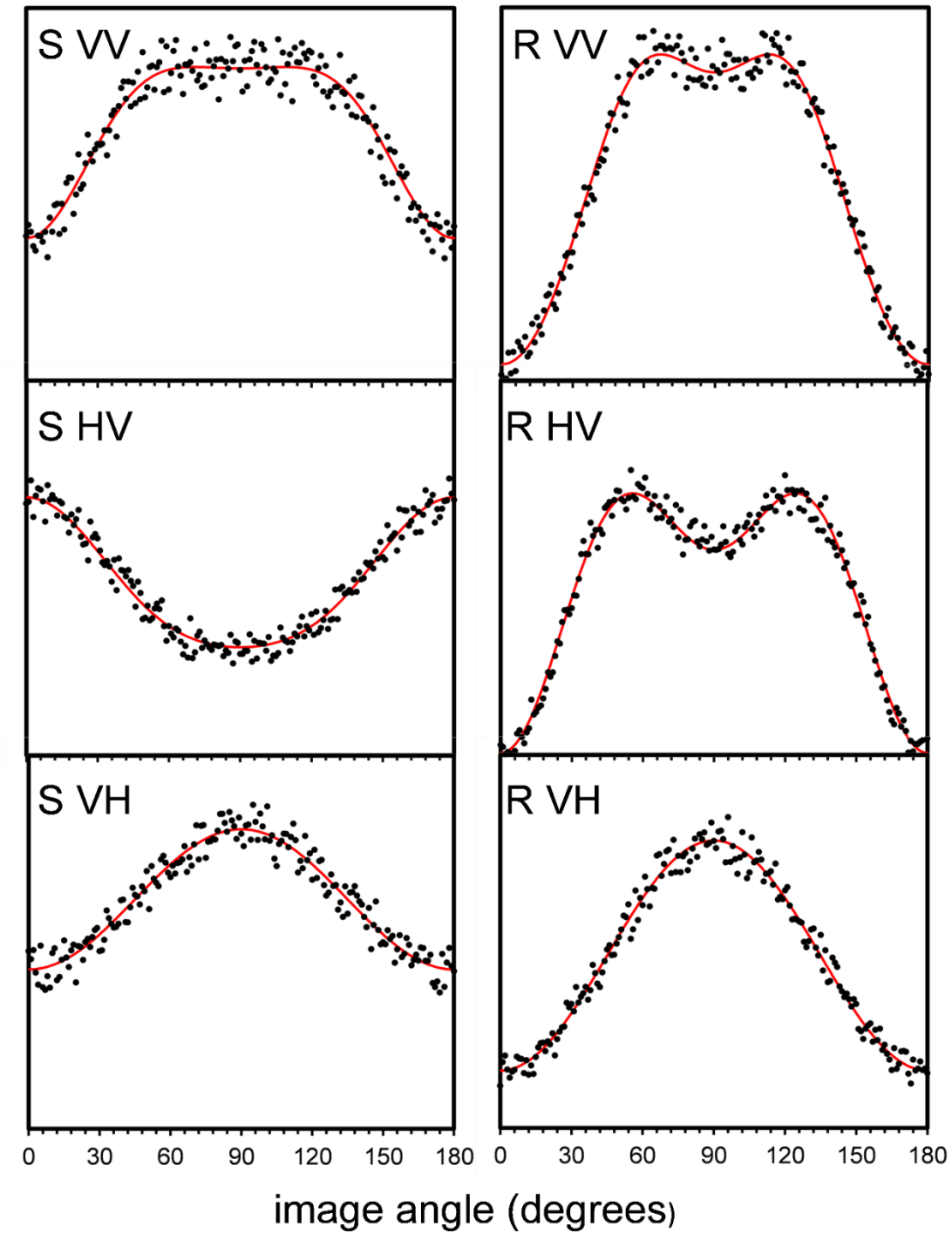


Figure 4.13. Majority cases C and E synthetic data (closed circles) and best fit (red line). The bipolar moments used in the best fit forward convolution simulation were determined through Monte Carlo analysis.

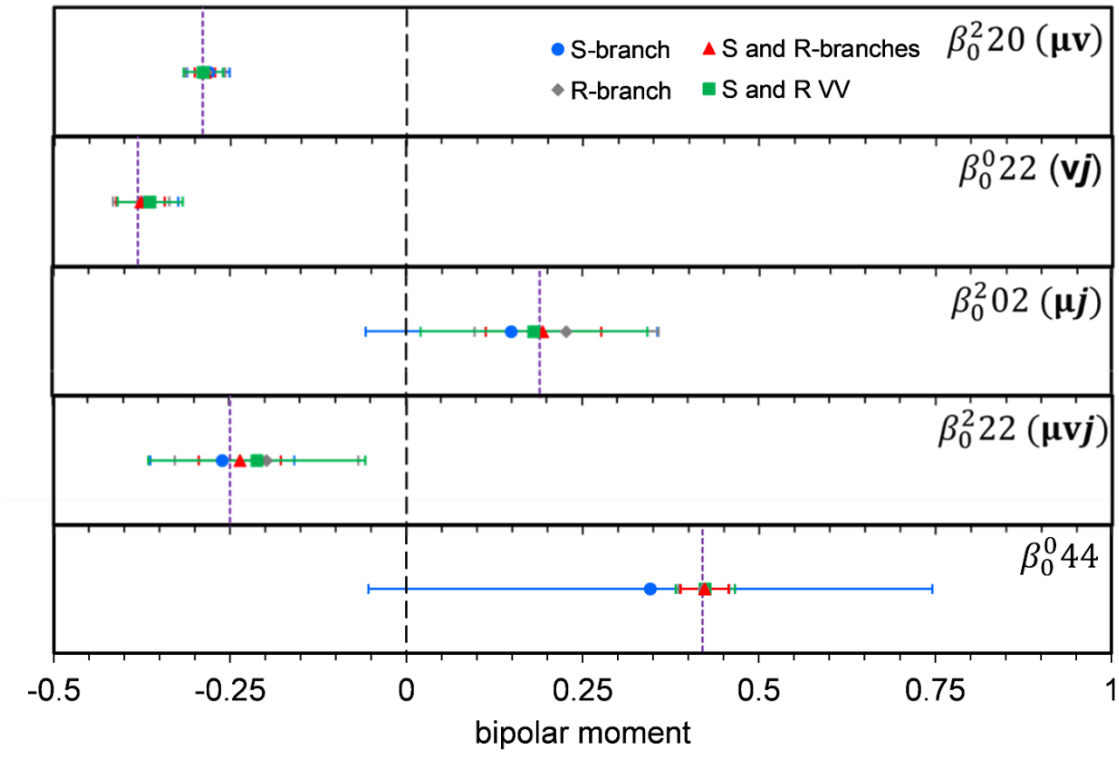


Figure 4.14. Lower order bipolar moments and $\beta_0^2(22)$ and $\beta_0^0(44)$ for the majority cases C and E synthetic data as determined through Monte Carlo forward convolution simulations using different image sets. The true value for each bipolar moment is indicated by the purple dashed line. Error bars represent 2σ.

Table 4.9. Low order bipolar moments and $\beta_0^2(22)$ and $\beta_0^0(44)$ for the majority cases C and E synthetic data as determined by Monte Carlo analysis using different image sets. Quoted errors are 2σ.

| | R only | S only | S and R VV only | S and R all images | true value |
|---|---|---|---|---|---|
| $\boldsymbol{\beta_0^2(20)}$ | -0.29 ± 0.03 | -0.28 ± 0.03 | -0.29 ± 0.03 | -0.29 ± 0.01 | -0.29 |
| $\boldsymbol{\beta_0^0(22)}$ | -0.38 ± 0.04 | -0.37 ± 0.05 | -0.36 ± 0.05 | -0.38 ± 0.03 | -0.38 |
| $\boldsymbol{\beta_0^2(02)}$ | 0.23 ± 0.13 | 0.15 ± 0.21 | 0.18 ± 0.16 | 0.20 ± 0.08 | 0.19 |
| $\boldsymbol{\beta_0^2(22)}$ | -0.20 ± 0.13 | -0.26 ± 0.10 | -0.21 ± 0.15 | -0.24 ± 0.06 | -0.25 |
| $\boldsymbol{\beta_0^0(44)}$ | 0.42 ± 0.04 | 0.34 ± 0.40 | 0.42 ± 0.04 | 0.42 ± 0.03 | 0.42 |

Similar to the other two data sets, the analysis using all six images produced the smallest error bars. The resulting bipolar moments from the six-image analysis are in good agreement with the true value for all three lower order moments, as well as $\beta_0^2(22)$ and $\beta_0^0(44)$. There was a much smaller spread in values among the different image sets for this synthetic data set than for the other two cases.

The fact that analysis using all six images resulted in narrower distributions for the experimental and synthetic cases shows that there is an intrinsic advantage to using six images versus three or two, but whether the advantage goes beyond simply having more constraints is an open question. The relative decrease in the width of the bipolar moment distributions resulting from analysis with six images versus analysis with only a subset of images was much greater for the experimental case than for either of the synthetic cases. Additionally, the spread in values among the image sets was much larger in the experimental case than the synthetic cases. This implies that the advantage gained from using six images in the experimental analysis is largely due to imperfections in the images themselves. The more images simultaneously analyzed, the less each individual artifact will affect the overall result. The differences in the spread in values between the majority B and majority C and E synthetic data sets implies that some combinations of limiting cases are more sensitive to the number of images used in the analysis than others. In many cases it is not possible to collect images in two branches with three polarization geometries. In two-color experiments with two appropriate isolated branches (O or S and P or R), however, it is

recommended that images are collected in two branches with the three laser polarization geometries for a total of six images.

# 5. CLASSICAL MODEL BASED ON Λ-DOUBLET PREFERENCE

The previous Chapters have presented evidence for a preference for the formation of the A′ Λ-doublet of $O_2(a^1\Delta_g)$ following the UV photodissociation of ozone. In Chapter 3 it was demonstrated that the $O_2(a^1\Delta_g)$ rotational distribution has a population alternation favoring the even rotational states. Due to symmetry restrictions, the A′ Λ-doublet can only occupy even rotational states while the A″ Λ-doublet can only occupy odd rotational states, so the population alternation favors the A′ Λ-doublet. The magnitude of the population alternation was shown to be temperature dependent with decreasing alternation with increasing temperature. This temperature dependence is inconsistent with a parity-selective curve crossing model. In Chapter 4 temperature dependent vector correlation measurements were presented for odd and even rotational states. It was found that both the **v-j** and **μ-j** correlations were more depolarized for the odd rotational states than the even rotational states, suggesting the odd rotational states arose from a more rotationally excited parent population. Additionally, for a given *j* state the **μ-v**, **v-j**, and **μ-j**, correlations became more depolarized with increasing temperature. In this Chapter, we present a classical model based on the preference for the formation of the A′ Λ-doublet of $O_2(a^1\Delta_g)$ in the UV photodissociation of ozone that is able to qualitatively reproduce the experimental trends in Chapters 3 and 4.

## 5.1. Classical Model

The model is partially based on the work of Levene and Valentini.[64] Levene and Valentini developed a model to predict the effect of parent rotation on the fragment rotational distribution for the dissociation of triatomic molecules with $C_{2v}$ symmetry. In this model, classical mechanics is used to map the parent rotational and vibrational motion onto the fragment motion using a cartesian coordinate system.

In the original model of Levene and Valentini, the intrinsic angular momentum imparted on the fragment during the dissociation process was estimated using the modified impulsive model. In the modified impulsive model the partitioning between rotational and translational motion is determined by geometric and kinematic factors. According to the model, the energy available for fragment rotation is determined by the following equation:[78]

$$E_{rot} = \frac{m_1 m_2 E_{avl} sin^2\Theta}{(m_1 + m_2)(m_2 + m_3) - m_1 m_3 cos^2\Theta} \tag{5.1}$$

where $m_i$ is the mass of the i$^{th}$ atom, $\Theta$ is the bond angle, and $E_{avl} = h\upsilon - D_0 - E_{elec} - E_{vib}$. The departing atom is atom 3, and the central atom is atom 2. The equilibrium bond angle of 117° was used in the impulsive model calculations, as the dissociation is treated as sudden. The energy partitioned into rotation corresponds to a single rotational level, which can be calculated according to

$$j_{diss} = [(B' + 4E_{rot})/4B']^{1/2} - \frac{1}{2} \tag{5.2}$$

where $B'$ is the rotational constant of the diatomic fragment. For dissociation in the singlet channel, equations 5.1 and 5.2 predict a $j_{diss}$ of 34 for photolysis at 248 nm, 27 for photolysis at 266 nm, and 21 for photolysis at 282 nm. It is now known that fragment angular momentum is due to angular anisotropy, and not impulses from the dissociation.

The triatomic parent is treated as a classical asymmetric top, with energy levels given by the equation

$$E_{rot} = AJ_A^2 + BJ_B^2 + CJ_C^2 \quad (5.3)$$

where A, B, and C are the constants for rotation around the A, B, and C axis, respectively. The three axes are depicted in Figure 5.1. In the case of ozone and other triatomic molecules with $C_{2v}$ symmetry, the C axis is perpendicular to the molecular plane and the B axis is the $C_2$ rotation axis, bisecting the molecular angle. For parent rotation with a given $J_A$, $J_B$, and $J_C$ combination, the linear momentum of each atom is calculated. Rotation in both directions about each axis is considered. The weighting of each $J_A$, $J_B$, and $J_C$ combination is determined using a Boltzmann distribution. The impact of zero-point bending motion on fragment rotation was also accounted for in the model. The $v_2$ vibrational mode was described by a harmonic oscillator wavefunction. The linear momentum imparted on each atom due to vibrational motion is calculated for different phases of the vibration.

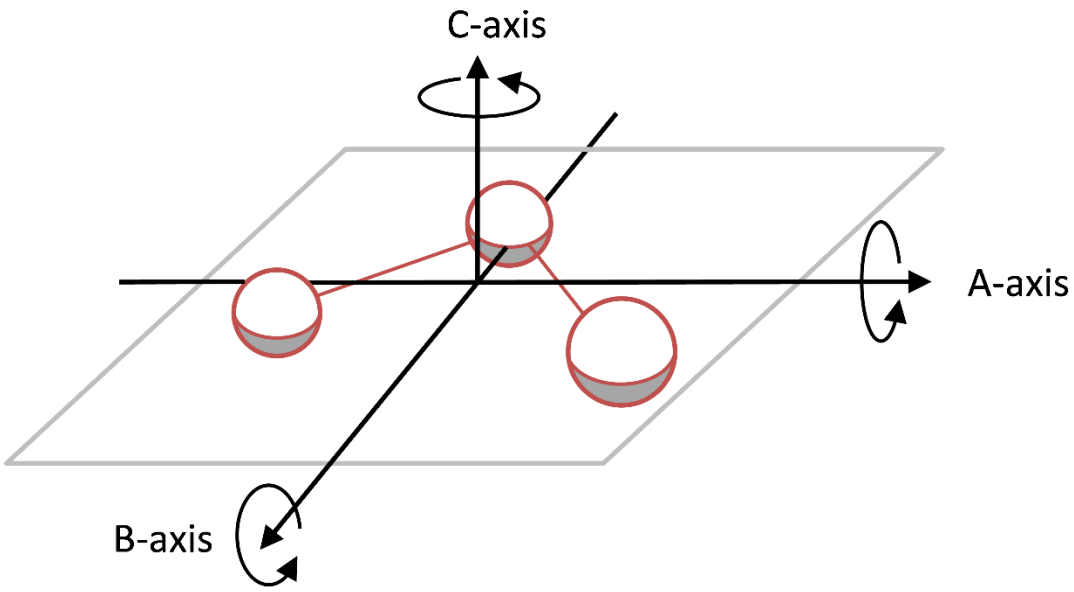

Figure 5.1. Three axes of rotation in ozone.

To determine the rotational motion of the fragment, the cartesian components of linear momentum resulting from an impulsive dissociation, parent rotation, and zero-point vibrational motion were summed. The magnitude of the angular momentum of the fragment was determined using the following equation,

$$j_{O_2} = \left[\left(j_{diss,O_2} + j_{O_2,C}\right)^2 + \left(j_{O_2,A}\right)^2 + \left(j_{O_2,B}\right)^2\right]^{1/2} \quad (5.4)$$

where $j_{O_2,i}$ is the fragment rotational angular momentum arising from parent rotation about the i[th] axis. Conservation of angular momentum dictates that $j_{diss}$ is perpendicular to the molecular plane. Accordingly, rotation about the C axis, which is also perpendicular to the molecular plane, will change the magnitude of $j_{O_2}$ but not its direction. Depending on the direction of rotation, rotation about the C axis can increase or decrease the fragment rotational angular momentum.

Rotation about the A and B axes on the other hand will change both the magnitude and direction of the fragment angular momentum vector. The effect of parent rotation on the fragment rotational distribution can be seen in Figure 5.2. For the calculated distributions shown in this figure, a single $j_{diss}$ of 20 is used. At 1 K, most of the population remains in $j$=20, and there is a small amount of population in $j$=19 and 21 due to parent rotation. As the parent temperature is increased to 10 K, $j$=20 is still the peak of the distribution but no longer holds the majority of the population, and the distribution has broadened to encompass $j$=17-23. At a parent temperature of 100 K, the distribution has continued to broaden and the peak of the distribution has shifted to $j$=21.

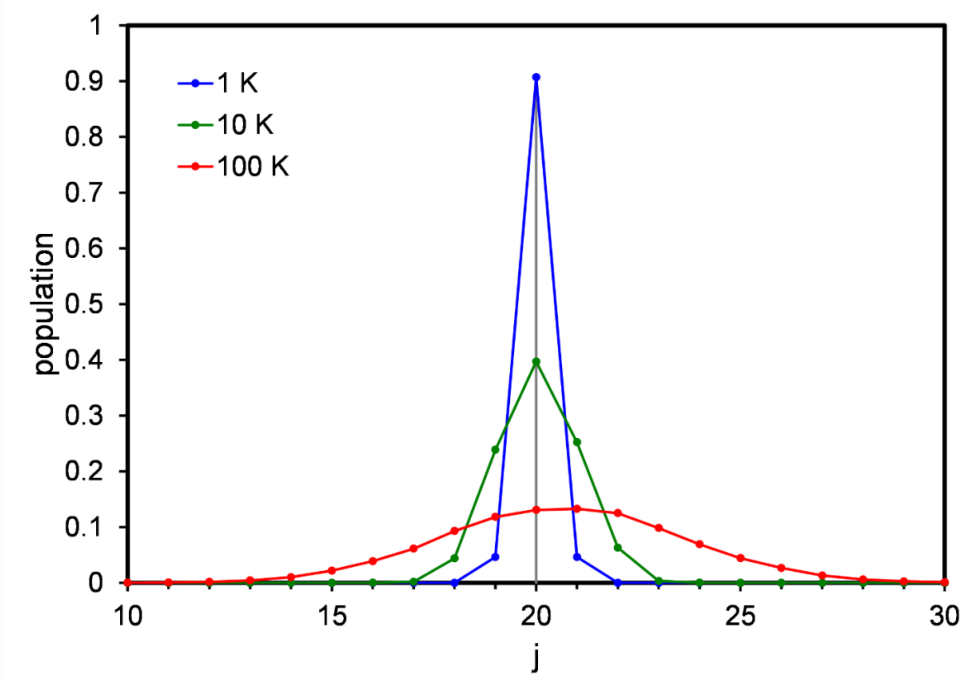


Figure 5.2. Model results starting with a single $j_{diss}$ of 20 at parent temperatures of 1 K (blue), 10 K (green) and 100 K (red). As the parent temperature is increased the rotational distribution broadens and shifts.

In order to verify the code we compare to previous results from Levene and Valentini. Levene and Valentini applied their model to the case of at threshold dissociation of 300 K ozone to form $O_2(\,^3\Sigma_g^-)$ and $O(^1P)$ fragments. It was found that the resulting $O_2(\,^3\Sigma_g^-)$ distribution resembled that of a 300 K Boltzmann, implying that the thermal rotational motion of the parent is transferred effectively into fragment rotation in a near threshold dissociation. They also applied the model to the same dissociation but with 7200 $cm^{-1}$ available energy, corresponding to a $j_{diss}$ of 32 based on the impulsive model (eq 5.1 and 5.2). When zero-point vibrational motion is excluded, the result is a bifurcated rotational

distribution. When zero-point vibrational motion is included to provide a range of initial angles, there is no longer bifurcation. When comparing the model and experimental $O_2(^3\Sigma_g^-)$ distributions, it was found that the calculated distribution was significantly broader than the experimental distribution (FWHM of 16 for the experimental and 21 for the model). Excellent agreement was found between experiment and model if parent rotational combinations with the rotation about the C axis antiparallel to $j_{diss}$ were excluded, leading that authors to propose that the direction of rotation dictates which of the two O-O bonds is broken.

In the model presented by Levene and Valentini the treatment of the degeneracy factor, g, in the parent rotation Boltzmann distribution was incorrect. The results of Levene and Valentini can be reproduced using a degeneracy factor of $g=(2J_A+1)(2J_B+1)(2J_C+1)$. As can be seen in Figure 5.3, treating the degeneracy in this manner leads to a parent distribution that is hotter than the experimental distribution measured by Erlandsson using microwave spectroscopy.[79, 80]

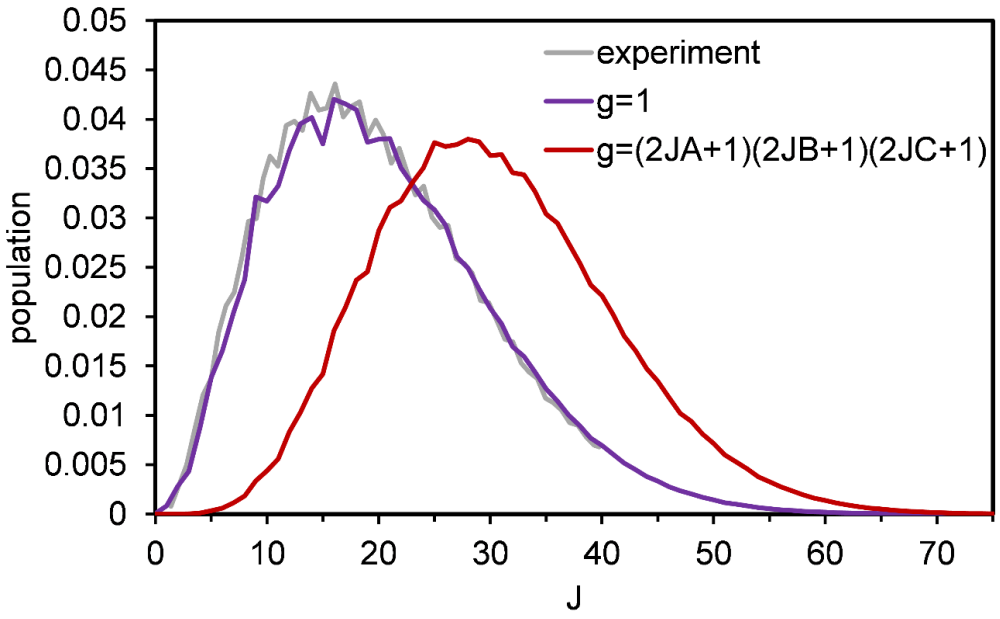


Figure 5.3. Experimental ozone rotational distribution at 300 K[64] compared to 300 K Boltzmann distributions calculated using a degeneracy factor of g=1 and g=$(2J_A+1)(2J_B+1)(2J_C+1)$. The Boltzmann distribution calculated using g=1 shows excellent agreement with experiment.

The distribution calculated using a degeneracy factor of g=1, however, shows excellent agreement with the experimental distribution. The degeneracy can be treated in this manner because $J_A$, $J_B$, and $J_C$ are not true constants of motion. Sampling all of the *signed* integer triplets of $J_A$, $J_B$, and $J_C$ accounts for the degeneracy of $J$, so no extra degeneracy term needs to be included in the Boltzmann expression. This change in degeneracy affects the results seen by Levene and Valentini. Figure 5.4 shows the rotational distribution resulting from the dissociation of 300 K ozone, assuming a single $j_{diss}$ of 32. The distribution calculated using g=$(2J_A+1)(2J_B+1)(2J_C+1)$ is relatively wide (FWHM=19) and

bifurcated, as reported by Levene and Valentini. If the same calculation is performed using g=1, the distribution narrows and is no longer bifurcated.

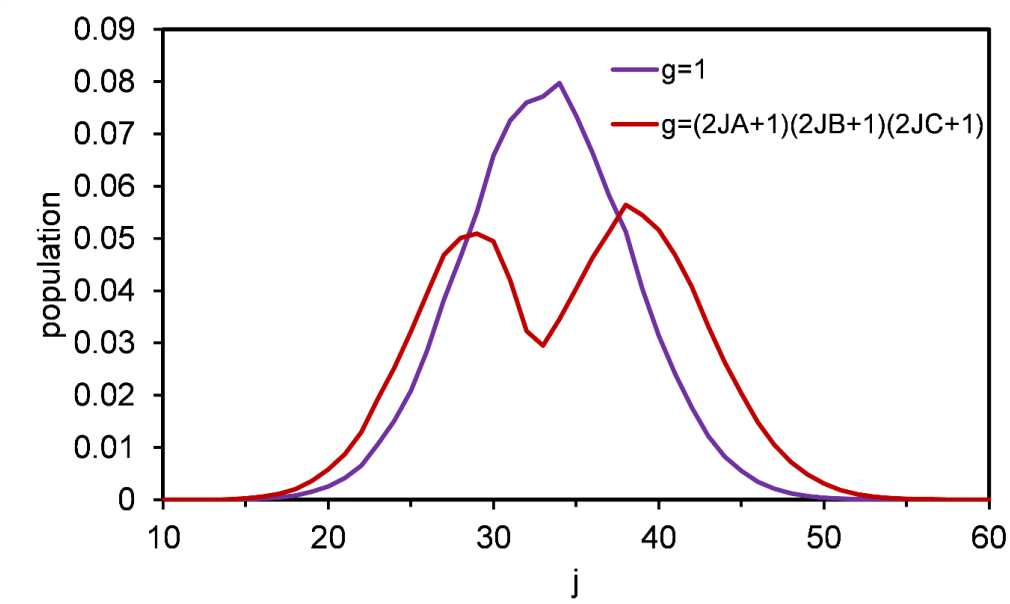


Figure 5.4. 300 K model results with with a $j_{diss}$ of 32. The purple trace is calculated using a degeneracy factor of g=1 in calculating the Boltzmann weighting of the parent distribution while the red trace uses $g=(2J_A+1)(2J_B+1)(2J_C+1)$.

The g=1 distribution is narrower than the $O_2(\,^3\Sigma_g^-)$ experimental distribution reported by Levene *et al.*[64, 80] (FWHM of 12 and 16, respectively), so there is no need to invoke a correlation between the directions of $j_{diss}$ and rotation about the C axis to explain the results. Figure 5.5 shows the rotational distribution resulting from the at threshold dissociation of 300 K ozone calculated with g=1. While the corresponding distribution calculated by Levene and Valentini was well described

by a 300 K Boltzmann distribution, the distribution calculated with g=1 is well described by a slightly colder 200 K Boltzmann distribution. Although the rotational temperature for the distributions calculated using $g=(2J_A+1)(2J_B+1)(2J_C+1)$ and g=1 are different, both distributions are well described by a Boltzmann distribution supporting the theory that the thermal rotational energy of the parent is transferred to rotational motion in the fragment.

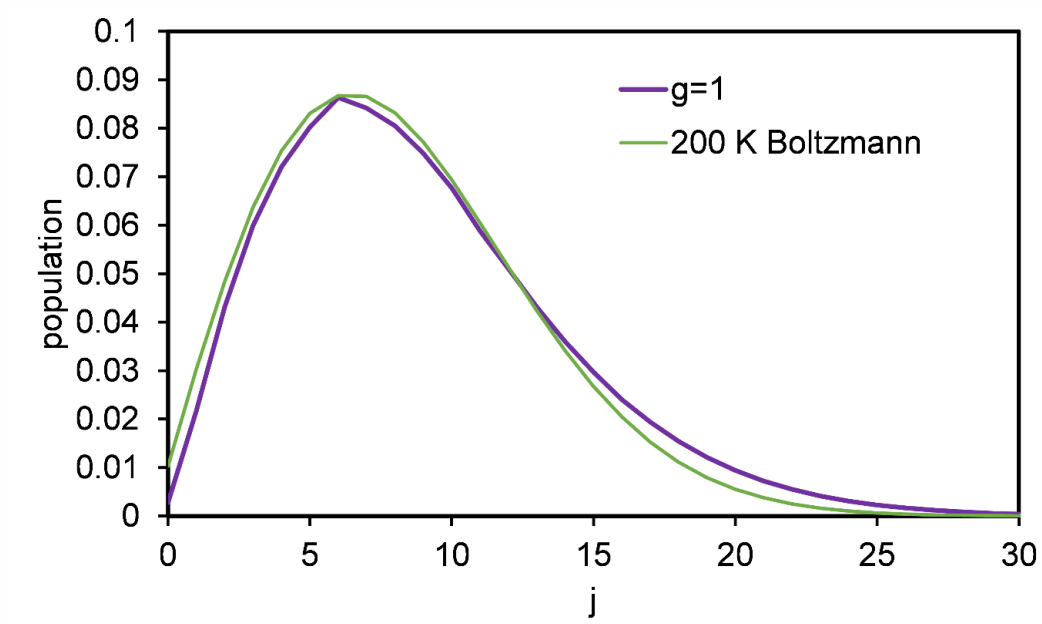


Figure 5.5. Model results for an at threshold dissociation at 300 K with parent ozone populations weighting by a Boltzmann distribution with g=1. A 200 K $O_2(\,^3\Sigma_g^-)$ Boltzmann distribution is shown for comparison.

Another major difference between the current model and the model of Levene and Valentini is the treatment of $j_{diss}$. Instead of using the impulsive model

to determine $j_{diss}$ our modified model used calculated 0 K rotational distributions by McBane.[26, 81] The rotational distributions are the result of semiclassical trajectory calculations, which include surface hopping. In these calculations trajectories are started on the B state with an initial total angular momentum of zero. Similar to the results for a single $j_{diss}$ the final rotational distribution broadens and shifts with increasing parent temperature, as shown in Figure 5.6. The 0 K and 60 K distributions peak at $j$=21 while the 175 K and 300 K distributions peak at $j$=22. The FWHM of the 0 K distribution is 14.5 and the FWHM of the 300 K distribution is 18.6. We have neglected parent ozone zero-point vibrational motion in our model.

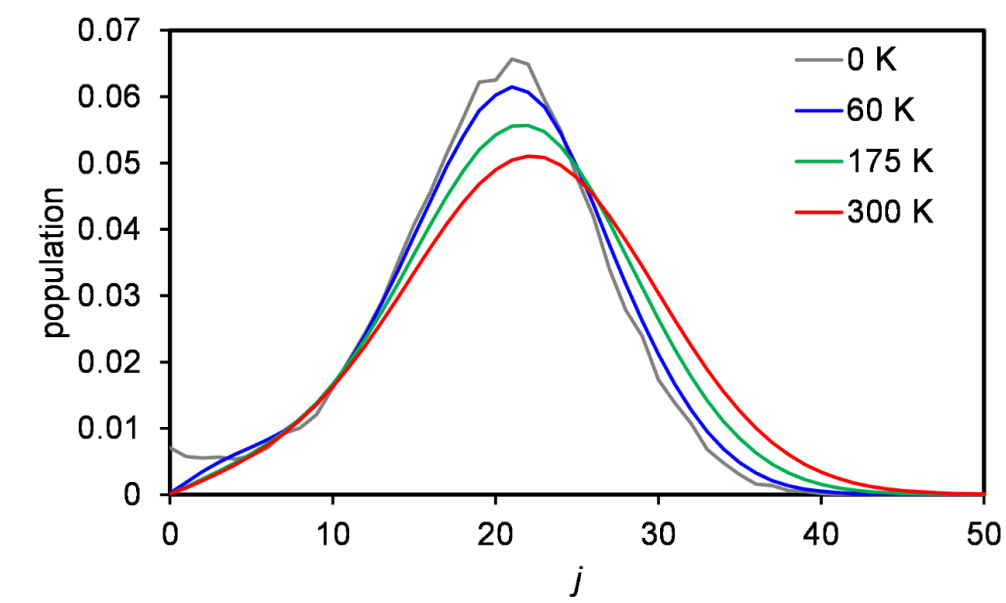


Figure 5.6. $O_2(a^1\Delta_g, v=0)$ rotational distribution resulting from the 266 nm photolysis of 0 K ozone compared to rotational distributions calculated with parent ozone temperatures of 60, 175, and 300 K.

Once the model is used to calculate the magnitude and direction of $j_{O2}$, the Λ-doublet propensity and **v-j** correlation can be calculated. When *j* is normal to the original molecular plane, the fragment rotates in the molecular plane and to conserve the A′ symmetry of the B state the A′ Λ-doublet is formed. As *j* is tilted away from normal to the molecular plane, the symmetry with respect to the original molecular plane is conserved by a linear combination of the two Λ-doublets. The greater the tilt, the larger the contribution from the A″ Λ-doublet. The probability of forming one Λ-doublet over the other is determined by its weighting in the symmetry conserving linear combination. The probability of forming the two Λ-doublets for a given $j_{diss}$, $J_A$, $J_B$, $J_C$ combination can be calculated with the following equations:

$$f(A') = cos^2\gamma \tag{5.5}$$

$$f(A'') = sin^2\gamma \tag{5.6}$$

where $\gamma$ is the angle the *j* vector is displaced from the normal to the molecular plane (see Figure 5.7). The equations were derived following the work of Bronikowski and Zare[82] and were selected so the probability of forming the A′ Λ-doublet is 1 when $\gamma = 0°$ and 0 when $\gamma = 90°$. The resulting A′ and A″ fractions for *j*=18 fragments resulting from photodissociation of ozone at 266 nm as a function of temperature are shown in Figure 5.8.

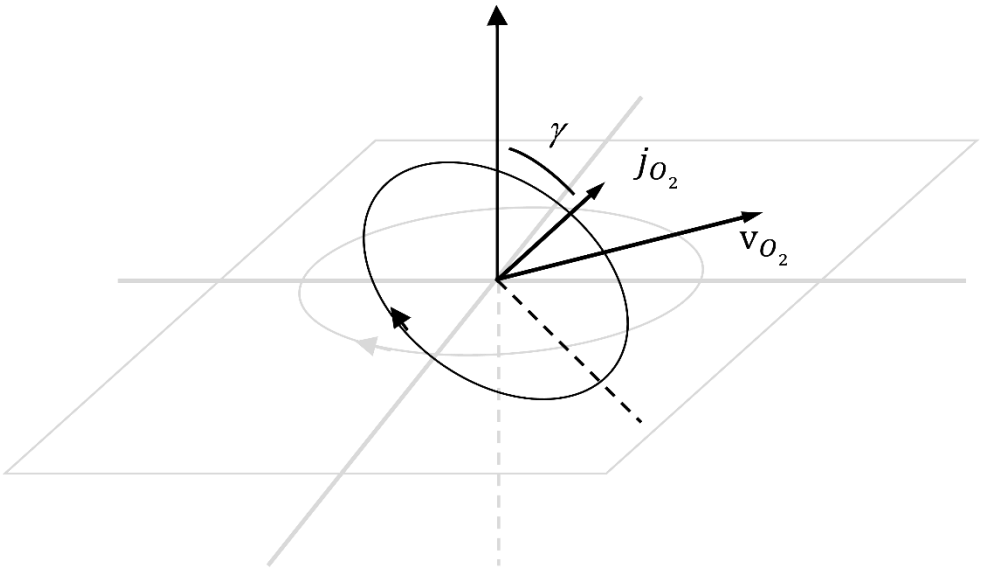


Figure 5.7. Depiction of tilt of the fragment angular momentum vector and rotational plane due to parent rotation. The original molecular plane is shown in gray.

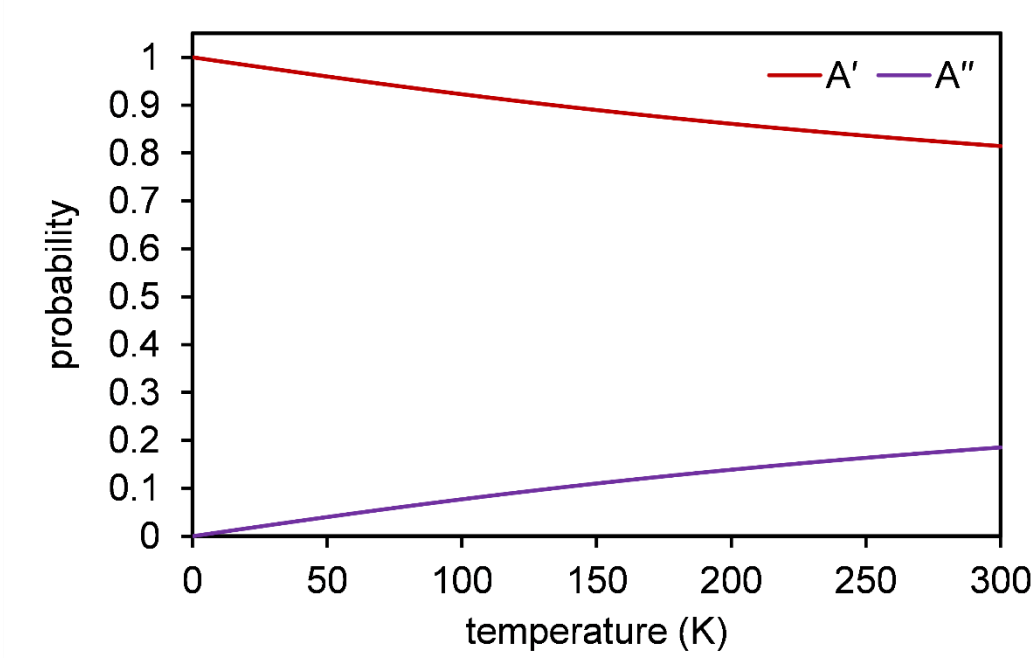


Figure 5.8. Model A′ and A″ fractions calculated for *j*=18 fragments resulting from the 266 nm photodissociation of ozone.

To calculate the **v-j** correlation, the position of the recoil velocity vector had to be estimated. It was assumed that **v** remains in the initial molecular plane. The $\beta_0^2(20)$ value of 0.75 measured by Dylewski *et al.* was used to determine the average angle between **v** and **μ** (A axis) which is 24°. The angle between **v** and **j** was calculated for each $j_{diss}$, $J_A$, $J_B$, $J_C$ combination and was used to calculate a $\beta_0^0(22)$ value. To calculate rotational population and **v-j** distributions, each $j_{diss}$, $J_A$, $J_B$, $J_C$ combination, along with its corresponding A′/A″ fractions and **v-j** correlation, was binned into integer *j* values according to the magnitude of the resulting $j_{O_2}$ vector. Binning followed regular rounding rules. The average A′/A″ fractions were determined for each *j* bin, with weightings determined by the probability of forming the specific $j_{diss}$ in the 0 K rotational distribution and the Boltzmann weighting of the specific $J_A$, $J_B$, $J_C$ combination. The average **v-j** correlations were calculated in the same way but with the additional step of weighting by the individual A′ or A″ fractions in order to obtain separate **v-j** correlations for the even and odd fragments, respectively. For even *j*-states the A′ **v-j** correlation was reported, and for odd *j*-states the A″ **v-j** correlation was reported. The model **v-j** correlations for *j*=17 and *j*=18 fragments following photolysis at 266 nm as a function of temperature are shown in Figure 5.9. The difference between the **v-j** correlations for the odd and even rotational states increases with temperature, as observed experimentally.

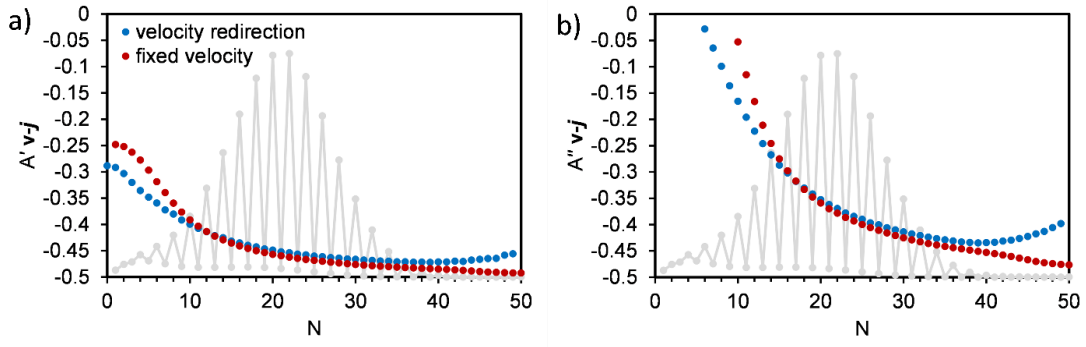


Figure 5.9. Model **v-j** correlations for j=17 and j=18 fragments following the 266 nm photodissociation of ozone as a function of parent temperature.

To test the validity of the assumption that **v** remains fixed in the original molecular plane, Hall developed a modified model that took into consideration the redirection of the velocity vector due to parent rotation. As can be seen in Figure 5.10, there is good agreement for the **v-j** correlations predicted by both models. The two models begin to diverge at high and low-*j* where there is low population predicted by the model.

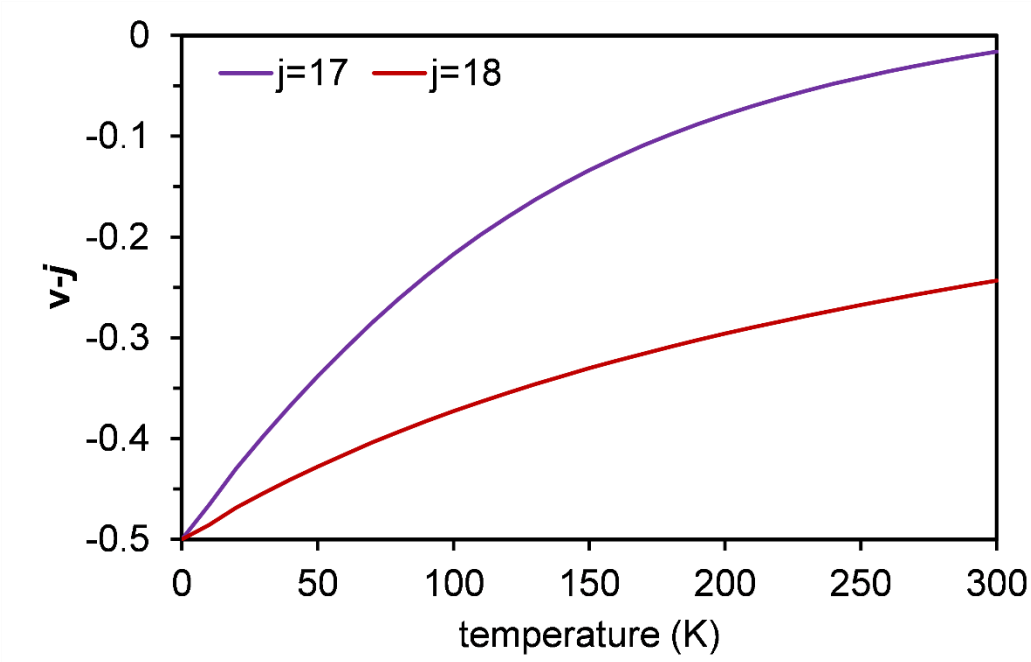


Figure 5.10. Calculated **v-j** correlations at 70 K with and without velocity redirection. Panel a) shows the **v-j** correlation for the A′ fragments, and panel b) shows the **v-j** correlation for the A″ fragments. The calculated rotational distribution is shown in gray for reference.

## 5.2. Results

### *5.2.1. Scalar Properties*

One prediction of the model is that A″ fragments originate from a hotter parent population than the A′ fragments. This prediction arises from the fact that the probability of forming a A″ state increases with increasing out-of-plane rotation, as illustrated in Figure 5.11.

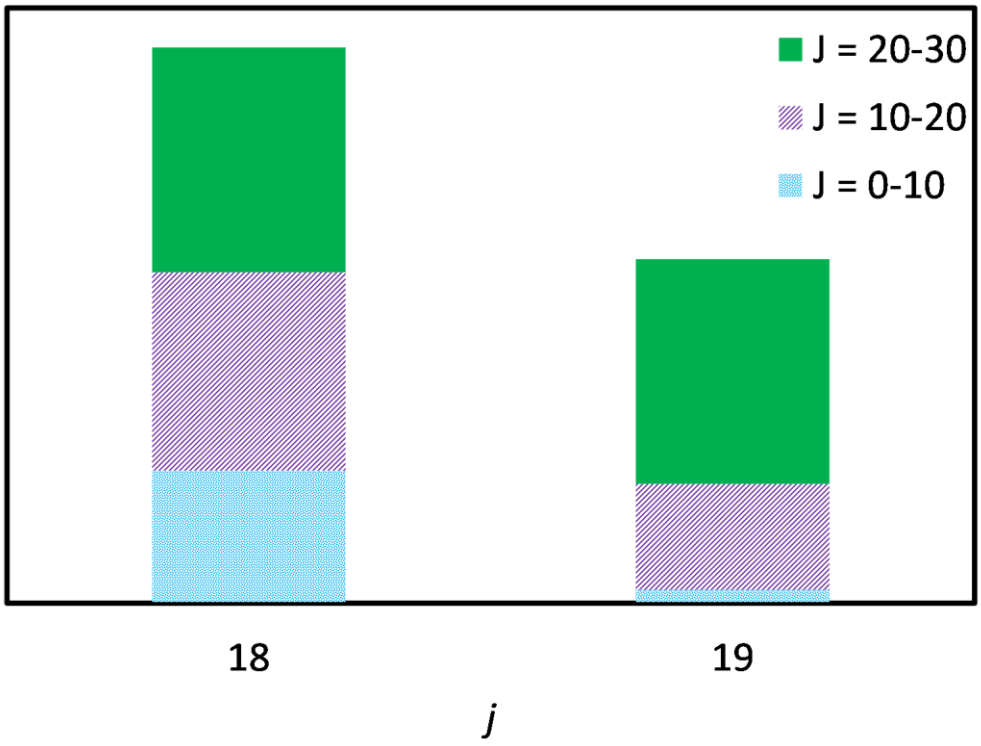


Figure 5.11. Schematic comparing parent contributions to an even (j=18) and odd (j=19) rotational state. As the probability of forming an odd-state increases with parent rotation, the odd-states arise from a hotter parent population than the even-states.

Evidence for this phenomenon was seen in the speed distributions of the $O_2(a^1\Delta_g)$ fragments. According to conservation of energy, the fragment speed is expected to decrease with increasing fragment rotation, because the more energy that is partitioned into rotation, the less that is available for translation. As can be seen in Figure 5.12, in a 70 K beam the $j$=18 and $j$=19 fragments recoil with approximately the same speed, even though there is a 54 $cm^{-1}$ difference in rotational energy between the two fragments. If conservation of energy is used to calculate the amount of parent energy necessary for the fragments to recoil with

the measured speed, it is found that 58 $cm^{-1}$ of parent energy is needed for the *j*=18 and *j*=20 fragments, while 99 $cm^{-1}$ is needed for the *j*=19 fragment, indicating that the odd states do originate from a more excited parent population. The difference in parent internal energy required is 41 $cm^{-1}$, which is close to the 54 $cm^{-1}$ difference in rotational energy.

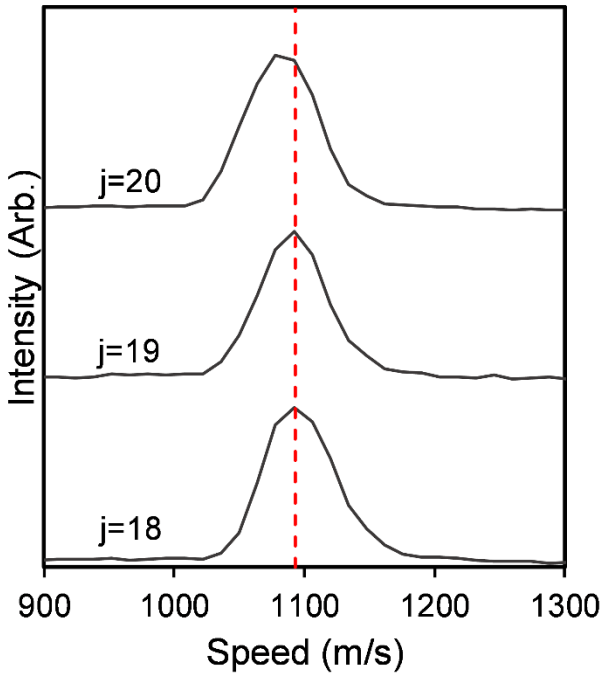


Figure 5.12. Speed distributions of the O2(a1Δg, v=0, j=18, 19, 20) fragments resulting from the photodissociation of 70 K ozone. The red dotted line is a guide to the eye. Figure reprinted from Gunthardt *et al. J. Chem. Phys.* **151**, 224302 (2019), with the permission of AIP Publishing.

The model and experimental $O_2(a^1\Delta_g, v=0)$ rotational distributions following photolysis at 266 nm and 60 K are shown in Figure 5.13. To compare model and

experimental population distributions, the rotational angular momentum quantum number N is used. The spectroscopic community typically uses the total angular momentum quantum number *j*, which includes contributions from rotational, orbital, and electron spin angular momenta. In the case of $O_2(a^1\Delta_g)$, molecules have 2 quanta of orbital angular momentum and no electron spin angular momentum, so for the experimental measurements *j* represents the sum of orbital and rotational angular momentum, i.e. $j$=N+2. The model, however, neglects the 2 quanta of orbital angular momentum, so for the model the total angular momentum is equal to the rotational angular momentum, i.e. $j$=N. It can be seen that the odd/even population distribution is clearly reproduced in the model distribution.

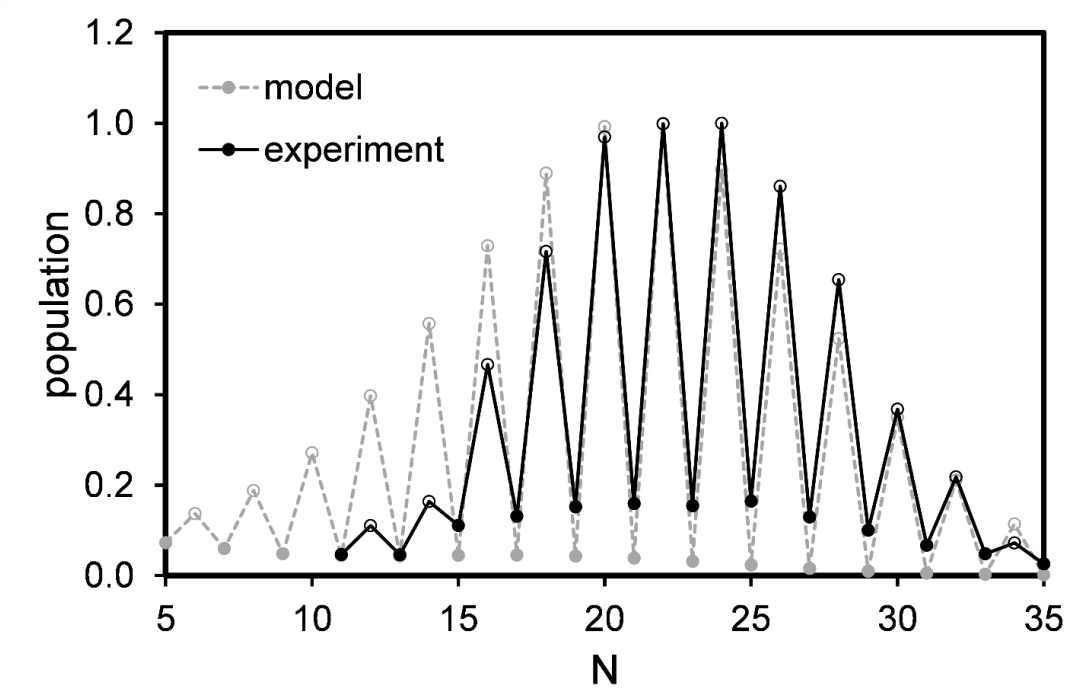


Figure 5.13. Model and experimental $O_2(a^1\Delta_g, v=0)$ rotational distribution following the 266 nm photodissociation of 60 K ozone.

The model distribution is slightly colder than the experimental distribution and the predicted odd state populations are less than what is observed experimentally. Overall, however, the agreement is quite good. The results for the v=0 fragments resulting from photodissociation at 282 nm and 60 K are shown in Figure 5.14. Due to congestion in the low *j* region of the spectrum is it difficult to get accurate low *j* experimental populations, so experimental results for N ≤ 4 have been omitted from the figure. The agreement between model and experiment is excellent, and has improved compared to the results at 266 nm.

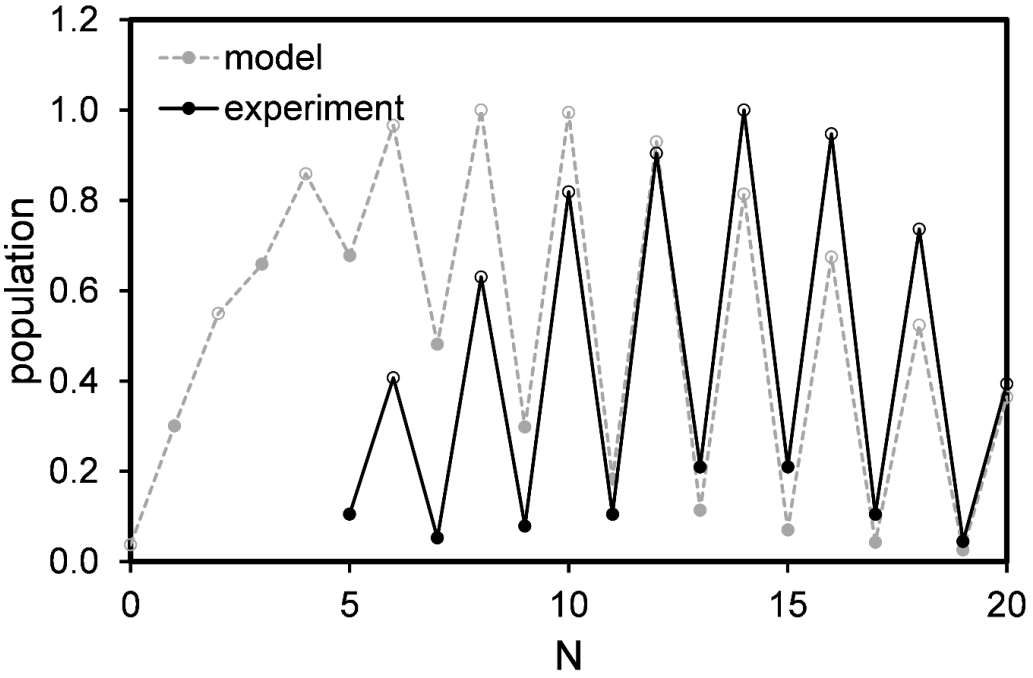


Figure 5.14. Model and experimental $O_2(a^1\Delta_g, v=0)$ rotational distribution following the 282 nm photodissociation of 60 K ozone. Figure reprinted from Gunthardt *et al. J. Chem. Phys.* **151**, 224302 (2019), with the permission of AIP Publishing.

The model was also used to predict rotational distributions at 300 K to compare to the more extensive experimental results by Valentini *et al.*[17] The results for the 266 nm photodissociation of ozone at 300 K for v=0, v=1, and v=3 fragments are shown in Figure 5.15.

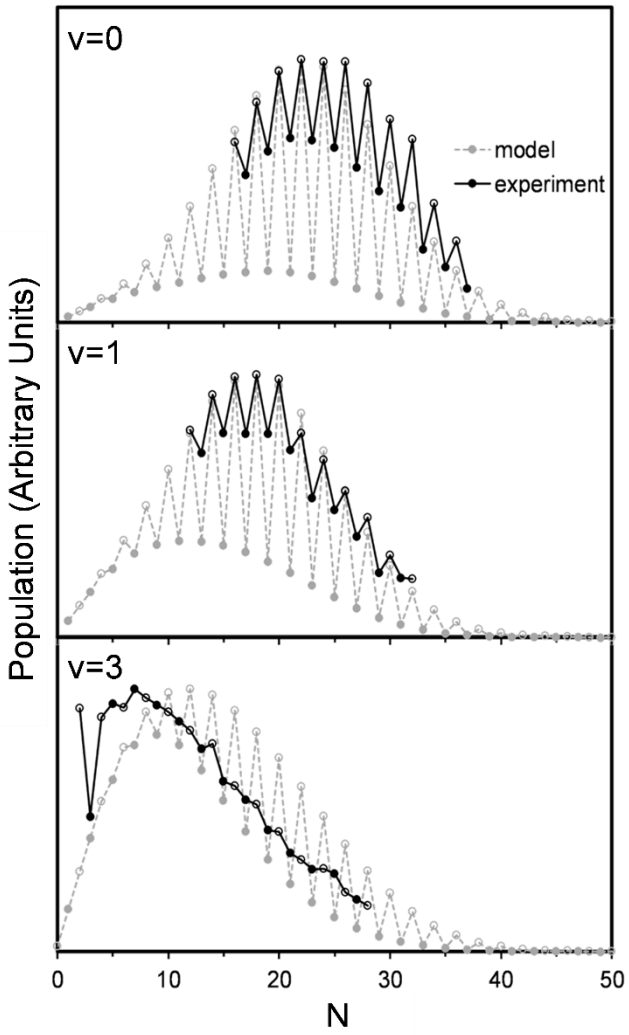


Figure 5.15. Model and experimental[17] $O_2(a^1\Delta_g$, v=0, 1, 3) rotational distributions following the 266 nm photodissociation of 300 K ozone. Figure reprinted from Gunthardt *et al. J. Chem. Phys.* **151**, 224302 (2019), with the permission of AIP Publishing.

Parent rotation has broadened and shifted the envelope of model rotational distribution, which is in excellent agreement with experimental results. It can be seen that the degree of odd/even alternation predicted by the model for the v=0 fragments has decreased going from 60 to 300 K, qualitatively capturing the

temperature dependence of the alternation. While the model overestimates the magnitude of the population alternation for all vibrational states, the model clearly captures the trend of decreasing alternation with increasing fragment vibrational state. The results for dissociation at 240 nm and 300 K are shown in Figure 5.16. It can be seen that the alternation at 240 nm is stronger than at 266 nm, replicating the experimentally observed dependence on photolysis wavelength. The model suggests that this trend, as well as the trend of decreasing alternation with increasing vibrational state, is a result of the rotational distributions shifting to lower N. The smaller $j_{diss}$ relative to the rotational motion imparted by out-of-plane motion of the parent, the greater the tilt of $j_{O2}$ and the more odd states are produced.

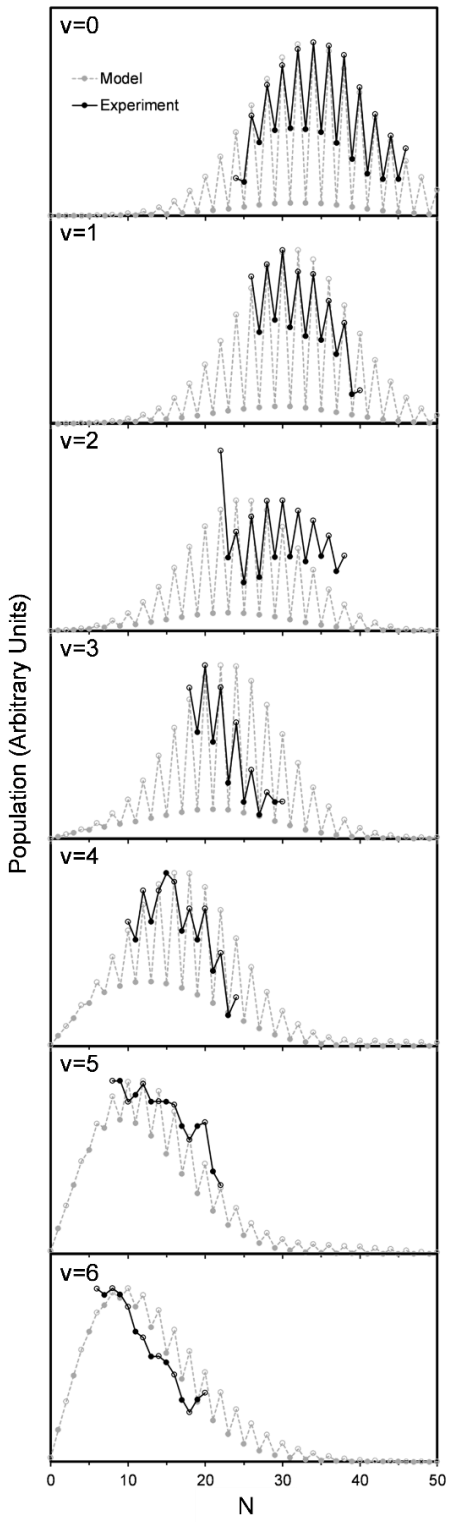


Figure 5.16. Model and experimental[17] O2(a1Δg, v=0-6) rotational distributions following the 240 nm photodissociation of 300 K ozone. Figure reprinted from Gunthardt *et al. J. Chem. Phys.* **151**, 224302 (2019), with the permission of AIP Publishing.

### *5.2.2. Vector Correlations*

To compare the center-of-mass model **v-j** results to the laboratory frame experimental results, depolarization due to parent thermal velocity must be included.[83-86] The equations for thermal depolarization of the **v-j** correlation are similar to those derived for the depolarization of the **μ-v** correlation.[87] The depolarization factor applied to the model **v-j** correlation is calculated using the following equation,

$$\frac{\beta_0^0(22)_{LAB}(v)}{\beta_0^0(22)_{COM}} = \frac{I_{5/2}(vu/\sigma^2)}{I_{1/2}(vu/\sigma^2)} \tag{5.7}$$

where $I_{5/2}$ and $I_{1/2}$ are the modified spherical Bessel functions, $v$ and $u$ are the laboratory-frame and center-of-mass speeds, respectively, and $\sigma^2 = k_b T/m$. The depolarization factor for a *j*=20 fragment resulting from the 266 nm dissociation of ozone as a function of temperature is shown in Figure 5.19. The **v-j** results were further depolarized by the Busch and Wilson depolarization factor (eq 4.5). The depolarized model results are compared to the experimental results in Table 5.1. The trend of decreasing correlation with increasing temperature is qualitatively reproduced by the model, although the magnitude of depolarization is greater in the experiment than in the model. Most importantly the odd/even alternation in the **v-j** correlation is reproduced by the model. The modified model of Hall also predicted **μ-j** correlations. The model and experimental **μ-j** results are shown in Table 5.2. While all of the experimental values are more depolarized than

predicted by the model, the model captures the temperature dependent trend, as well as the odd/even alternation.

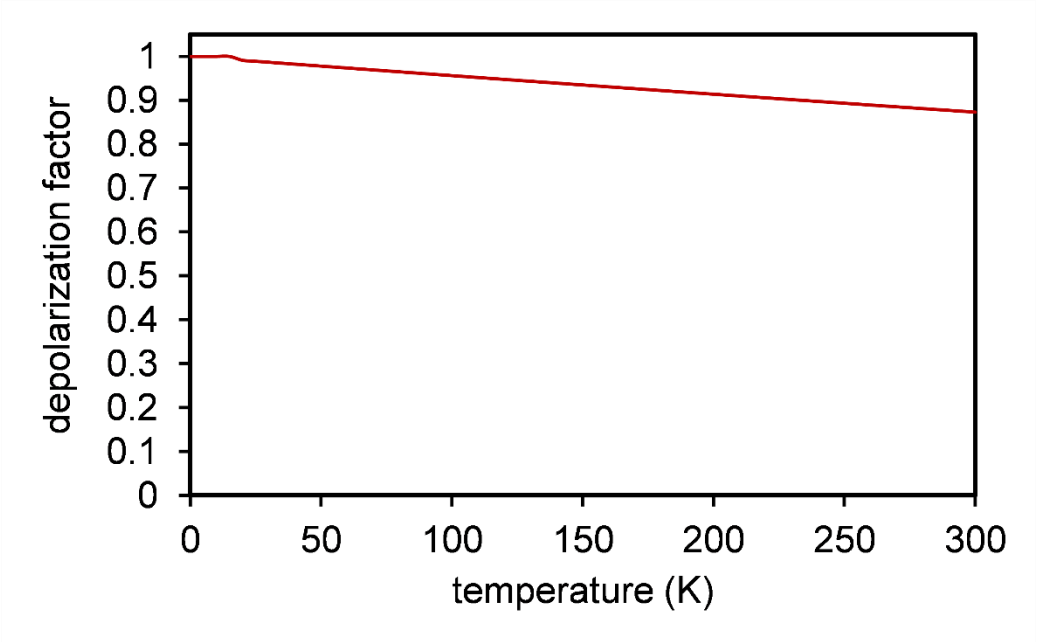


Figure 5.17. Depolarization factor for **v-j** correlation calculated for a j=20 fragment resulting from 266 nm photodissociation of ozone as a function of temperature.

Table 5.1. Model and experimental $\beta_0^0(22)$ values for $O_2(a^1\Delta_g)$ fragments resulting from the 266 nm photolysis of ozone. Experimental results are given in parenthesis. Two quanta have been added to the model results to account for the orbital angular momentum of the $O_2$ fragment.

| $\boldsymbol{\beta_0^0(22)}$ | *j*=18 | *j*=19 | *j*=20 |
|---|---|---|---|
| 70 K | -0.39 | -0.29 | -0.40 |
| | (-0.32 ± 0.08) | (-0.22 ± 0.07) | (-0.33 ± 0.09) |
| 115 K | -0.35 | -0.19 | -0.35 |
| | (-0.14 ± 0.08) | (-0.07 ± 0.16) | (-0.23 ± 0.20) |
| 170 K | -0.31 | -0.11 | -0.31 |
| | (-0.10 ± 0.09) | (0.01 ± 0.06) | (-0.14 ± 0.06) |

Table 5.2. Model and experimental $\beta_0^2(02)$ values for O2(a1Δg) fragments resulting from the 266 nm photolysis of ozone. Experimental results are given in parenthesis. Two quanta have been added to the model results to account for the orbital angular momentum of the O2 fragment.

| $\boldsymbol{\beta_0^2(02)}$ | *j*=18 | *j*=19 | *j*=20 |
|---|---|---|---|
| 70 K | -0.48 | -0.43 | -0.48 |
| | (-0.34 ± 0.08) | (-0.25 ± 0.08) | (-0.33 ± 0.06) |
| 115 K | -0.47 | -0.39 | -0.47 |
| | (-0.20 ± 0.06) | (-0.09 ± 0.20) | (-0.29 ± 0.22) |
| 170 K | -0.46 | -0.36 | -0.46 |
| | (-0.14 ± 0.15) | (0.07 ± 0.09) | (-0.13 ± 0.01) |

The model results were also compared to the experimental results of Ritchie and coworkers. As can be seen in Figures 5.18-5.22, the model does an excellent job reproducing the experimentally observed alternation. The largest discrepancy is in the 248 nm results where the model predicts odd/even alternation which is not observed experimentally.

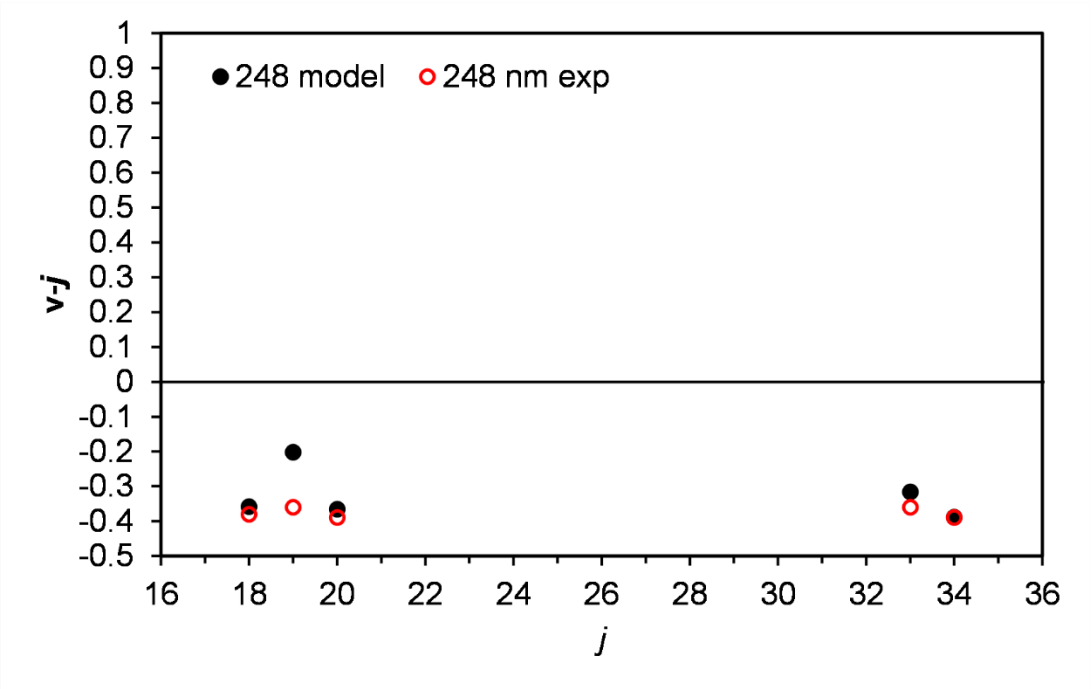


Figure 5.18. Comparison of model results with experimental[29] results at 248 nm. Two quanta have been added to the model results to account for the orbital angular momentum of the O2 fragment.

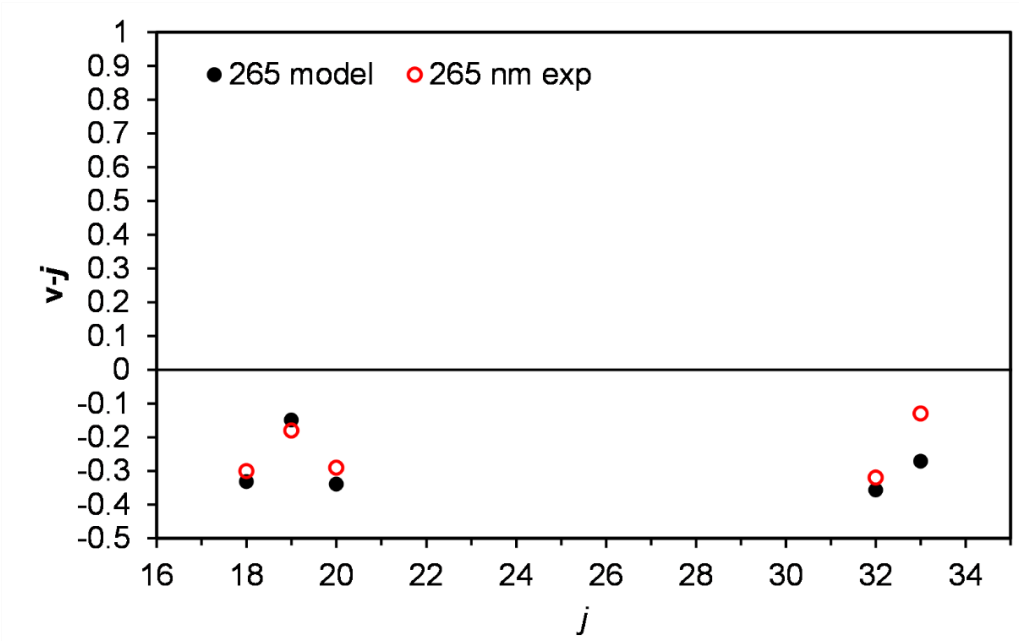


Figure 5.19. Comparison of model results with experimental[29] results at 265 nm. Two quanta have been added to the model results to account for the orbital angular momentum of the $O_2$ fragment.

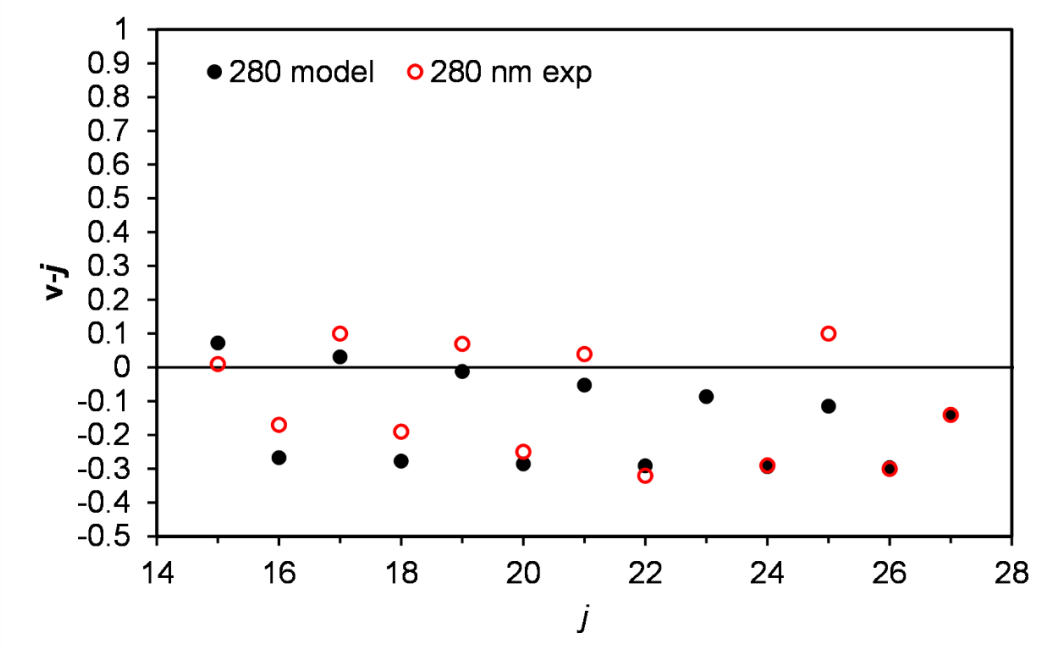


Figure 5.20. Comparison of model results with experimental[28] results at 280 nm. Two quanta have been added to the model results to account for the orbital angular momentum of the O2 fragment.

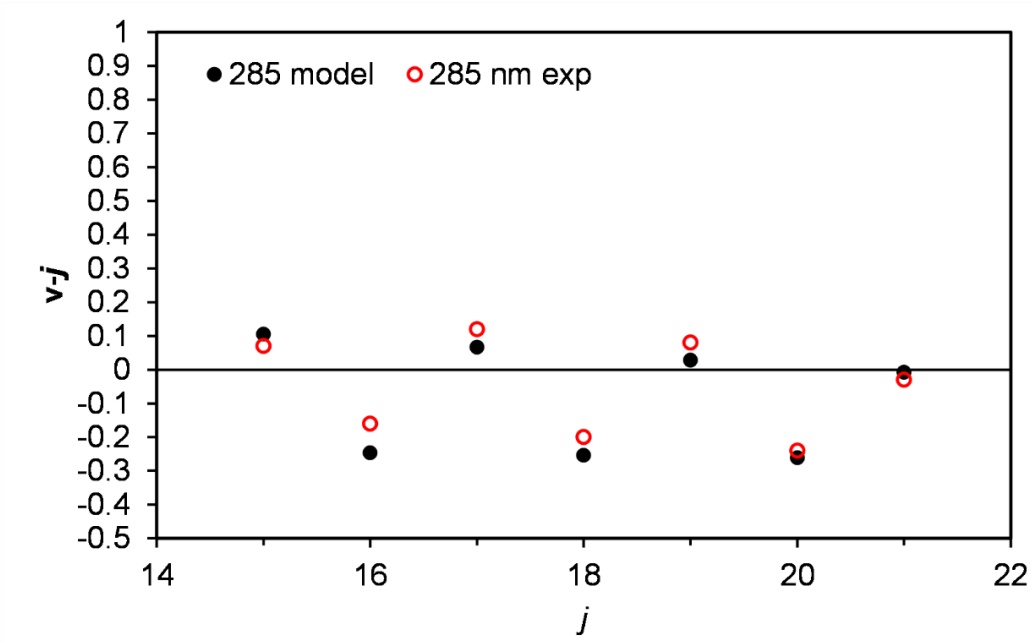


Figure 5.21. Comparison of model results with experimental[28] results at 285 nm. Two quanta have been added to the model results to account for the orbital angular momentum of the $O_2$ fragment.

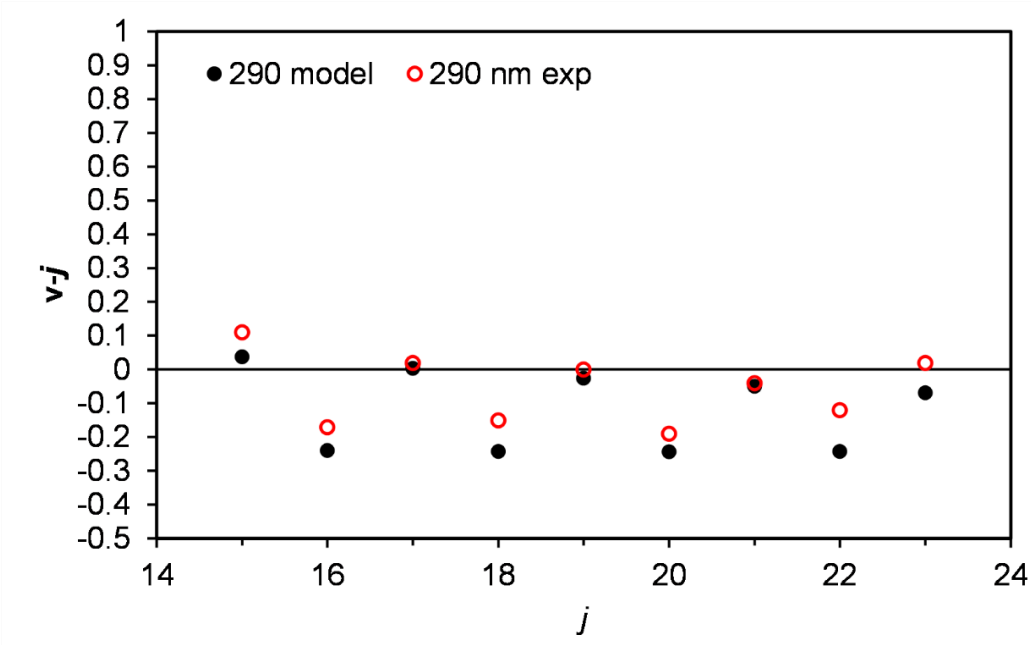


Figure 5.22. Comparison of model results with experimental[28] results at 290 nm. Two quanta have been added to the model results to account for the orbital angular momentum of the O2 fragment.

The simple classical model based on a preference for forming the A′ Λ-doublet successfully reproduces the odd/even alternation in both the rotational population distribution and the **v-j** and **μ-j** correlations. In addition, the model captures the temperature, photolysis wavelength, and vibrational state dependencies of the odd/even population alternation, and the temperature dependence of the vector correlations. The success of the classical model in reproducing these experimental trends provides strong evidence in favor of the Λ-doublet preference model.

# 6. CONCLUSIONS AND FUTURE WORK

## 6.1. Conclusions

This dissertation has provided clear evidence for a Λ-doublet preference in the $O_2(a^1\Delta_g)$ fragments resulting from the photodissociation of ozone in the Hartley band. This Λ-doublet preference is the origin of the odd/even alternation in the $O_2(a^1\Delta_g)$ rotational distribution first observed by Valentini *et al.*[16, 17] with CARS experiments at 300 K and later verified by Warter *et al.*[26] in a jet-cooled molecular beam using 2+1 REMPI. The alternation favors the even rotational states and was found to be temperature dependent, with alternation decreasing with increasing temperature. In the Hartley band, initial excitation is to the B state which has A′ symmetry. As the singlet products are formed from diabatic dissociation on the B state, conservation of symmetry leads to a preferential formation of the A′ Λ-doublet of $O_2(a^1\Delta_g)$. Due to nuclear exchange restrictions, the A′ Λ-doublet of $O_2(a^1\Delta_g)$ can only occupy even rotational states while the A″ Λ-doublet of $O_2(a^1\Delta_g)$ can only occupy odd rotational states. Consequently, a preference for the A′ Λ-doublet leads to a preference for even states in the rotational distribution. Formation of the A″ Λ-doublet is facilitated by parent out-of-plane rotation, so the relative population of odd states in the rotational distribution increases with parent temperature. Ion imaging was used to verify that the **v-j** and **μ-j** correlations are more depolarized for the odd rotational states than for the even rotational states, providing evidence that the odd rotational

states are formed from a rotationally hotter parent population than the even rotational states. The **μ-v** correlation was found to be independent of rotational state parity, as previously reported.[27-30] A simple classical model based on the Λ-doublet propensity model has been developed which qualitatively reproduces the trends observed in the odd/even population alternation as well as the vector correlations.

To provide further evidence for the Λ-doublet preference model, our collaborators (Han, Dawes, Xie, and Guo), ran full quantum scattering calculations which included explicit treatment of the Λ-doublets. Using this method, Han *et al.*[88] were able to reproduce the odd/even alternation in the rotational distribution, marking the first time this phenomenon has been reproduced by theory. The calculated distributions capture the temperature dependence of the alternation and the magnitude of the calculated odd/even alternation at 60 K is in excellent agreement with the experimental distribution reported in Chapter 3, as shown in Figure 6.1. The success of their method provides conclusive evidence that preferential formation of the A′ Λ-doublet is the origin of the odd/even population alternation, and not a parity selective curve-crossing mechanism. Consequently, parity selective curve crossing in ozone cannot be a source of mass-independent isotopic fractionation in the atmosphere.

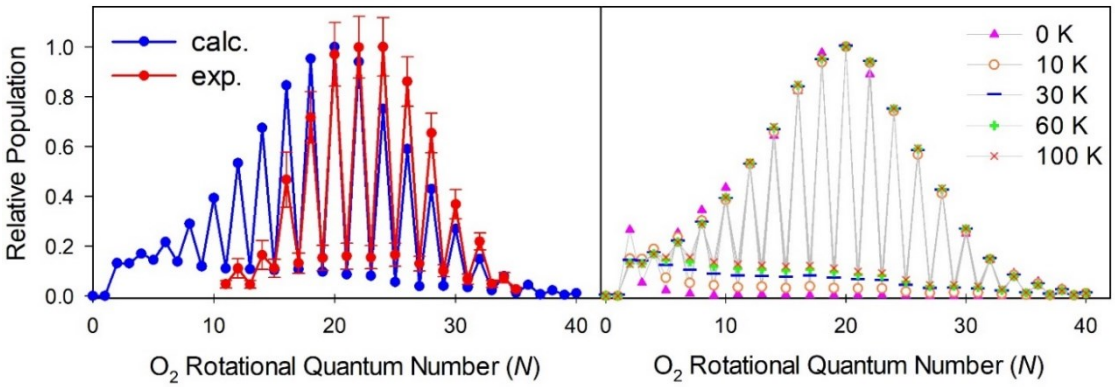


Figure 6.1. Left panel: comparison of calculated and experimental $O_2(a^1\Delta_g, v=0)$ rotational distributions resulting from the 266 nm photodissociation of ozone 60 K. Right panel: comparison of calculated $O_2(a^1\Delta_g, v=0)$ rotational distributions resulting from the 266 nm dissociation of ozone at multiple temperatures. Figure reproduced from Han and Gunthardt *et al.*, *PNAS*, **accepted**, (2020) doi: 10.1073/pnas.2006070117.[88]

## 6.2. Future Studies

It has shown that 2+1 REMPI via the $O_2(d^1\Pi_g, v=4) \leftarrow \leftarrow O_2(a^1\Delta_g, v=0)$ transition can be used to accurately measure $O_2(a^1\Delta_g)$ rotational distributions.[26] While this dissertation focuses on the $O_2(a^1\Delta_g)$ rotational distributions resulting from photodissociation in the Hartley band, theoretically the rotational distributions of the $O_2(a^1\Delta_g)$ photofragments resulting from ozone dissociation in different bands can be characterized as well using this detection scheme.

### *6.2.1. Ozone Photodissociation in the Huggins Band*

There are three energetically allowed channels in the Huggins band, the triplet channel and the following three spin forbidden channels:

$$O_3 + h\nu \rightarrow O_2(a^1\Delta_g) + O(^3P) \quad 6.1$$

$$\rightarrow O_2(b\ ^1\Sigma_g^+) + O(^3P) \quad 6.2$$

$$\rightarrow O_2(X\ ^3\Sigma_g^-) + O(^1D) \quad 6.3$$

Previous studies have found that the yields of the three $O(^3P)$ producing channels are approximately equal.[89, 90] The calculated transition dipole moments between the ground and triplet states are extremely small.[91] Accordingly, it is expected that for the spin forbidden channels initial excitation is to the B state and followed by a crossing to a triplet state facilitated by spin-orbit coupling. Based on calculations, there are five triplet surfaces that diabatically correlate to $O_2(a^1\Delta_g)$ + $O(^3P)$ and cross the B state.[90] If the rotational state of the $O_2(a^1\Delta_g)$ fragment is determined after the crossing, the $O_2(a^1\Delta_g)$ rotational distribution may indicate the symmetry of the triplet state(s) involved in channel 6.1. A propensity for even states would indicate that the triplet state has A′ symmetry while a propensity for odd states would indicate that the triplet state has A″ symmetry. In addition, the Huggins band is highly structured due to vibrational excitation of ozone in the bound B state. It would be interesting to see how the $O_2(a^1\Delta_g)$ rotational distribution changes when different vibrational bands are excited with the photolysis laser.

One challenge to collecting an $O_2(a^1\Delta_g)$ REMPI spectrum in the Huggins band is the presence of one-color signal from the photolysis laser, as shown in Figure 2.18 of the dissertation by Kelleher.[92] The wavelength range from 320-330 nm includes REMPI signal originating from $O_2(X\ ^3\Sigma_g^-)$, $O_2(a^1\Delta_g)$, and $O_2(b\ ^1\Sigma_g^+)$

fragments. Another challenge is that $O_2(a^1\Delta_g)$ can be formed by two channels at these photolysis wavelengths. Vibrationally excited parent molecules have enough energy to reach the singlet channel and form $O_2(a^1\Delta_g)$ fragments in addition to the $O_2(a^1\Delta_g)$ fragments formed through equation 1.1. Fortunately, the products arising from different channels will have different velocities, resulting in signal at different radii on the image. While it is possible to use a mask to block the undesired signal, a more elegant way of conducting the experiment would be to use 2-D REMPI.[93, 94] In 2-D REMPI an image is collected at each wavelength step and the image intensity is integrated as a function of radius. Using this method REMPI spectra for multiple channels can be obtained simultaneously assuming the velocity of the fragments from the two channel is sufficiently different. Figure 6.2 shows a 2D-REMPI spectrum of the CO fragments resulting from the 308 nm photodissociation of acetaldehyde.[94] The top panel shows the 2D-REPMI spectrum which is composed of the 1D image arrays collected at each wavelength. The bottom panel shows the traditional 1D-REMPI spectra, extracted from the 2D-REMPI spectrum by integrating signal as a function of image radius. Using this method, Lee *et al.* were able to simultaneously determine the CO photoproduct rotational distributions resulting from two separate roaming channels in acetaldehyde.

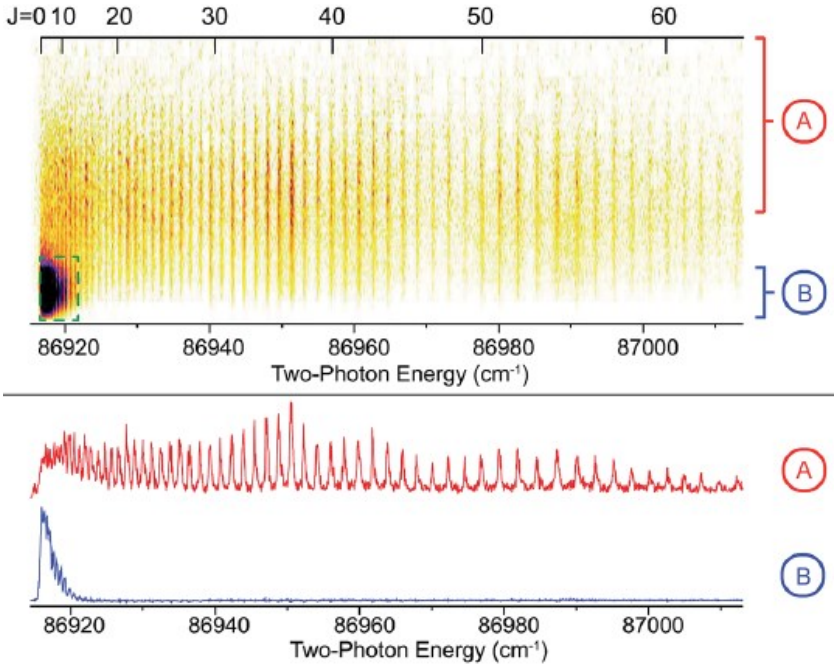


Figure 6.2. Top panel: 2D-REMPI spectrum of CO photoproducts resulting from the 308 nm photodissociation of acetaldehyde. A and B represent the low and high speed fragments, respectively. Bottom panel: Traditional 1D-REMPI spectra extracted from the 2D-REMPI spectrum by integrating as a function of image radius. Figure reproduced from Lee *et al., Chem.l Sci.* **5**, 4633 (2014)[94] with permission from the Royal Society of Chemistry.

### *6.2.2. Ozone Photodissociation at 226 nm*

Possible future studies include experiments involving the photodissociation of ozone at shorter wavelengths. One possible experiment involves probing the $O_2(a^1\Delta_g)$ fragments resulting from ozone photodissociation at 226 nm using 2+1 REMPI via the $O_2(d^1\Pi_g, v=4) \leftarrow \leftarrow O_2(a^1\Delta_g, v=0)$ transition. Classical trajectory calculations by McBane[95] predict that the rotational distribution of the $O_2(a^1\Delta_g)$ photofragments resulting from the 226 nm photolysis of ozone will be significantly

hotter than that at 266 nm (see Figure 6.3). The calculated rotational distribution peaks at *N*=38 and has a FWHM of around 19, including the shoulder at high *N*.

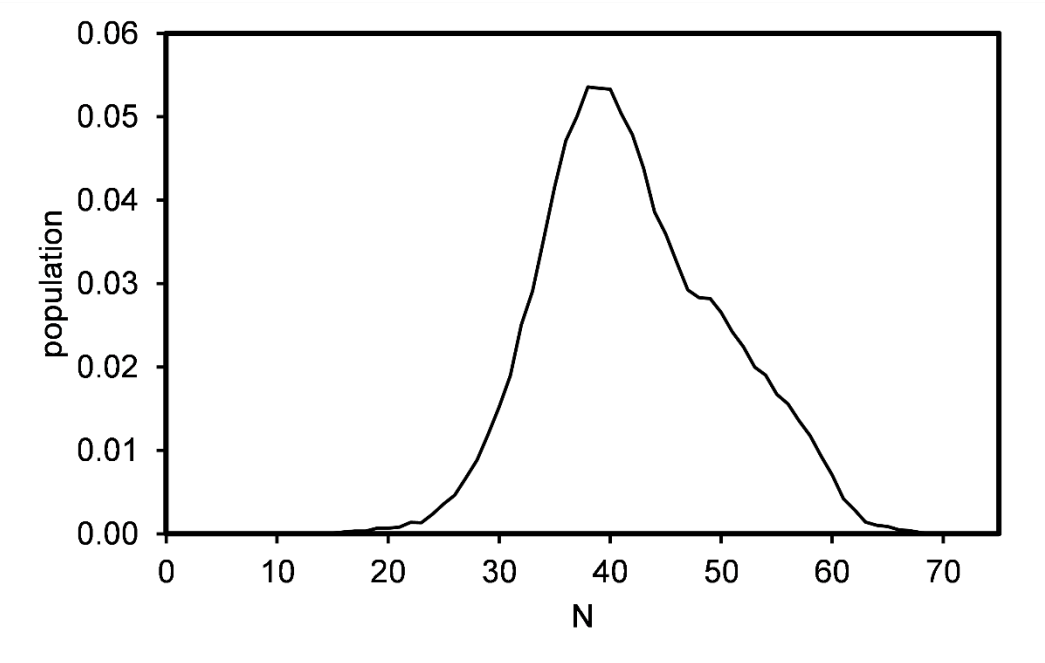


Figure 6.3. Calculated rotational distribution of the $O_2(a^1\Delta_g)$ fragments resulting from the photodissociation of ozone at 226 nm.[95]

Of particular interest are the linewidths of these high *j* fragments in the $O_2(d^1\Pi_g$, v=4) $\leftarrow \leftarrow O_2(a^1\Delta_g$, v=0) 2+1 REMPI spectrum. As discussed in Chapter 3, the $O_2(d^1\Pi_g$, v=4) state undergoes *j* dependent predissociation due to its interaction with a nearby $^1\Pi$ state. Determining accurate linewidths at high *j* states will provide insight into the nature of the predissociation and will provide a benchmark for computational models. A study by Li *et al.*[96] used ab initio calculations to

determine the coupling of the two states and predict the $O_2(d^1\Pi_g, v=4)$ linewidths. As seen in Figure 6.4, the calculated results show excellent agreement with the empirical linewidths from Chapter 3 for *j* values 10 to 15, but diverges from experiment as *j* increases. As the $O_2(a^1\Delta_g)$ rotational distribution following ozone photodissociation a 226 nm is expected to have population in these higher *j* states, measuring accurate linewidths would allow for refinement of the experimental data in this region. In addition to measuring linewidths, access to high *j* states provides the potential to refine the rotational constants for $O_2(a^1\Delta_g)$. In order to refine these rotational constants, the accuracy of the dye laser calibration must be improved. This can be achieved by using an iodine cell, as iodine has many absorption features in the appropriate wavelength range. Another method is to use an etalon in conjunction with an optogalvanic lamp.

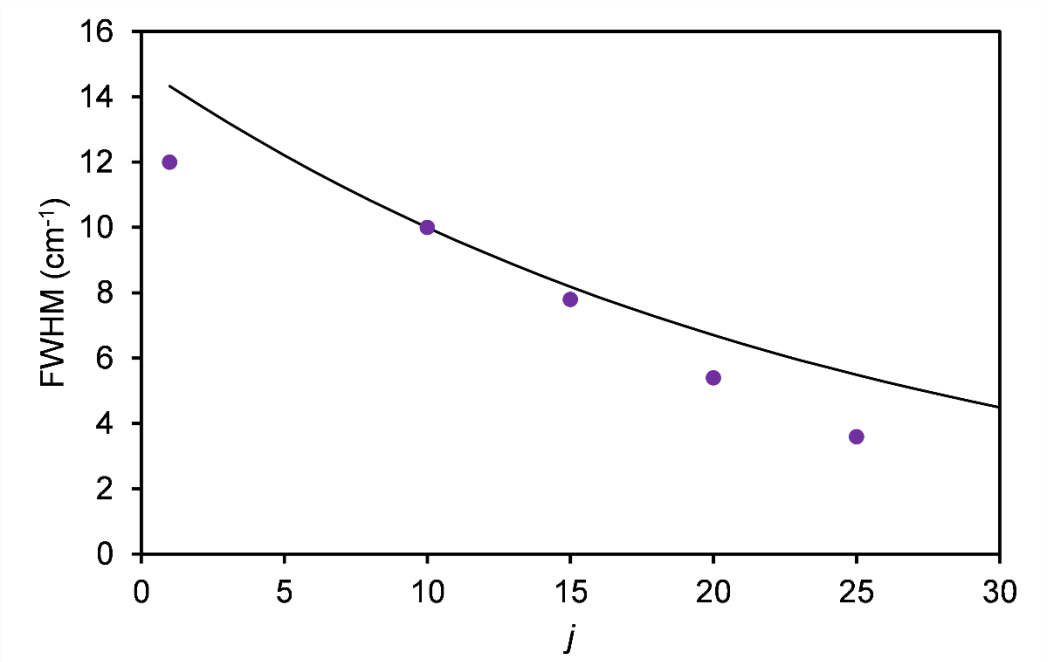


Figure 6.4. Comparison of $O_2(d^1\Pi_g)$ linewidths calculated by Li *et al.*[96] (closed circles) with the empirical exponential used to fit the REMPI spectrum in Chapter 3 (solid line).

### *6.2.3. Ozone Photodissociation at 193 nm*

The photodissociation of ozone in the VUV is much less understood than photodissociation in the Hartley band. As seen in Figure 6.5, to the blue of the Hartley band is a small absorption feature, followed by a larger absorption feature which has been attributed to excitation to Rydberg states.[97] While much of the VUV wavelengths are not atmospherically relevant, some light around 190 nm penetrates the stratosphere, due to gaps in the Schumann-Runge absorption bands of $O_2$. Accordingly, most of the VUV studies have focused on the wavelength of 193 nm, which can be produced with an ArF excimer. In the VUV nm, many more channels are energetically accessible, including the triple

dissociation of ozone into three oxygen atoms. Evidence for the triple dissociation channel has been seen at 157 nm,[98] and 193 nm.[99, 100] It is believed that the triple dissociation is a concerted process.[100] Interestingly, the **μ-v** correlations measured at 193 nm are negative, as opposed to the positive correlations observed throughout the Hartley band.[100, 101] A negative **μ-v** correlation is indicative of a perpendicular transition, suggesting that excitation at 193 nm involves states other than the B state. In ozone, excitation to states with $^1A_1$ or $^1B_1$ symmetry in $C_{2v}$ ($^1A'$ or $^1A''$ in $C_s$, respectively) will involve a perpendicular transition. In agreement with a perpendicular transition, calculations by Schinke and Grebenshchikov[97] indicate that the small feature to the blue of the Hartley band is due to excitation to $5^1A'$ ($^1A_1$ in $C_{2v}$) and $4^1A''$ ($^1B_1$ in $C_{2v}$) states. Based on an imaging experiment of the O($^1$D) fragments resulting from ozone photodissociation at 193 nm it is possible that there is also some excitation to the B state ($3^1A'$ in $C_s$, $^1B_2$ in $C_{2v}$) at this wavelength.[101]

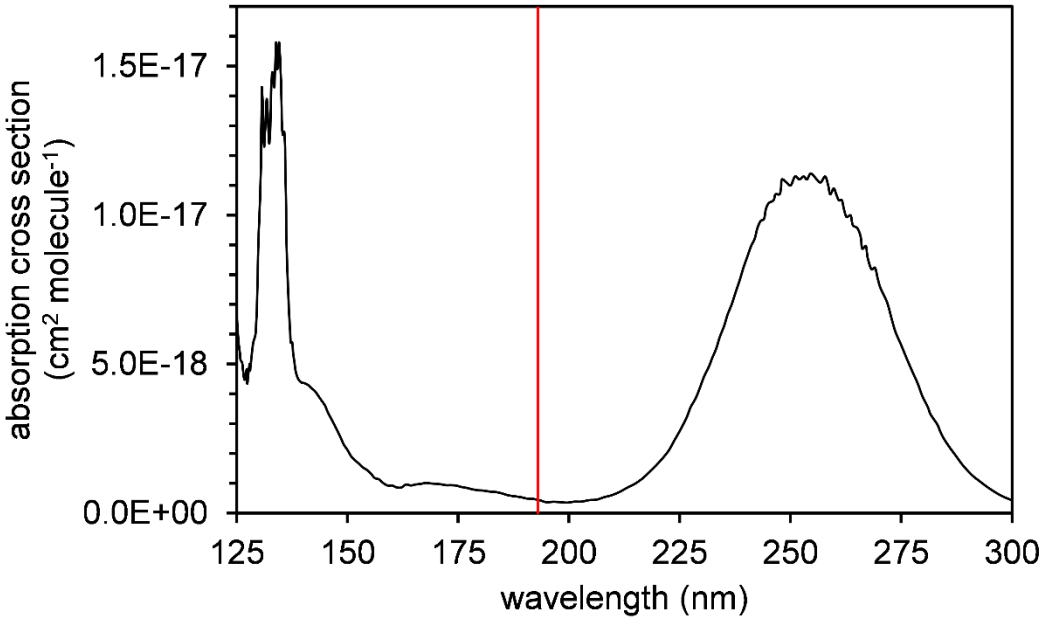


Figure 6.5. Absorption cross sections of ozone in the UV. Data from Mason *et al.*[102] The position of 193 nm is indicated by the red line.

As the B, $5^1A'$, and $4^1A''$ states all diabatically correlate to $O(^1D) + O_2(a^1\Delta_g)$ products, probing the $O_2(a^1\Delta_g)$ fragments resulting from the photodissociation of ozone at 193 nm can provide insight into which states are involved in the excitation. Excitation to an A′ or A″ state can be distinguished by measuring the $O_2(a^1\Delta_g)$ rotational distribution. Due to conservation of symmetry, photodissociation following excitation to a state with A′ symmetry will result in a preference for the formation of the A′ Λ-doublet, and thus even rotational states, while photodissociation following excitation to a state with A″ symmetry will result in a preference for the formation of the A″ Λ-doublet, and thus odd rotational states. Consequently, a rotational distribution with odd/even alternation favoring

the even rotational states would suggest excitation to the B state or the $5^1A'$ state, while a rotational distribution with odd/even alternation favoring the odd rotational states would suggest excitation to the $4^1A''$. The most likely case is that there are contributions from excitation to all three of these states, resulting in three different rotational distributions which may or may not overlap. Ion imaging of the $O_2(a^1\Delta_g)$ fragments can help distinguish between fragments resulting from transitions to the B state or the $5^1A'$ and $4^1A''$ states as **μ-v** will be positive for the B state and negative for the $5^1A'$ and $4^1A''$ states. Additionally, at 193 nm, a second singlet channel is energetically available, with ozone dissociating into $O(^1D)$ and $O_2(b\ ^1\Sigma_g^+)$. While multiple studies have found indirect evidence for this channel at 193 nm, to the best of our knowledge, no studies have directly probed the $O_2(b\ ^1\Sigma_g^+)$ photoproducts at this wavelength. There are multiple previously published REMPI schemes that can be used to detect $O_2(b\ ^1\Sigma_g^+)$[63, 103] and confirm the presence of this channel at 193 nm.

# REFERENCES


1. J. B. Burkholder, S. P. Sander, J. P. D. Abbat, J. R. Barker, R. E. Huie, C. E. Kolb, M. J. Kurylo, V. L. Orkin, D. M. Wilmouth and P. H. Wine, edited by NASA (2015), Vol. JPL Publication 15-10.

2. D. Picconi and S. Y. Grebenshchikov, J. Chem. Phys. **141**, 074311 (2014).

3. S. Y. Grebenshchikov, Z. W. Qu, H. Zhu and R. Schinke, Phys. Chem. Chem. Phys. **9**, 2044 (2007).

4. J. H. Seinfeld and S. N. Pandis, *Atmospheric Chemistry and Physics : From Air Pollution to Climate Change.* (Wiley, Somerset, United States, 2012).

5. W. B. Demore, S. P. Sander, D. M. Golden, R. F. Hampson, M. J. Kurylo, C. J. Howard, A. R. Ravishankara, C. E. Kolb and M. J. Molina, edited by NASA (1997), Vol. JPL Publication 97-4.

6. R. K. Talukdar, M. K. Gilles, F. Battin-Leclerc, A. R. Ravishankara, J.-M. Fracheboud, J. J. Orlando and G. S. Tyndall, Geophys. Res. Lett. **24**, 1091 (1997).

7. R. K. Sparks, L. R. Carlson, K. Shobatake, M. L. Kowalczyk and Y. T. Lee, J. Chem. Phys. **72**, 1401 (1980).

8. K. Takahashi, S. Hayashi, Y. Matsumi, N. Taniguchi and S. Hayashida, J. Geophys. Res. Atmos. **107**, ACH 11 (2002).

9. N. Taniguchi, K. Takahashi and Y. Matsumi, J. Phys. Chem. A **104**, 8936 (2000).

10. I. A. Cooper, P. J. Neill and J. R. Wiesenfeld, J. Geophys. Res. Atmos. **98**, 12795 (1993).

11. M. Trolier and J. R. Wiesenfeld, J. Geophys. Res. Atmos. **93**, 7119 (1988).

12. S. M. Ball, G. Hancock, S. E. Martin and J. C. Pinot de Moira, Chem. Phys. Lett. **264**, 531 (1997).

13. R. Schinke and G. C. McBane, J. Chem. Phys. **132**, 044305 (2010).

14. P. L. Houston, *Modern Trends in Chemical Reaction Dynamics : Experiment and Theory (Part 2).* (World Scientific Publishing Co Pte Ltd, Singapore, 2004).

15. S. M. Dylewski, J. D. Geiser and P. L. Houston, J. Chem. Phys. **115**, 7460 (2001).

16. J. J. Valentini, Chem. Phys. Lett. **96**, 395 (1983).

17. J. J. Valentini, D. P. Gerrity, D. L. Phillips, J. C. Nieh and K. D. Tabor, J. Chem. Phys. **86**, 6745 (1987).

18. M. A. Thelen, T. Gejo, J. A. Harrison and J. R. Huber, J. Chem. Phys. **103**, 7946 (1995).

19. R. K. Talukdar, C. A. Longfellow, M. K. Gilles and A. R. Ravishankara, Geophys. Res. Lett. **25**, 143 (1998).

20. G. Herzberg, *Spectra of Diatomic Molecules.* Second ed(D. Van Nostrand Company, Inc., New York, 1939).

21. E. Baloïtcha and G. G. Balint-Kurti, J. Chem. Phys. **123**, 014306 (2005).

22. R. Schinke, S. Y. Grebenshchikov, M. V. Ivanov and P. Fleurat-Lessard, Annu. Rev. Phys. Chem. **57**, 625 (2006).

23. S. A. Ndengué, R. Schinke, F. Gatti, H.-D. Meyer and R. Jost, J. Phys. Chem. A **116**, 12271 (2012).

24. P. R. Bunker, P. Jensen and C. National Research Council, *Molecular Symmetry and Spectroscopy.* (NRC Research Press, Ottawa, 1998).

25. If Pcross is calculated using a velocity of 1236 m/s and the VBR and |ΔF| values calculated by Schinke and McBane for a bond angle of 120° and a conserved bond length of 2.70 a0 a crossing probability of 0.6 percent is predicted. This value should be viewed as a lower bound, because most of the molecules that cross from the B to the R state are not in the equilibrium geometry of the ground state and have elongated conserved bonds.

26. M. L. Warter, C. E. Gunthardt, W. Wei, G. C. McBane and S. W. North, J. Chem. Phys. **149**, 134309 (2018).

27. G. Hancock, P. J. Pearson, G. A. D. Ritchie and D. F. Tibbetts, Chem. Phys. Lett. **393**, 425 (2004).

28. G. Hancock, S. J. Horrocks, P. J. Pearson, G. A. Ritchie and D. F. Tibbetts, J. Chem. Phys. **122**, 244321 (2005).

29. S. J. Horrocks, G. A. Ritchie and T. R. Sharples, J. Chem. Phys. **127**, 114308 (2007).

30. G. Hancock, G. A. D. Ritchie and T. R. Sharples, Mol. Phys. **111**, 2012 (2013).

31. K. Mauersberger, Geophys. Res. Lett. **8**, 935 (1981).

32. K. Mauersberger, Geophys. Res. Lett. **14**, 80 (1987).

33. A. M. Fernando, P. F. Bernath and C. D. Boone, J. Quant. Spectrosc. Radiat. Transfer **238**, 106547 (2019).

34. R. N. Clayton, L. Grossman and T. K. Mayeda, Science **182**, 485 (1973).

35. J. A. Kaye and D. F. Strobel, J. Geophys. Res. Oceans **88**, 8447 (1983).

36. M. H. Thiemens and J. E. Heidenreich, Science **219**, 1073 (1983).

37. J. Morton, J. Barnes, B. Schueler and K. Mauersberger, J. Geophys. Res. Atmos. **95**, 901 (1990).

38. J. J. Valentini, J. Chem. Phys. **86**, 6757 (1987).

39. P. L. Houston, A. G. Suits and R. Toumi, J. Geophys. Res. Atmos. **101**, 18829 (1996).

40. J. Eluszkiewicz and M. Allen, J. Geophys. Res. Atmos. **98**, 1069 (1993).

41. C. E. Fairchild, E. J. Stone and G. M. Lawrence, J. Chem. Phys. **69**, 3632 (1978).

42. T. G. Slanger, L. E. Jusinski, G. Black and G. E. Gadd, Science **241**, 945 (1988).

43. R. Toumi, B. J. Kerridge and J. A. Pyle, Nature **351**, 217 (1991).

44. C. A. Rogaski, J. M. Price, J. A. Mack and A. M. Wodtke, Geophys. Res. Lett. **20**, 2885 (1993).

45. J. M. Price, J. A. Mack, C. A. Rogaski and A. M. Wodtke, Chem. Phys. **175**, 83 (1993).

46. C. A. Rogaski, J. A. Mack and A. M. Wodtke, Faraday Discuss. **100**, 229 (1995).

47. R. L. Miller, A. G. Suits, P. L. Houston, R. Toumi, J. A. Mack and A. M. Wodtke, Science **265**, 1831 (1994).

48. R. T. Jongma and A. M. Wodtke, J. Chem. Phys. **111**, 10957 (1999).

49. P. J. Crutzen, J.-U. Grooß, C. Brühl, R. Müller and J. M. Russell, Science **268**, 705 (1995).

50. D. W. Chandler and P. L. Houston, J. Chem. Phys. **87**, 1445 (1987).

51. A. T. J. B. Eppink and D. H. Parker, Rev. Sci. Instrum. **68**, 3477 (1997).

52. J. Luque and D. R. Crosley, SRI International Report **99** (1999).

53. C. Leforestier, F. LeQuéré, K. Yamashita and K. Morokuma, J. Chem. Phys. **101**, 3806 (1994).

54. B. R. Johnson and J. L. Kinsey, Phys. Rev. Lett. **62**, 1607 (1989).

55. B. R. Johnson and J. L. Kinsey, J. Chem. Phys. **91**, 7638 (1989).

56. B.-Y. Chang, R. C. Hoetzlein, J. A. Mueller, J. D. Geiser and P. L. Houston, Rev. Sci. Instrum. **69**, 1665 (1998).

57. G. M. Roberts, J. L. Nixon, J. Lecointre, E. Wrede and J. R. R. Verlet, Rev. Sci. Instrum. **80**, 053104 (2009).

58. M. P. Grubb, M. L. Warter, C. D. Freeman, N. A. West, K. M. Usakoski, K. M. Johnson, J. A. Bartz and S. W. North, J. Chem. Phys. **135**, 094201 (2011).

59. A. G. Suits, R. L. Miller, L. S. Bontuyan and P. L. Houston, J. Chem. Soc., Faraday Trans. **89**, 1443 (1993).

60. G. Hancock, P. J. Pearson, G. A. D. Ritchie and D. F. Tibbetts, Phys. Chem. Chem. Phys. **5**, 5386 (2003).

61. S. J. Horrocks, G. A. D. Ritchie and T. R. Sharples, J. Chem. Phys. **126**, 044308 (2007).

62. B. R. Lewis, S. T. Gibson, J. S. Morrill and M. L. Ginter, J. Chem. Phys. **111**, 186 (1999).

63. J. S. Morrill, M. L. Ginter, E. S. Hwang, T. G. Slanger, R. A. Copeland, B. R. Lewis and S. T. Gibson, J. Mol. Spectrosc. **219**, 200 (2003).

64. H. B. Levene and J. J. Valentini, J. Chem. Phys. **87**, 2594 (1987).

65. M. L. Warter, Ph.D. thesis, Texas A&M University, 2016.

66. W. J. van der Zande, W. Koot, J. Los and J. R. Peterson, J. Chem. Phys. **89**, 6758 (1988).

67. K. Takahashi, N. Taniguchi, Y. Matsumi and M. Kawasaki, Chem. Phys. **231**, 171 (1998).

68. S. J. Horrocks, P. J. Pearson and G. A. D. Ritchie, J. Chem. Phys. **125**, 133313 (2006).

69. W. Denzer, S. J. Horrocks, P. J. Pearson and G. A. D. Ritchie, Phys. Chem. Chem. Phys. **8**, 1954 (2006).

70. W. Wei, C. J. Wallace, M. P. Grubb and S. W. North, J. Chem. Phys. **147**, 013947 (2017).

71. R. N. Dixon, J. Chem. Phys. **85**, 1866 (1986).

72. C. E. Gunthardt, M. N. Aardema, G. E. Hall and S. W. North, J. Chem. Phys. **151**, 224302 (2019).

73. M. P. Docker, Chem. Phys. **135**, 405 (1989).

74. G. E. Busch and K. R. Wilson, J. Chem. Phys. **56**, 3638 (1972).

75. W. Wei, C. J. Wallace, G. C. McBane and S. W. North, J. Chem. Phys. **145**, 024310 (2016).

76. C. J. Wallace, C. E. Gunthardt, G. C. McBane and S. W. North, Chem. Phys. **520**, 1 (2019).

77. G. C. McBane, J. A. Schmidt, M. S. Johnson and R. Schinke, J. Chem. Phys. **138**, 094314 (2013).

78. G. E. Busch and K. R. Wilson, J. Chem. Phys. **56**, 3626 (1972).

79. G. Erlandsson, Arkiv for Fysik **10**, 65 (1955).

80. H. B. Levene, J. C. Nieh and J. J. Valentini, J. Chem. Phys. **87**, 2583 (1987).

81. G. C. McBane, L. T. Nguyen and R. Schinke, J. Chem. Phys. **133**, 144312 (2010).

82. M. J. Bronikowski and R. N. Zare, Chem. Phys. Lett. **166**, 5 (1990).

83. S. W. North and G. E. Hall, J. Chem. Phys. **106**, 60 (1997).

84. F. J. Aoiz, M. Brouard, P. A. Enriquez and R. Sayos, J. Chem. Soc., Faraday Trans. **89**, 1427 (1993).

85. S. W. North and G. E. Hall, J. Chem. Phys. **104**, 1864 (1996).

86. W. S. McGivern and S. W. North, J. Chem. Phys. **116**, 7027 (2002).

87. C. A. Taatjes, J. I. Cline and S. R. Leone, J. Chem. Phys. **93**, 6554 (1990).

88. S. Han, C. E. Gunthardt, R. Dawes, D. Xie, S. W. North and H. Guo, The Proceedings of the National Acadamey of Sciences **Accepted** (2020).

89. P. O'Keeffe, T. Ridley, K. P. Lawley, R. R. J. Maier and R. J. Donovan, J. Chem. Phys. **110**, 10803 (1999).

90. C. K. Ulrich, J. Chen, O. Tokel, P. L. Houston and S. Y. Grebenshchikov, J. Phys. Chem. A **117**, 12011 (2013).

91. S. Y. Grebenshchikov and S. Rosenwaks, J. Phys. Chem. A **114**, 9809 (2010).

92. C. Kelleher, Ph.D. thesis, Cornell University, 2013.

93. A. Schmaunz, U. Kensy, A. Slenczka and B. Dick, Phys. Chem. Chem. Phys. **11**, 7115 (2009).

94. K. L. K. Lee, M. S. Quinn, A. T. Maccarone, K. Nauta, P. L. Houston, S. A. Reid, M. J. T. Jordan and S. H. Kable, Chem. Sci. **5**, 4633 (2014).

95. G. C. McBane, (Private Communication, 2020).

96. Y. Li, I. D. Petsalakis, H.-P. Liebermann, G. Hirsch and R. J. Buenker, J. Chem. Phys. **106**, 1123 (1997).

97. R. Schinke and S. Y. Grebenshchikov, Chem. Phys. **347**, 279 (2008).

98. M. R. Taherian and T. G. Slanger, J. Chem. Phys. **83**, 6246 (1985).

99. A. A. Turnipseed, G. L. Vaghjiani, T. Gierczak, J. E. Thompson and A. R. Ravishankara, J. Chem. Phys. **95**, 3244 (1991).

100. D. Stranges, X. Yang, J. D. Chesko and A. G. Suits, J. Chem. Phys. **102**, 6067 (1995).

101. M. Brouard, R. Cireasa, A. P. Clark, G. C. Groenenboom, G. Hancock, S. J. Horrocks, F. Quadrini, G. A. D. Ritchie and C. Vallance, J. Chem. Phys. **125**, 133308 (2006).

102. N. J. Mason, J. M. Gingell, J. A. Davies, H. Zhao, I. C. Walker and M. R. F. Siggel, J. Phys. B-At. Mol. Opt. **29**, 3075 (1996).

103. R. O. Loo, W. J. Marinelli, P. L. Houston, S. Arepalli, J. R. Wiesenfeld and R. W. Field, J. Chem. Phys. **91**, 5185 (1989).

104. R. G. Bray and R. M. Hochstrasser, Mol. Phys. **31**, 1199 (1976).

105. T. P. Rakitzis and A. J. Alexander, J. Chem. Phys. **132**, 224310 (2010).

# APPENDIX A

## 2 PHOTON LINESTRENGH EQUATIONS

Table A-1. 2-photon linestrength equations for a $|\Omega \pm 1\rangle \leftarrow |\Omega\rangle$ transition where $\Omega$ is the orbital angular momentum quantum number. Equations from Bray and Hochstrasser.[104]

| $\Delta j$ | $\lvert\Omega \pm 1\rangle \leftarrow \lvert\Omega\rangle$ |
|---|---|
| -2 | $\frac{(j \mp \Omega - 1)(j \mp \Omega)(j \mp \Omega - 2)(j \pm \Omega)}{15\, j(j-1)(2j-1)}$ |
| -1 | $\frac{(j \mp \Omega + 1)(j \mp \Omega)(j \mp \Omega - 2)(j \pm 2\Omega + 1)^2}{30\, j(j+1)(j-1)}$ |
| 0 | $\frac{(j \pm \Omega + 1)(2\Omega \pm 1)^2(2j+1)(j \mp \Omega)}{10\, j(j+1)(2j-1)(2j+3)}$ |
| 1 | $\frac{(j \pm \Omega + 1)(j \pm \Omega + 2)(j \mp 2)^2}{30\, j(j+1)(j+2)}$ |
| 2 | $\frac{(j \pm \Omega + 1)(j \pm \Omega + 2)(j \pm \Omega + 3)(j \mp \Omega + 1)}{15\,(j+1)(j+2)(2j+3)}$ |

APPENDIX B

2+1 REMPI EQUATIONS

$$\beta_2^{VV} = \frac{5\{[9800\beta_0^2(64)+2100\beta_0^2(44)-3080\beta_0^2(24)]s_4+[3168\beta_0^2(42)-7920\beta_0^2(22)-1848\beta_0^2(02)+16170\beta_0^0(22)]s_2+16170\beta_0^2(20)\}}{231\{[96\beta_0^2(42)+40\beta_0^2(22)+84\beta_0^2(02)]s_2+175\}}$$

$$\beta_4^{VV} = \frac{-[88200\beta_0^2(64)+95900\beta_0^2(44)-69300\beta_0^2(24)-148225\beta_0^0(44)]s_4-[-165528\beta_0^2(42)+58080\beta_0^2(22)-81312\beta_0^2(02)]s_2}{847\{[96\beta_0^2(42)+40\beta_0^2(22)+84\beta_0^2(02)]s_4+175\}}$$

$$\beta_6^{VV} = \frac{25[2590\beta_0^2(64)+60\beta_0^2(44)-220\beta_0^2(24)]s_4}{363\{[96\beta_0^2(42)+40\beta_0^2(22)+84\beta_0^2(02)]s_2+175\}}$$

$$\beta_2^{VH} = \frac{-10\{[455\beta_0^2(64)+510\beta_0^2(44)-638\beta_0^2(24)]s_4+[792\beta_0^2(42)-1056\beta_0^2(22)]s_2-1848\beta_0^2(20)\}}{[10220\beta_0^2(64)+3840\beta_0^2(44)-6380\beta_0^2(24)+3465\beta_0^0(44)]s_4+[-1584\beta_0^2(42)-5280\beta_0^2(22)-3696\beta_0^2(02)-9240\beta_0^0(22)]s_2+9240}$$

$$\beta_2^{HV} = \frac{5\{[35\beta_0^2(64)+15\beta_0^2(44)-20\beta_0^2(24)]s_4+[18\beta_0^2(42)-24\beta_0^2(22)-42\beta_0^0(22)]s_2\}}{[35\beta_0^2(64)+15\beta_0^2(44)-20\beta_0^2(24)]s_4+[18\beta_0^2(42)+60\beta_0^2(22)+42\beta_0^2(02)]s_2-105}$$

$$\beta_4^{HV} = \frac{-105[25\beta_0^2(64)+14\beta_0^2(44)-22\beta_0^2(24)+11\beta_0^0(44)]s_4}{11\{[35\beta_0^2(64)+15\beta_0^2(44)-20\beta_0^2(24)]s_4+[18\beta_0^2(42)+60\beta_0^2(22)+42\beta_0^2(02)]s_2+105\beta_0^2(20)-105\}}$$

*2+1 REMPI equations from Wei *et al.*[70]

Table B-1. Equations for $s_2$ and $s_4$ factors. $\lambda$ is 0 for linearly polarized light and ±1 for $\sigma_{\pm}1$ circularly polarized light. Equations from Rakitzis *et al.*[105]

| $\Delta j$ | $s_2$ | $s_4$ |
|---|---|---|
| -2 | $-\frac{10\,(j+1)}{7\,(2j-1)}(-1)^{\lambda}$ | $\frac{12\,j(j+1)^2(6)^{-\lvert\lambda\rvert}}{7\,(j-1)(2j-1)(2j-3)}$ |
| -1 | $\frac{5\,(j-5)}{7\,(2j-1)}(-1)^{\lambda}$ | $-\frac{24\,j(j+1)(6)^{-\lvert\lambda\rvert}}{7\,(j-1)(2j-1)}$ |
| 0 | $-\frac{5\,(2j-3)(2j+5)}{7\,(2j-1)(2j+3)}(-1)^{\lambda}$ | $\frac{72\,j(j+1)(6)^{-\lvert\lambda\rvert}}{7\,(2j-1)(2j+3)}$ |
| 1 | $\frac{5\,(j+6)}{7\,(2j+3)}(-1)^{\lambda}$ | $-\frac{24\,j(j+1)(6)^{-\lvert\lambda\rvert}}{7\,(j+2)(2j+3)}$ |
| 2 | $-\frac{10\,j}{7\,(2j+3)}(-1)^{\lambda}$ | $\frac{12\,j^2(j+1)(6)^{-\lvert\lambda\rvert}}{7\,(j+2)(2j+3)(2j+5)}$ |